3-14-2014

Design of a Programmable Star Tracker-Based Reference System For a Simulated Spacecraft

Warren C. Grunwald

DESIGN OF A PROGRAMMABLE STAR TRACKER-BASED REFERENCE SYSTEM FOR A SIMULATED SPACECRAFT

THESIS

Warren C. Grunwald, Second Lieutenant, USAF

AFIT-ENY-14-M-22

DEPARTMENT OF THE AIR FORCE
AIR UNIVERSITY

AIR FORCE INSTITUTE OF TECHNOLOGY

Wright-Patterson Air Force Base, Ohio

The views expressed in this thesis are those of the author and do not reflect the official policy or position of the United States Air Force, the Department of Defense, or the United States Government.

AFIT-ENY-14-M-22

DESIGN OF A PROGRAMMABLE STAR TRACKER-BASED REFERENCE SYSTEM FOR A SIMULATED SPACECRAFT

THESIS

Presented to the Faculty

Department of Aeronautics and Astronautics

Graduate School of Engineering and Management

Air Force Institute of Technology

Air University

Air Education and Training Command

in Partial Fulfillment of the Requirements for the

Degree of Master of Science in Astronautical Engineering

Warren C. Grunwald, B.S., Mechanical Engineering

Second Lieutenant, USAF

March 2014

AFIT-ENY-14-M-22

DESIGN OF A PROGRAMMABLE STAR TRACKER-BASED REFERENCE SYSTEM FOR A SIMULATED SPACECRAFT

Warren C. Grunwald, B.S., Mechanical Engineering
Second Lieutenant, USAF

Approved:

//signed//	06 March 2014
Eric D. Swenson, PhD (Chairman)	Date
//signed//	06 March 2014
Ronald J. Simmons, Lt Col, USAF (Member)	Date
//signed//	16 March 2014
James Newman, PhD (Member)	Date

AFIT-ENY-14-M-22

Abstract

The main objective of this research effort is to achieve an accuracy level for the SimSat star tracker system comparable to what is reported in current literature by various star tracker manufacturers and researchers. Previous work has provided a spherical star dome that needs to be fully populated with light sources. Programmable organic light emitting diode (OLED) panels were chosen to populate the dome to allow high contrast ratios without backlighting and increase the number of star combinations able to be represented. Noise equivalent angles less than five arcseconds (1σ) are achieved about the boresight axis and less than half an arcsecond around the other axes. Absolute accuracy near the center of the star dome is tested to be less than 0.04 degree about each axis. Two different approaches to inertially cataloging the starfield are also investigated, externally referencing each panels coordinates using a coordinate measurement arm and utilizing the camera's known position to catalog the panel's location. The full population of the SimSat star dome and reprogrammable capability of the panels allows many future research endeavors related to star pattern recognition and attitude determination to be undertaken.

Acknowledgements

I would first like to express my gratitude towards Dr. Eric Swenson for guiding me through this process as my faculty advisor. He was always very eager to hear updates, give construtive feedback, and offer potential solutions. Lt Col Ron Simmons also was also a great help during the course of my research, whether it was giving me feedback on my writing style or brainstorming what could be causing certain errors, he was another reason I was able to stay focused on this project.

I would also like to say a big thank you to the ENY laboratory technicians, specifically Chris Zickefoose, Jorge Urena, and Jay Anderson. They all helped get me the equipment I needed to move the project forward and took the time to teach me new skills which helped tremendously when constructing various hardware pieces used in this research. Chris Zickefoose was there to help me all along the way from the first order I placed until the very end of my time at AFIT. Jorge Urena assisted me in the beginning with the electronic components specifications and showed me useful resources and techniques related to all the electronics used in this project. His help allowed me to get a running start on this project and jump into the research faster. Jay Anderson was there when things needed to get done quickly and his assistance prevented certain crucial components from being further delayed.

Finally, I would like to thanks my friends and family for all of their support throughout this project. All of the other AFIT students I have had the pleasure of meeting, especially the ENY Astronautical Engineering students, have been a great boon to this project, either by bouncing ideas off each other or just being there as friends. My family has also been very supportive during my time at AFIT, thank you so much for believing in me.

Warren C. Grunwald

Table of Contents

Page

Page

List of Figures

List of Tables

List of Acronyms

Acronym	Definition
APS	Active Pixel Sensor
CCD	Charge-Coupled Device
CMM	coordinate measuring machine
ECI	Earth-Centered Inertial
FOV	field of view
LEDs	light emitting diodes
NEA	noise equivalent angle
NPS	Naval Postgraduate School
OLED	organic light emitting diode
PWM	pulse-width modulation
QUEST	Quaternion Estimation
TAS-2	Three-Axis Simulator-2

DESIGN OF A PROGRAMMABLE STAR TRACKER-BASED REFERENCE SYSTEM FOR A SIMULATED SPACECRAFT

I. Introduction

1.1 Motivation

Satellite simulators have been used to test different aspects of spacecraft dynamics since the dawn of the space age. By simulating dynamics on the ground, new algorithms can be tested and analyzed with instant feedback to the experimenter. Adding more capability to these simulators allows more advanced algorithms that incorporate different aspects of true spaceflight into the simulators. Also, these satellite simulators provide a valuable learning experience for those designing and building them, which is why they are popular in academia. The Air Force Institute of Technology's (AFIT) latest satellite simulator (SimSat, a.k.a. SIMSAT II) is the second generation that has been designed and built by students.

SimSat is a tabletop style satellite simulator that sits on a spherical air bearing which simulates a very low friction environment for rotational dynamics testing. SimSat has been invaluable to students at AFIT over the years, with the second generation unit's initial design being the focus of a three person thesis in 2008 [22]. These three students took a systems engineering approach to redesigning SIMSAT I from its dumbbell configuration to the more versatile tabletop configuration of SIMSAT II and also added fans to simulate spacecraft thrusters. The following year, SimSat proved to be an effective testbed for an optimal control thesis involving these thrusters. This thesis effort required accurately characterizing SimSat's mass and moments of inertia along with integrating a laser gyroscope into the control logic to run the control algorithms [17]. SimSat's capabilities

were further improved in 2010 when reaction wheels and SIMULINK control logic were added to the system [25]. In 2011, a control moment gyroscope (CMG) was designed at AFIT and added to SimSat [16]. At that point SimSat had three separate actuator systems but only one attitude determination method in the laser gyroscope. The laser gyroscope was prone to drift errors after running for extended periods of time so an external reference system was desired.

Star trackers are the most accurate method for determining spacecraft attitude used on real satellites, so an effort to develop a star tracker based reference system for SimSat was undertaken. Star trackers operate by taking pictures of the stars, analyzing the patterns in the picture to determine which stars are in the field of view (FOV), and then determining the rotation by comparing the body vectors obtained from stars in the FOV to an inertially known vector in the star catalog. In order to simulate this effect, Jorge Padro added a black star dome above SimSat, experimented with using light emitting diodes (LEDs) to represent stars, and developed image processing and cataloging code using MATLAB [20]. Padro's work showed the idea could work, but only three small LED panels were placed upon the dome and the system accuracy was near one degree (1σ). The groundwork dome by Padro showed some promise; however, additional work was needed to ensure the dome could be fully populated with stars and to increase the accuracy of the system.

This thesis effort focuses on completing the SimSat star tracker system (current configuration shown in Figure 1.1). The additional source of attitude knowledge allows filtering algorithms to be utilized that take information both from the gyroscopes and the star tracker. The increased attitude knowledge will allow more complex control algorithms to be run, which will further SimSat's original purpose as a diverse satellite dynamics testbed.

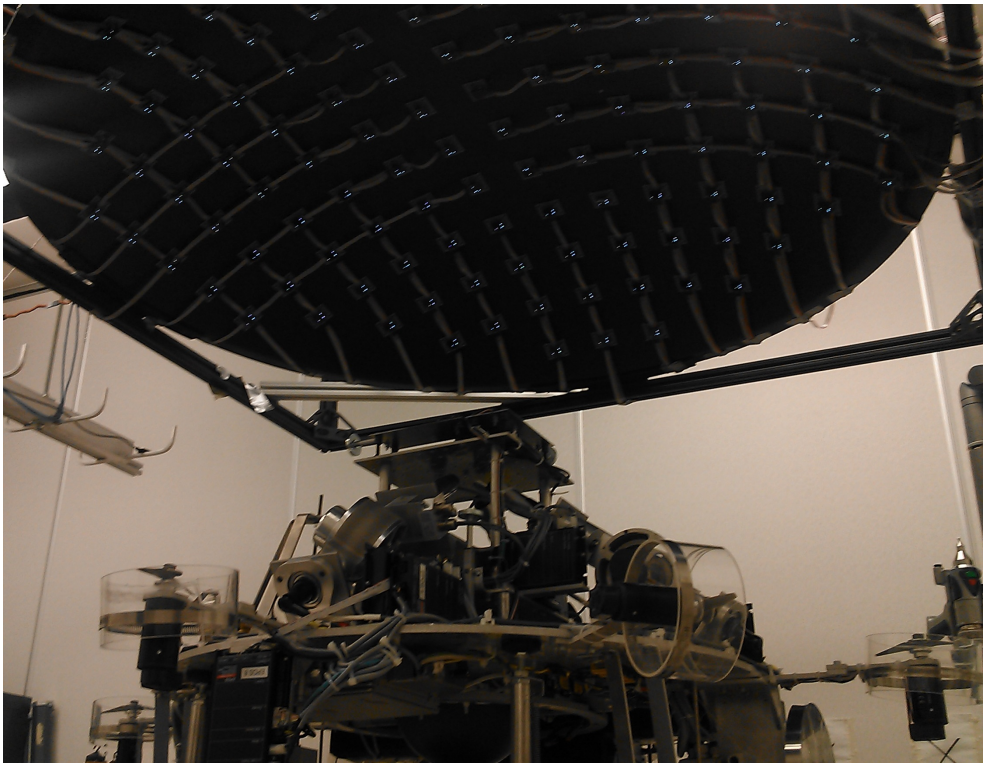

Figure 1.1: SimSat and Star Dome Configuration

1.2 Problem Statement

SimSat is utilized for hardware-in-the-loop validation of various satellite control algorithms. SimSat previously relied on only gyroscope information, which is prone to noise and random drift over time. In order to provide an external reference over the full range of motion possible by SimSat, the star dome above SimSat needs to be completely populated and have a star tracker system capable of accurately determining attitude within at least a tenth of a degree about each axis. Several options for fully populating the dome were considered and several different star tracker configurations were tested in order to have the highest accuracy possible.

1.3 Research Objectives

The main objective of this research is to achieve an accuracy level for the SimSat system comparable to what is reported in current literature by various star tracker manufacturers and researchers. This level is usually less than one arcsecond for the relative accuracy. In order to achieve that level of accuracy, the system needs to be broken down and characterized to determine what are the most important effects on the accuracy. Some aspects of the system that are focused on in this research are the type of camera, the optics, and the characteristics of the light source. Once this characterization is complete, improving integration with SimSat is another key objective. This entails ensuring an accurate solution over the full range of motion of SimSat and cataloging every star in a set inertial frame. This research effort will serve as a stepping stone towards a more robust and efficient integration with SimSat.

1.4 Thesis Overview

Chapter II provides a literature review of relevant topics that are utilized in this research, such as attitude dynamics, different approaches to representing starfields, star tracker accuracy components, star image processing, and attitude determination algorithms. Chapter III delves into the process of the accuracy improvements and characterization, the design for fully populating the star dome, the star cataloging approach, the system software algorithms, and accuracy validation methods. Chapter IV presents the results of the accuracy tests performed both on the optics bench and after the system has been moved back to above SimSat. Finally, Chapter V will present the conclusions to be gained from this research and include recommendations for future work.

II. Background

This chapter will cover the relevant information that was reviewed before this thesis effort was undertaken. First, spacecraft attitude dynamics were studied to both motivate the problem and better understand how attitude knowledge can be applied and transformed. Then, different ways of representing star fields were examined to see what already exists and how successful different implementations of indoor starfields have been. Next, star tracker development and technical characteristics are discussed to understand how a star tracker operates and what aspects are important for accuracy. Coupled with star tracker operation is star image processing which covers how the star location is extracted from the data in the star image. Last, a summary of different attitude determination algorithms typically used is presented.

2.1 Spacecraft Attitude Dynamics

In this section, attitude dynamics are discussed to explain the problem that star trackers solve. This section also shows the different ways that rotations can be represented in order to clarify the terminology used throughout this thesis. An object's orientation with respect to a fixed frame is its attitude. The calculations required to determine the torques acting on the spacecraft must be performed in an inertial (non-accelerating) frame since the equations governing spacecraft attitude dynamics are derived from Euler's equation [32]. Euler's equations states that the time rate of change of angular momentum $\vec{H}$ is equal to the torque $\vec{M}$ on the object

$$\vec{M} = \frac{^{i}d}{dt}(\vec{H}). \tag{2.1}$$

Thus, the fixed frame used as a reference for the spacecraft needs to be inertial in order to use equations deriving from Equation (2.1). Once a suitably inertial frame is chosen, the

coordinate frame derivative transport theorem can be used to generate and expression in terms of the spacecraft's body frame, as shown in

$$\vec{M}_b = \frac{^b d}{dt}(\vec{H}_b) + \vec{\omega}^{bi} \times \vec{H}_b \tag{2.2}$$

where $\vec{M}_b$ is the torque vector in the body frame of the spacecraft, $\vec{H}_b$ is the angular momentum vector in the body frame, and $\vec{\omega}^{bi}$ is the angular velocity vector in the body frame. Equation (2.2) specifies the relationship between torques in the spacecraft body frame and angular velocity in the body frame with respect to inertial frame. However, for these equations to be useful for attitude control, a mathematical representation of the spacecraft's current attitude needs to be chosen, which is discussed in Section 2.1.2. Once a proper representation is chosen, a controller can be implemented to control the spacecraft as long as angular velocity and attitude can be determined. Determining attitude, to be discussed in detail in Section 2.1.3, is usually done utilizing gyroscopes for frequent measurements, while utilizing inertial references update gyroscope reference points and determine absolute attitude with no prior information. Before being able to determine a spacecraft's attitude, a proper inertial reference frame must be defined, which is discussed next.

2.1.1 Reference Frames.

In this section we will discuss different reference frames commonly used in spacecraft attitude determination because properly defining reference frames is essential to the attitude determination problem. For a coordinate frame to be truly inertial, the frame must not be rotating or otherwise accelerating. For this reason, the astronautical community commonly uses an Earth-Centered Inertial (ECI) frame based on the direction to the Vernal Equinox, which is fixed with respect to the stars [26]. The current standard is known as J2000, which fixes the intersection of the celestial equator and the orbital plane as of noon 1 January 2000 Terrestrial Time as the X-axis of the ECI frame. The Z-axis of the ECI frame is towards the

celestial north pole (Earth's rotation axis) and the Y-axis completes the right handed set, shown in Figure 2.1.

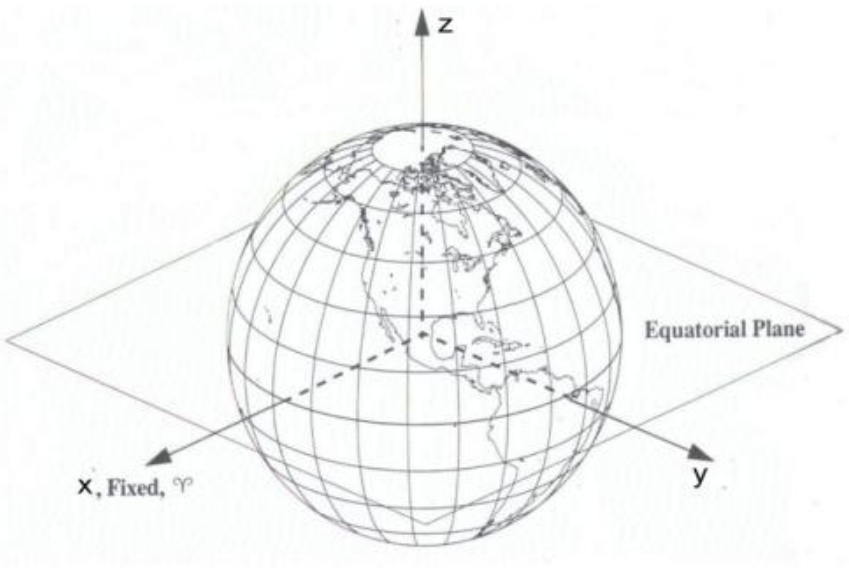

Figure 2.1: Earth Centered Inertial Frame Coordinates

Using a consistent reference frame is essential for attitude determination. For example, the *Hipparcos* catalog contains over a hundred thousand star locations listed in the J2000 ECI frame. However, the *epoch* for the stars' locations is J1991.25 [1]. The epoch of the stars must be defined because their location in space will change; their current location must be updated based on their proper motion and the current date. Although the J2000 ECI frame is fixed, the stars coordinates in that frame must be updated at the time that a measurement is taken.

Now that a suitably inertial reference frame has been defined for spacecraft applications, the other commonly used frames must be defined. For star tracker applications, the stars will first be recorded in the star tracker camera frame. The camera frame refers to an XYZ-axis set fixed to the head of the camera. The frame is centered on the boresight of the camera with the X-axis pointing parallel to the boresight. In the

image formed by the camera, everything is assumed to be a unit distance away [4]. This allows points in the image to be expressed as unit vector in the camera frame, as shown in Figure 2.2 . Since the camera is fixed to the body of the spacecraft, a set rotation from the camera frame to the body frame will allow the star tracker to calculate the body frame's orientation.

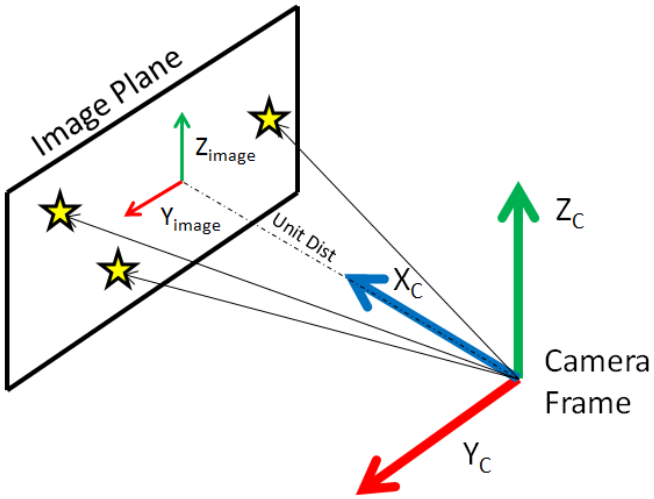

Figure 2.2: Image Coordinates in the Camera Frame

The body frame of the spacecraft is the set of local axes that are non-inertial and are fixed to the spacecraft, as shown in Figure 2.3. Having axes fixed to the body of the spacecraft ensures that the moment of inertia expressed in these coordinates will not change from the spacecraft's rotational motion. Usually these axes are chosen to be at the center of mass and align with the principal axes of the spacecraft to make the math for attitude dynamics calculations simpler. Now that all of the axes have been chosen for a spacecraft (inertial set, camera frame, and body frame), we will discuss the methods for representing the rotation of one frame to another.

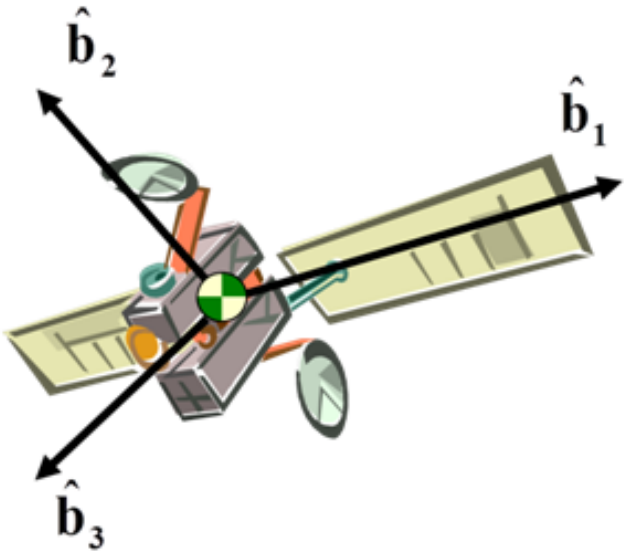

Figure 2.3: Body Frame Fixed to the Spacecraft

2.1.2 Rotation Representations.

Rotations can be represented in a variety a ways, of which the most common is the rotation matrix $\boldsymbol{R}^{bi}$. Utilizing a rotation matrix allows vectors in one frame to be represented in another frame, such as a vector in the inertial frame $\vec{v}_i$ to be represented in the body frame $\vec{v}_b$ by

$$\vec{v}_b = \boldsymbol{R}^{bi}\vec{v}_i \tag{2.3}$$

The requisite property for a matrix to represent a rotation is that the matrix's columns must be *orthonormal*, meaning each column is unit magnitude and is orthogonal to both other columns. The matrix $\boldsymbol{R}^{bi}$ is composed of columns of an orthonormal basis for the inertial frame, where each basis component is expressed in the body frame [26]. Because of this basis expression property, rotation matrices are also referred to as *direction cosine matrices* since each element is a dot product between two different unit vectors, essentially leaving the cosine of the angle between each vector as values in the matrix. Because of

orthonormality, the nine elements of the matrix have six constraints applied so there are only three free degrees of freedom in the rotation matrix.

One of the simplest ways to think about a rotation from one frame to another is to break it into three simpler rotations. Leonhard Euler was the first to suggest that these three parameters be used to break up a rotation matrix into three simple rotations [26]. These three rotation angles are now commonly referred to as Euler Angles, which are expressed in shorthand by the sequence about which axis is the rotation axis. For example, a "3-2-1" Euler Angle set would first involve $\boldsymbol{R_3(\theta_1)}$, which is read as "rotation about the 3-axis by θ_1", then $\boldsymbol{R_2(\theta_2)}$, and finally $\boldsymbol{R_1(\theta_3)}$. These rotation matrices are shown in the equations below

$$\boldsymbol{R_3(\theta_1)} = \begin{bmatrix} \cos(\theta_1) & \sin(\theta_1) & 0 \\ -\sin(\theta_1) & \cos(\theta_1) & 0 \\ 0 & 0 & 1 \end{bmatrix} \tag{2.4}$$

$$\boldsymbol{R_2(\theta_2)} = \begin{bmatrix} \cos(\theta_2) & 0 & -\sin(\theta_2) \\ 0 & 1 & 0 \\ \sin(\theta_2) & 0 & \cos(\theta_2) \end{bmatrix} \tag{2.5}$$

$$\boldsymbol{R_1(\theta_3)} = \begin{bmatrix} 1 & 0 & 0 \\ 0 & \cos(\theta_3) & \sin(\theta_3) \\ 0 & -\sin(\theta_3) & \cos(\theta_3) \end{bmatrix}. \tag{2.6}$$

The final rotation matrix can be expressed by multiplying each of the Euler Angle rotation matrices

$$\boldsymbol{R^{bi}} = \boldsymbol{R_1(\theta_3)R_2(\theta_2)R_3(\theta_1)}. \tag{2.7}$$

While Euler Angles may be useful for breaking a rotation into easy to visualize components, there are two issues when it comes to using them for attitude determination

and control calculations. First, every Euler Angle set has a singularity that causes the first and third rotations to become indistinguishable. For symmetric sets such as 3-1-3 or 1-2-1, the singularity occurs when $\theta_2 = 0$ or π and with asymmetric sets such as the previous example or 2-3-1, the singularity occurs when $\theta_2 = \frac{\pi}{2}$ or $\frac{3\pi}{2}$ [26]. Secondly, trigonometric functions must be called several times for every given Euler Angle set, which can be costly and time consuming. For these reasons, Euler Parameters or *quaternions* are commonly used for attitude calculations.

Quaternions are based upon the fact that any rotation can be represented by a single axis rotation about some axis. This idea was formed by Euler, so the axis of rotation is referred to as an Euler Axis $\hat{e}$ with the angle of rotation θ referred to as the *principle* Euler Angle [26]. An example of this rotation is shown in Figure 2.4. There are now four parameters describing the rotation instead of the minimum of three. There is an extra constraint in this representation in the form that $\hat{e}$ must be a unit vector, which is enforced through $\hat{e}^T\hat{e} = 1$. However, if the rotation angle is zero, then the rotation axis cannot be determined from the rotation matrix and there is a singularity. Quaternions overcome this by re-parameterizing the Euler Axis/Angle set as

$$\tilde{q} = \begin{bmatrix} \vec{q} \\ q_4 \end{bmatrix} = \begin{bmatrix} e_1 \sin\frac{\theta}{2} \\ e_2 \sin\frac{\theta}{2} \\ e_3 \sin\frac{\theta}{2} \\ \cos\frac{\theta}{2} \end{bmatrix}. \tag{2.8}$$

Through this method, the quaternion can always be related to a rotation without any singularity or ambiguity. Quaternions also eliminate the need for utilizing trigonometric functions when performing attitude dynamics calculations. For example, the spacecraft control algorithm needs to find the difference between the current quaternion, $\tilde{q}_c$, and the desired quaternion, $\tilde{q}_d$, which are both assumed to be defined in the same frame (expressing

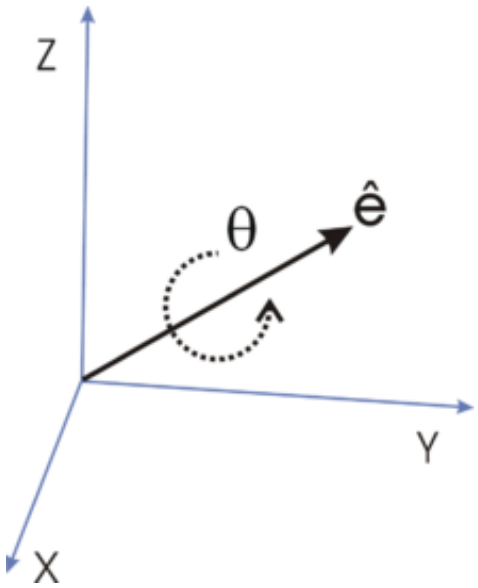

Figure 2.4: Euler Axis and principle Euler Angle Representation

a rotation from the inertial frame) [16]. The difference between $\tilde{q}_c$ and $\tilde{q}_d$ relative to $\tilde{q}_c$ can be defined as

$$\tilde{q}_d^{\{\tilde{q}_c\}} = \begin{bmatrix} q_{c4} & q_{c3} & -q_{c2} & -q_{c1} \\ -q_{c3} & q_{c4} & q_{c1} & -q_{c2} \\ q_{c2} & -q_{c1} & q_{c4} & -q_{c3} \\ q_{c1} & q_{c2} & q_{c3} & q_{c4} \end{bmatrix}^T \begin{bmatrix} q_{d1} \\ q_{d2} \\ q_{d3} \\ q_{d4} \end{bmatrix}. \tag{2.9}$$

When the difference between the desired and controlled states is zero, $\tilde{q}_d^{\{\tilde{q}_c\}}$ (read as desired quaternion relative to current quaternion) is $[0\ \ 0\ \ 0\ \ 1]^T$. This approach can also be used to compare solutions calculated mathematically to solutions from external measurements such as a star tracker. Comparing external measurements to internally propagated methods, such math models and gyroscope measurements, is an essential portion of spacecraft attitude determination. Now that we have discussed different frames and their representation, we will cover the process of determining the spacecraft's attitude.

2.1.3 Attitude Determination.

This section overviews spacecraft attitude determination because it is an essential part of satellite operations and the main mission of star trackers. Spacecraft often operate in two modes when determining their attitude: Normal and Lost in Space. Normal mode occurs when prior attitude information is available, then that information can be used to update the current attitude. Rate gyroscopes can use prior attitude information in this way since they measure angular velocities and can be integrated to give current attitude [32]. However, star trackers and other inertial sensors that use external information to form vector-based observations (such as magnetometers and sun sensors) can use this information as well to limit searching time or to reject erroneous measurements. In regards to this thesis effort, the most important consideration for normal attitude operations occurs in how the star tracker catalog architecture and star pattern recognition algorithm are built, which will be detailed in Section 2.4.3. These aspects are important to normal mode because they are historically the limiting factors in terms of time for the star tracker to generate a solution and how they incorporate current attitude information can greatly speed up their solution time. Recognizing a portion of the night sky is not a trivial matter, see Figure 2.5, especially when false objects such as planets, other satellites, and radiation incidents may be present [5]. Since prior attitude knowledge is available during normal mode, the possible section of night sky that the camera is looking at can be narrowed, which could save several seconds of processing time, depending on the number of stars in the catalog.

However, if no prior attitude knowledge is available then the spacecraft goes into Lost in Space attitude determination. With no *a priori* knowledge, the system is totally reliant on inertial references in the form of vector- based observations. This process can be described simply as follows: first the sensor will make measures in the sensor frame to come up with a vector (such as one pointing at a certain star), then this sensor frame vector can be rotated to the spacecraft's body frame based on the known position and orientation of the

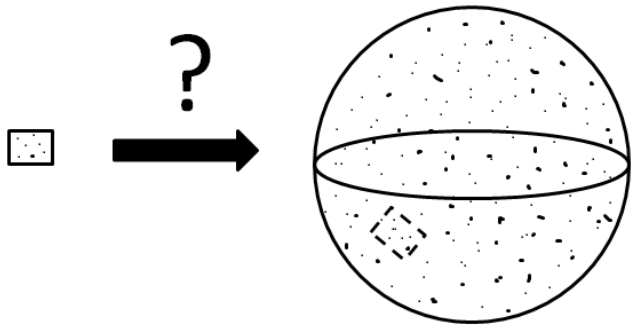

Figure 2.5: Determining Attitude from a Small Sky Sample [5]

sensor, then information about that observation is used to come up with a matching inertial vector (such as the stars magnitude and properties about its relation to nearby stars), finally this matching inertial-sensor vector set can be used in the attitude determination algorithms described in Section 2.5. Other sensors, such as sun sensors or magnetometers, work the same way, but instead of a star catalog these sensors require cataloged information about the sun's relative position or the Earth's magnetic field vector, respectively. The spacecraft's body frame orientation can be described with exactly three parameters of information; however, each vector measurements produces only two unique pieces of information since each measurement is a unit vector (three scalars with one constraint). Thus, the attitude determination problem is undetermined with one measurement and overdetermined with more than one measurement [8]. How this problem is resolved depends on if the solution should be deterministic or optimal and is covered in detail in Section 2.5. For this thesis, the focus will be on the Lost in Space case; however, before delving further into how to solve that problem, first the problem of how to best represent stars in a laboratory must be investigated.

2.2 Starfield Representation

This section will cover some basic characteristics about starlight and other research efforts that involve creating simulated starfields to compare and contrast different approaches to this problem. To simulate a star field, the stars have to be suitably represented in a way that allows repeatable and accurate measurements. Real stars' characteristics must first be examined to understand what can and cannot be easily mimicked in a laboratory setting. Then, methods utilizing dome-like structures and LEDs to create star-like illumination are studied. Finally, star fields created using pixelated screens are examined.

2.2.1 Real Stars.

This segment covers basic aspects of real starlight, describing what true star trackers are looking for and guiding the choices for a good star field. The current method of characterizing a star's apparent magnitude dates back to the ancient Greeks when the astronomer Hipparchus cataloged about one thousand stars visible to the naked eye, listing the brightest stars as first magnitude stars and the faintest as sixth magnitude stars [2]. Once these magnitude levels were quantified nearly two thousand years later, it was discovered that the first magnitude stars were roughly one hundred times brighter than the sixth magnitude stars. From this, one step in magnitude was *defined* as a factor of $\sqrt[5]{100} = 2.512...$, which made five magnitudes difference equal to a flux difference of 100. Essentially the apparent magnitude scale is a comparison between flux levels, with the current apparent magnitude zero set by the star Vega [2]. Knowing the expected photon flux from a star allows magnitude comparisons with other stars that may be used on a star tracker testbed. We can calculate the apparent visual magnitude received by a sensor from

$$m_1 = -2.5 \log(C_1/C_2) + m_2 \tag{2.10}$$

where m_2 is a standard star's visual magnitude, C_2 is the photon flux from that star on earth, and C_1 is the photon flux from the source used for comparison. This method allows star trackers' visual magnitude thresholds to be compared in the laboratory using light from star-like sources, even if those sources may not exhibit all of the qualities of real starlight. Light from real stars is coming from infinity from the camera's perspective. This means that the light will be *collimated*, which means that the light rays will be parallel and focus to the same point in the focal place [9]. Stars will occupy very small regions of the camera's FOV and will appear as point sources when focused to infinity, as shown in Figure 2.6. This means that the camera will only be able to have the location of the star in the image frame accurate to a single pixel (which is not accurate enough for most missions). This can be remedied by defocussing the camera and spreading the light over more pixels to achieve subpixel precision. This will be covered in more detail in Section 2.4.2, but it means that having collimated light focused to a single point is not necessarily essential, or even desired, when trying to recreate star tracker methods and accuracy.

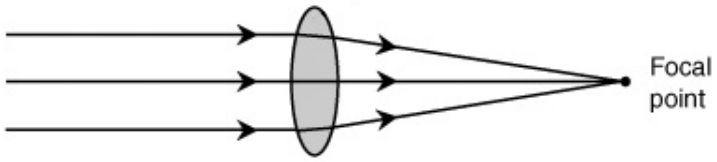

Figure 2.6: Collimated Light Focusing to a Single Point

Another aspect of real star imagery is that each object in the camera's FOV is for practical purposes essentially the same distance away. This is important when building a starfield because any deviation in distance from the camera will change both apparent brightness and angular distance in the identical patterns. This was investigated by Jorge Padro, who previously worked in the SimSat star dome, and his findings revealed the image plane is distorted if the camera does not view the same scene at the same angle with respect

to the camera focal plane and the same distance [20]. This is shown in Figure 2.7, where *e* is the distance by which the image is stretched. Accurate angular distance measurement is hugely important for searching the star catalog quickly, as explained in Section 2.4.3. Thus, having a spherical starfield offers a large advantage for star trackers that will move about some fixed point.

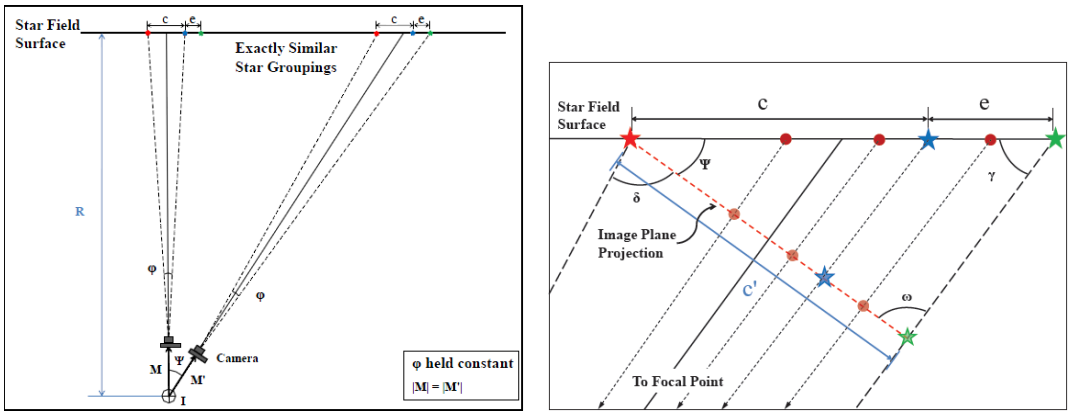

(a) Padro Graphic 1

(b) Padro Graphic 2

Figure 2.7: Flat Surface Analysis [20]

2.2.2 Using Light Emitting Diodes to Represent Stars.

Both of the methods utilizing LEDs that will be discussed involve spherical star field surfaces, so the unit distance issue is mostly resolved. This is important to note because one advantage of LEDs is that they can be powered and placed individually, thus following the contours of the sphere well and allowing variable brightness control. The first approach involves utilizing LEDs connected to fiber optic cords. This approach mimics the point source attributes of real stars.

Using fiber optics to send an LED's light to the surface of the star dome allows real star-like qualities, which is essential for testing real star trackers. This is the method used by the John Hopkins University/Applied Physics Laboratories (JHU/APL) Celestial

Object Simulator, 100 LEDs were used to mimic the brightest 100 stars present in the north hemisphere [3]. The dome had less than a 0.4% radial variation, which was deemed insignificant enough to not be a major source of error. By utilizing a laser positioning system and drilling holes for each individual fiber cord, the position of each light source was fixed accurately; however, this method fixes the relative and absolute positions of each stars. Changes can only be made by drilling new holes in the dome, which would most likely require recalibration and alignment to ensure that the work did not change the known position of each point source.

Another LED implementation that was used in prior work at AFIT involves individual LEDs arranged in a 3x3 grid. The first problem with this system occurred with the directional output of the LEDs, which is shown in Figure 2.8 [20]. If the brightness of the LED is dependent on the viewing angle, then the same LED will appear brighter when viewed in the middle of the camera's FOV versus at the edge of the FOV. This could cause errors in star recognition and an incorrect attitude solution. Another issue with this approach is that having a 3x3 grid of LEDs only leaves 5 possible different angles between LEDs. Limiting the possible angles between LEDs has effects on the star catalog search method (which uses angles between two stars to narrow the search) and limits the total number of unique recognizable starfields.

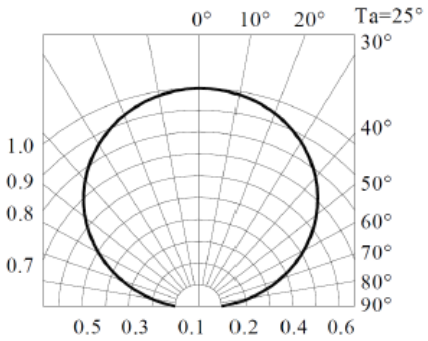

Figure 2.8: LED Radiation Pattern Plot

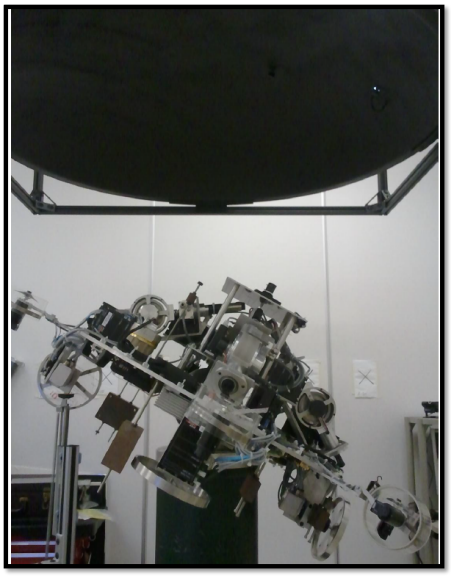

Figure 2.9: SimSat with 3x3 LED Grid on Dome Above

Another aspect of creating unique starfields is how many different levels of brightness the LEDs can be powered to. The previous investigation into the 3x3 grid of LEDs utilized an Arduino to power each LED through pulse-width modulation (PWM). Utilizing this method, there were only five different PWM duty cycles that could be recognized as reliably distinct by the camera [20]. Using Equation (2.11), this limited the total number of unique combinations possible to 75.

$$N_{uniquefields} = N_{angles}\frac{(N_{PWMlevels}+1)!}{2(N_{PWMlevels}-1)!} \tag{2.11}$$

where $N_{uniquefields}$ is the number of unique LED fields, N_{angles} is the number of *unique* angles between LEDs, and $N_{PWMlevels}$ is the number of different brightness levels that can be uniquely discerned by the camera.

This is a huge problem, because based on the camera's FOV at the start of this research, there would need to be at least 178 3x3 grids to ensure that at least one star pattern was always visible. Increasing the grid size of the LED panels would result in a larger non-

spherical surface and more possible angle distortion as discussed in Section 2.2.1. Solutions involving increasing the camera's FOV also have drawbacks and will be discussed in Section 2.3.2. Utilizing pixel-based screens allows a much larger number of possible angles and resolves the issue of not having enough unique combinations to fill out the starfield.

2.2.3 Using Pixels to Represent Stars.

Other methods for creating starfields have utilized pixelated displays. These displays have an advantage over the previously described LED methods of being able to be changed through software. Screens also offer pixel grouping solutions that allow many more possible angles between stars. However, the screens used thus far for starfield representation have been flat. This is not a large issue if the star tracker is fixed in place and only views the same portion of the screen. If rotational range of motion is desired, then there will be errors from angular distortion since the surface will not always be the same distance away from the camera. Utilizing pixelated screens is ideal if testing the star tracker's response to a moving image (satellite movement relative to the fixed background) and a variety of possible fields. The Star Field Simulator is one such testbed that allows testing of star tracker FOV, brightness range, star motion, and visual magnitude calibration. The Star Field Simulator was built to test the Fixed Head Star Tracker (FHST) that were used with the Space Shuttle's Spacelab Instrument Pointing System. This system utilized a monitor with 4096x4096 addressable pixels, whose intensity can vary to simulate a relative output range from 2 to 8 visual magnitudes [31]. This system could be used to test different star trackers after closed loop calibration was completed to adjust the output of each pixel, with count rates from 0 to 4095, to the star trackers sensitivity range. This approach is effective for optical response testing of star trackers; however, for full simulated satellite testing, a testbed that allows movement is required.

The Naval Postgraduate School (NPS) Three-Axis Simulator-2 (TAS-2) is one such satellite testbed that was used to test star tracker pattern recognition algorithms as part of a

2009 thesis effort by Jack Tappe [28]. The focus of the research was utilizing simulations to prove several pattern recognition algorithms and then implementing them on the TAS-2. The LCD screen above the TAS-2 displayed a total of nine stars. The tests on the TAS-2 yielded mixed results, only ever recognizing a maximum of seven of the nine stars and requiring an initial guess from -3 to 6 degrees to even find a solution. While the experiment was not necessarily aimed at creating a simulated star tracker system, it does shed light on possible issues when creating a simulated star tracker.

Some of the problems related to cataloging the angles between stars arose because the entire screen is viewed instead of a locally aligned region. This stems from the larger FOV lens with an 8.5 mm focal length and the completely flat screen. When designing the AFIT simulated star tracker, Jorge Padro got around this issue by using a smaller FOV lens (35 mm focal length) and having a spherical surface. The method developed by Padro is shown in Figure 2.10. This method allows the distance of two stars to be measured in the body frame (which is centered at the dome's center) and then correlated to an angle measured in the star tracker image frame. Since the star field surface at AFIT is mostly spherical, apparent brightness or angle differences across the FOV can be attributed to optics issues, such as the depth of focus across the image.

Although pixelated screens allow star movement, software based starfield changes, and many possible star angles, they are poorly suited for use with dynamic test beds because they are usually large flat surfaces. Utilizing smaller displays affixed to a spherical surface could allow the benefits of both a spherical surface and pixelated display to be realized. On small scales, an LCD screen's back light may bleed over the edges of the display and cause false star recognition; however, an organic light emitting diode (OLED) display does not require a back light and also has a large viewing angle (up to 160 degrees). In general, OLEDs have gained in popularity recently because of their self-emitting property, high luminous efficiency, full color capabilities, wide viewing angle, high contrast, and

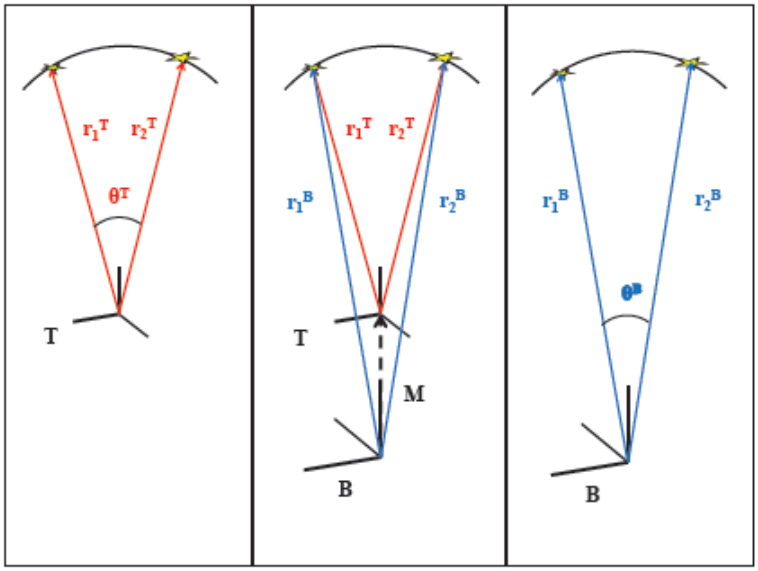

Figure 2.10: Algorithmic Vector Frame Transformation [20]

low power consumption [7]. For these reasons, 0.96 inch diagonal programmable OLED displays were chosen as the display elements for the SimSat star dome full population. See Chapter 3 for more details on the specifics of the chosen OLED display performance.

2.3 Starlight Acquisition

After covering typical light source approaches, the next point in the information chain is the star camera. This section covers the history of star trackers, which explains the generational differences between star trackers and how they developed. Then star tracker technical aspects such as mass, FOV, and other considerations are covered to understand the composition of past and current systems. Next star tracker accuracy considerations such as noise equivalent angle (NEA) and absolute accuracy are covered to understand the best way to describe certain aspects of the total accuracy. Last, calibration techniques are briefly discussed to explore ways to remove systematic errors and increase overall accuracy.

2.3.1 Star Tracker Historical Development.

Star trackers have been an essential part of high accuracy attitude determination almost since spaceflight began. Originally, star trackers had extremely low bandwidth and were used to update the attitude solution from gyro-stabilized platforms [21]. These star trackers were not fully integrated units and could not produce an attitude solution themselves, they either had to rely on the flight computer or even ground stations for processing of the data. These first generation star trackers could be accurate up to 10 arcseconds, but they could not solve the Lost in Space problem and required known stars to be identified in the FOV [11]. Solving the Lost in Space problem requires not only storing a large catalog of all stars that could be picked up by the star tracker, but also finding a way to effectively search that catalog to find the stars that were within the FOV.

As these problems began to be addressed with more powerful microcomputers and less massive memory storage options, star tracker units that were able to operate autonomously began to be developed in the mid 1990s. The key differences that warrant generational change are:

- The Lost in Space problem can be solved with a fully internal catalog of over 20,000 stars.
- A much larger average number of stars are utilized in the FOV, from 25 to 65, which improves the accuracy and the likelihood of a solution across the whole sky
- Image compensation techniques are performed internally to the star tracker system.
- Spacecraft attitude quaternion is output directly by the star tracker system. [5].

These second generation units have almost exclusively relied upon Charge-Coupled Device (CCD) imaging technology, developed by the Jet Propulsion Laboratory (JPL) in the early 1970s, with the first astronomical imagery use in 1976 . CCDs are pixel-based

sensors that consist of an array of photo-detector junctions or photosites that are discharged proportionally to how many photons strike the photosite [2]. Recent research has also began looking at Active Pixel Sensor (APS) based star trackers. According to Liebe *et. al.*, APS technology advantages over CCD sensors include lower power consumption, higher dynamic range, higher blooming threshold, individual pixel readout, single voltage supply operation, and the capability to integrate on chip timing [13].One big potential drawback to APS technology is that each pixel may have different photo-sensitivity, which can be very important for star tracker imagery. The main advantages from APS technology can be condensed into a simplifying of the star tracker support hardware (power consumption, single voltage supply, on chip timing) and having lower changes of saturation problems (higher dynamic range and higher blooming threshold). While these aspects may be beneficial, the availability of reliable, high resolution, and relatively cheap CCD technology cameras pushed the SimSat simulated star tracker in that direction.

More recent research in star tracker technology has lowered star tracker error values into the tenths of arcseconds and also focused on tracking moving images with higher update rates. For example, in 2004 the Ball Aerospace High Accuracy Star Tracker (HAST) achieved 0.2 arcsec total 1-sigma error while moving under 1 deg/sec [18]. This was done using existing CCD technology at a higher sample rate. Even though the HAST outputs individual star positions every 2 Hz, the actual CCD sensor can be sampled between 10 and 100 Hz, thereby providing many images of the same scene with only small deviations in time to aid in tracking [18]. Because of this higher sample rate, the integration time of the CCD was lower and the star tracker could not get enough photons in from the fainter stars to resolve them. This example illustrates some of the current state of the art in star trackers and also shows the design space trades as faster computers are able to handle the processing components more easily, The ultimate limitation in accuracy becomes the optics and photon counts required to image the stars.

2.3.2 Star Tracker Technical Characteristics.

To understand what variables to change to improve the accuracy of the current AFIT SimSat star tracker system, the different star tracker technical characteristics need to be examined. These characteristics are summarized from Eisenman *et. al.* as follows:

Field of View.

The size of the FOV is crucial to star tracker accuracy and operation. FOVs range from a few degrees to over thirty degrees diagonally. Narrowing the FOV causes the following:

- Increased angular resolution per pixel, resulting in linear increase in pitch and yaw accuracy (non-boresight axes).
- A larger lens aperture will be needed if the average number of stars in the FOV is expected to stay constant , because this increase in aperture will allow the detection of more numerous dim stars.
- A larger star catalog since the collecting aperture of the lens allows more stars to be detected. This means increased complexity of the pattern recognition of star constellations.

Sky Coverage.

Sky coverage is the percentage of the sky over which the star tracker will operate and provide an attitude solution.

Mass.

The mass of a star tracker is especially important for microsatellites. When it is possible to implement a star tracker on a few integrated circuits (ICs), the mass of the optics will dominate, which gives an advantage to wide FOV optics since the aperture would not need to be as large to have the same number of stars in the FOV.

Update rate.

The update rate of the star tracker depends on two factors: the exposure time and the

processing time for the image. The longer the exposure time, the more photons are utilized and the better the signal-to-noise ratio. However, the entire attitude control subsystem relies on how accurately the attitude can be extrapolated to a specific time. Therefore, exposure time and accuracy are trade-offs for a stable platform, depending on spacecraft dynamics [5].

For the SimSat star tracker, the main requirement is based upon the accuracy attitude solution. Satisfying this requirement thus means having a small enough FOV to have a small angular resolution per pixel to locate each star in the image and form an accurate vector set. The current camera used on SimSat is a Lumenera Lu205c 1600x1200 resolution full color camera with a pixel pitch of 4.2 micrometers and currently uses a 35 mm focal length lens (longer focal will mean smaller effective FOV). This sensor size and focal length can be used in Equation (2.12), which is

$$\phi_{pixel} = 2 \arctan\left(\frac{d_{pixel}}{2 \times FocalLength}\right) \tag{2.12}$$

where ϕ_{pixel} is the angular FOV for a given pixel and d_{pixel} is the size of the pixel in the same units as the focal length, which is millimeters in this case. Applying this equation to the SimSat camera results in each pixel having an angular resolution of 24.7 arcseconds However, the actual angular position resolution of a star can be improved by utilizing centroiding techniques covered in Section 2.4.2. Angular resolution per pixel will be able to provide a figure of merit to compare to when utilizing other optics with different focal lengths. The SimSat star tracker FOV will drive how many OLED panels are required to fully populate the dome and fill the "sky coverage" (which is a thirty degree cone about SimSat). The rest of the technical characteristics are mostly related to secondary objectives of this research, although update rate does tie into another piece of the accuracy puzzle: exposure time, which is also linked to aperture setting.

Another star tracker technical characteristic that is taken for granted in the previous list was the aperture setting. Eisenman briefly mentioned it in the FOV section when referring to fixed f/no (f-number) optics; however, understanding aperture settings in more detail is crucial to improving the accuracy of the SimSat star tracker. Camera's are usually specified by their focal length and f/no. This is because exposure time is proportional to the square of the f/no since the flux density at the image plane varies as $(D/f)^2$, where D is the current aperture diameter and f is the focal length [9]. The square root inverse of this flux density is defined as the f/no, or f/D. Some common f/no settings are shown in Figure 2.11. Notice that they increase by a factor of $1/\sqrt{2}$, which corresponds to a decrease in flux density by half.

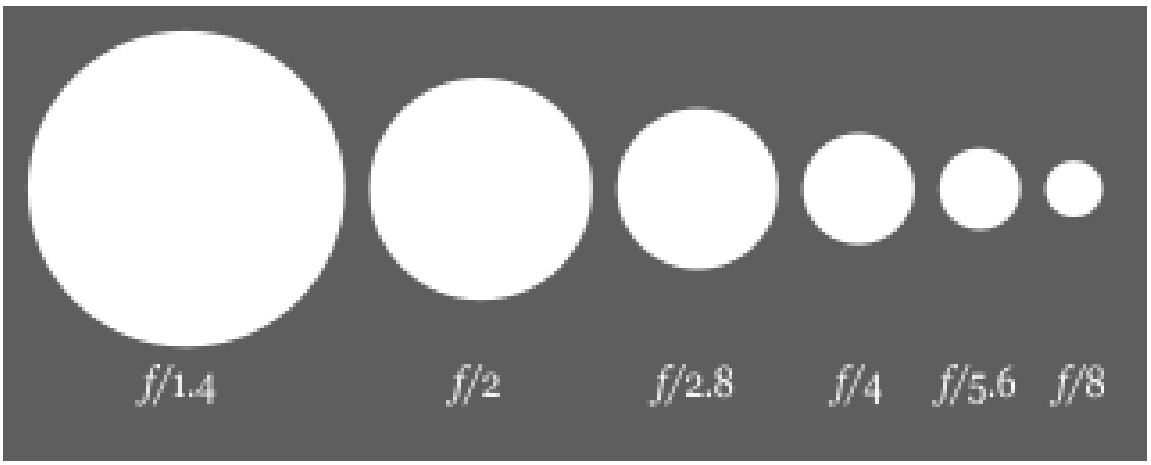

Figure 2.11: Various f/no Aperture Settings

The problem that arises with decreasing the flux density, either by decreasing the aperture and/or the exposure time, is that there will be a smaller signal-to-noise ratio in the image for a given star. Since CCDs are basically counting photons that have been converted into electrons, the output levels roughly follows a Poisson distribution and since

the signal-to-noise ratio is the signal divided by the noise, it can be described simply by Equation (2.13) [2].

$$SNR = \frac{p}{\sqrt{p}} = \sqrt{p} \tag{2.13}$$

Decreasing the aperture does have some beneficial effects in that stray light is also decreased by a rate slightly higher than more directed light. This property was utilized in previous research to allow intensity thresholding of the image [20]. Another beneficial aspect of decreasing the aperture setting is that the depth of field in an image will increase. Depth of field refers to the depth of the image that remains in focus away from the actual focal point. This concept is shown in Figure 2.12.

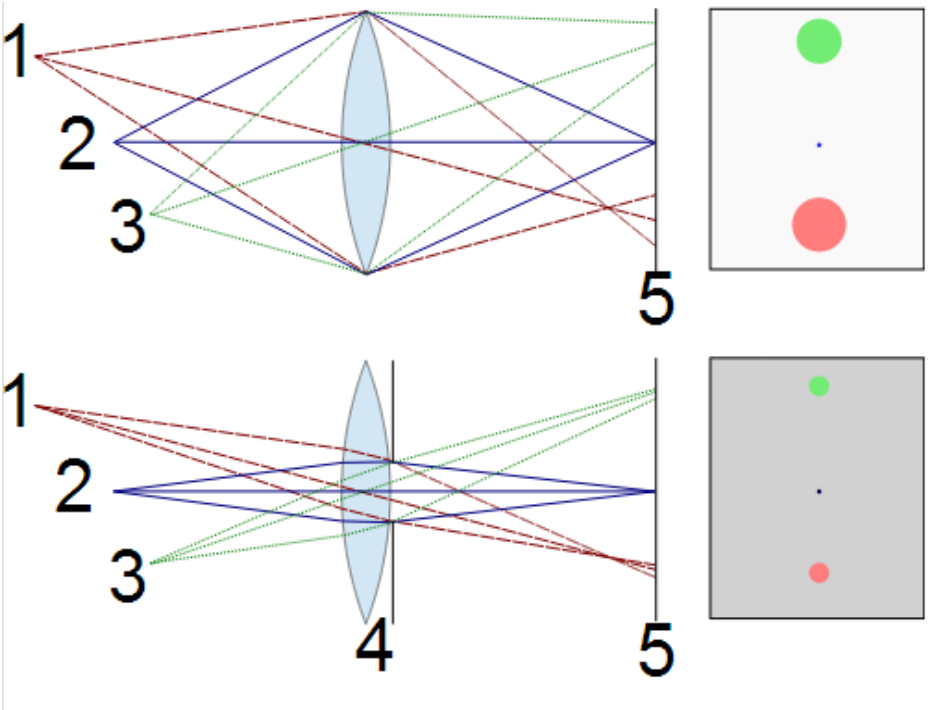

Figure 2.12: Depth of Field Increases with Smaller Aperture: Notice the Spot of the Out-of-Focus dots (1 and 3) are Tighter when the Aperture is Decreased

In Figure 2.12, the bottom lens has a more tightly closed aperture than the top lens. This reduces the overall light intensity hitting the sensor, as indicated by the darker color. However, the red and green circles are also forming tighter circles since their light rays are more focused when the aperture is decreased, even though they are away from the focal point of the lens. This may be beneficial on SimSat since we can control the light output depending on the source chosen. It is possible to sacrifice some star light intensity for increased focus across the image. Given the close distance to the dome and that the edges of the FOV will always be closer to the camera than the center, the entire image will never be in focus at full aperture. A description of the effects on the accuracy of the star tracker by each of the technical characteristics described in this section is one of the main goals of this thesis effort.

2.3.3 Star Tracker Accuracy.

The accuracy of a star tracker stems from a combination of its optics, sensor performance, and architecture decisions. The main error components as paraphrased from Allan Eisenman and Carl Liebe [6] as follows:

LOS uncertainty.

The line of sight (LOS) uncertainty is the angle between the camera boresight axes and the body axes. The uncertainty consists of thermal drift, ground calibration residuals, and launch effects. Usually its initial value is measured in a laboratory with simulated stars which can be precisely referenced to the star tracker.

Relative accuracy.

Relative accuracy is often referred to as star tracker accuracy because it measures how accurately the star tracker can detect changes in attitude. The components of relative accuracy are noise equivalent angle (NEA), optics error, centroiding error, and algorithmic errors.

Noise Equivalent Angle.

The NEA is a random error component which represents the star tracker's ability to reproduce the same attitude when it is continuously presented with the same star image. The NEA consists of readout noise, dark current noise, stray light noise, and photon noise. In real star trackers the NEA is primarily inversely proportional to the square root of the number of stars in the image.

Optical errors.

Optical errors include ground calibration error, thermal distortion, and chromatic, optical distortion and point spread function (PSF) variations over the focal plane.

Centroiding errors.

Centroiding errors include pixel light sensitivity, non-uniformity, quantization error, centroid algorithm uncertainty, and CCD charge transfer efficiency (CTE) effects.

Algorithmic errors.

Algorithmic errors include time stamp, thresholding, and *star catalog uncertainties* [emphasis mine], erroneous star matches, and algorithmic approximations [6].

While most of these same errors will be present for the simulated star tracker being used for SimSat, there will some important variations. Launch effects are not a concern; however, similar issues might occur when the SimSat star dome is moved from its bolted down vertically position on the optics bench to its horizontally supported position above SimSat. Thus instead of the camera unit being affect by gravity release and launch stresses, the star field itself may warp from changes in stress applied by the different supports. The SimSat star tracker also will not undergo much thermal variation over time as it will always be kept indoors. There is one component of the star tracker error that will be more magnified in this case than in a real star tracker design: the inertial star catalog position uncertainty. The star's position will be measured using a coordinate measuring machine (CMM). The CMM used in this research was the FaroArm Edge with a 6 mm

probe from FARO Technologies Inc. The volumetric accuracy of the FaroArm Edge measurement arm is 0.091 mm in the full 3.7 meter working volume case [10]. Using this uncertainty value to find the angular uncertainty in each star's catalog position can be estimated with the equation

$$\Delta\phi_{cat} = \tan^{-1}\left(\frac{\Delta P}{R_{dome}}\right) \tag{2.14}$$

where ΔP is the positional uncertainty of each star's catalog position, R_{dome} is the distance from the dome surface to the center of rotation, and $\Delta\phi_{cat}$ is the angular uncertainty for each star's position. Applying this equation with the 0.091 mm FaroArm Edge accuracy and the dome radius of 1219.2 mm yields an angular uncertainty of 15.4 arcseconds. This is just the uncertainty for a single star, so by combining many stars in an image, the absolute best possible accuracy of the system may be better. However, this value is much higher than the Hipparcos catalog uncertainty of less than 1 arcsecond for most stars. Thermal effects should be minimal since the SimSat room is kept at room temperature year round. Some of the main error sources may come from the optics, since relatively inexpensive lens have been used so far. To try to mitigate this, calibration techniques can be employed.

2.3.4 Calibration Techniques.

Errors are introduced into an optical system through lens distortion. Lens distortion is the result of the lens not behaving like an ideal pinhole camera, so mapping points from an image to the sensor may not follow a straight path. For star trackers, this means that stars not directly on the optical axis will be pictured further away from or closer to the optical center than would be expected using a simple pinhole model for the optics [14]. Two basic manifestations of lens distortion are barrel distortion and pincushion distortion, which are shown in Figure 2.13.

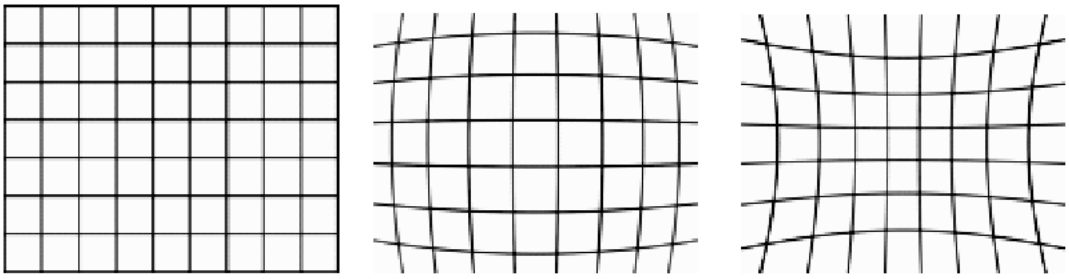

(a) Distortion Free Image (b) Barrel Distortion (c) Pincushion Distortion

Figure 2.13: Camera Image Distortion Types

In order to discover what type of distortion a lens may suffer from, a rectangular grid can be imaged and then distortion coefficients can be estimated from the alteration of the straight lines [14]. This can allow the image to be corrected back to a distortion free image by applying the distortion coefficients. Another approach is to estimate focal place coefficients from the distorted focal plane coordinates to determine the distortion [23]. This process can be quite complicated if there is also misalignment of the lens with the sensor. Applying this process to the SimSat star tracker system will be done if there is evidence that distortion is affecting the measurement. This could be investigated by measuring length deviations over the FOV. If there is evidence of distortion problems, then mapping of the lens' distortion can be done once a focal length is decided upon, which is discussed more in Section 3.2.3.3.

2.4 Star Image Processing and Cataloging

Once the light has been acquired by the optics and hits the sensor, the image is processed to search for probable stars. This section will cover the image processing aspect of star trackers. First, the image is "thresholded", which means it tries to filter out background noise and non-star objects by applying certain criteria that stars will likely fulfill, such as brightness levels. Then, the centroid of the leftover portions (assumed to

be stars) are calculated. From these centroids and brightness values, certain relationships between stars can be discerned which can aid in looking through the star catalog to find which stars are currently in the FOV.

2.4.1 Thresholding.

Star tracker image processing begins with finding the regions where stars are located. The first step in this process involves estimating the background noise and ignoring anything with a value lower than that noise level. This is known as *thresholding* because it sets the minimum intensity threshold that will be processed. Setting the intensity threshold depends on the range of star magnitudes that will be viewed and the camera optics setup. For SimSat star tracker purposes, it depends on the level of acceptable outside light on the dome, aperture setting and exposure time.

Thresholding can be a simple two step process. For example, in previous work on SimSat, potential stars must have a percentage of the maximum intensity seen in an image [20]. From these potential stars, potential small bright spots can be rejected by setting another threshold value, an "area" threshold. This setting rejects anything smaller than the area value listed, which is only really appropriate for certain testbeds where the "stars" may be larger than tens of pixels. Real stars are point sources that must be defocused to take up more than one pixel, but will still remain in a relatively small area.

2.4.2 Centroiding.

After thresholding, regions of interest (ROI) are established around stars so that the centroiding process may begin. Centroiding is a crucial portion of star tracker image processing. By slightly defocusing the light from a star, the light will spread out over several pixels, and allow location of the star with subpixel accuracy, as shown in Figure 2.14. The total brightness of the star is calculated by adding the magnitude of each pixel in the ROI [12]. The size of the ROI is usually set depending on the optics and estimation of the maximum star airy disc size.

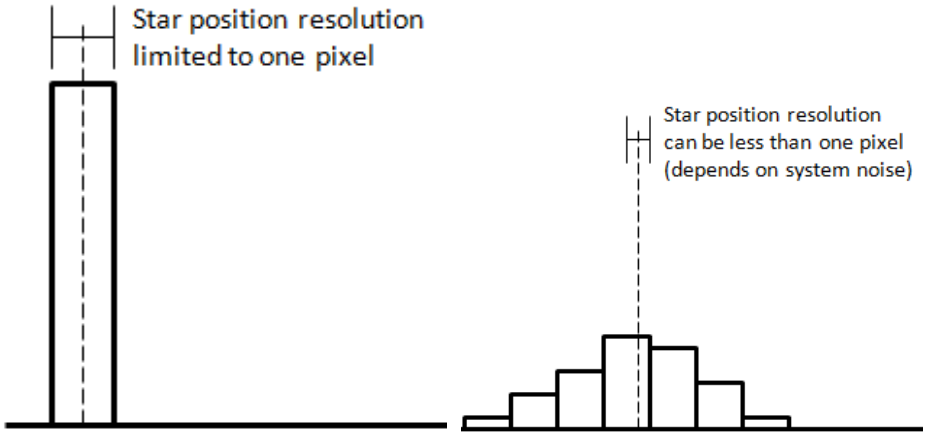

(a) Pixels From a Focused Star (b) Pixels From a Defocused Star

Figure 2.14: Centroiding Allows Sub-pixel Star Location Resolution

For SimSat purposes, the calculation of the centroid is simplified. Each contiguous pixel passing the threshold test is converted into a logical 1 or 0 and the area centroid is found [20]. Magnitude is found by adding the instrument magnitude of each contiguous pixel, which makes larger stars have a larger apparent magnitude even though their specific brightness might be the same. Specific brightness of a given source can be found be simply dividing the total magnitude by the area of the illuminated pixels. This could be useful for separating different color sources, which should have distinct specific magnitudes.

2.4.3 Star Pattern Recognition.

Now that the image has been processed to record the star's locations and brightness values, the catalog must be searched to match those stars to their inertial set. There are many stars with similar brightness and having an exact brightness search could lead to many errors. Instead of taking that approach, the current AFIT SimSat star tracker catalog searches using a common method of star pattern recognition. The architecture created by Jorge Padro is based upon the Boeing Star Catalog explained in detail by Needelman *et. al*[19]. The essential aspects of the system are that it uses angular separation between stars

to sort them into pairs. A Pair Catalog (PC) is created along with the main Acquisition Star Catalog (ASC), which actually holds the star position and magnitude. The algorithm first looks for applicable pairs in the image, which are grouped into "buckets" in the PC. Each pair in the applicable bucket is linked to a star in the ASC, which is then checked for matching magnitudes. If the magnitude matches then a direct match test is performed using the two stars that formed that pair to test the solution. If a third star is matched from the rotation formed by the direct match test solution, then the solution is accepted. The full catalog can be used in the Lost in Space case to find a solution, while a limited scope search can be done based upon prior attitude knowledge if the system is operating in Normal mode.

Another approach to star pattern recognition is utilizing triangles and grouping stars by three instead of two. The planar triangle method connects neighboring stars into a triangle shape. This triangle's area and polar moment can be calculated from three stars unit vectors $\hat{b}_1$, $\hat{b}_2$, and $\hat{b}_3$ as

$$A = \sqrt{s(s-a)(s-b)(s-c)} \tag{2.15}$$

where

$$s = \frac{1}{2}(a+b+c) \tag{2.16}$$

$$a = ||\hat{b}_1 - \hat{b}_2|| \tag{2.17}$$

$$b = ||\hat{b}_2 - \hat{b}_3|| \tag{2.18}$$

$$c = ||\hat{b}_1 - \hat{b}_3||. \tag{2.19}$$

While two triangles may have the same area, they will most likely not have the same polar moment as well [27]. The polar moment is calculated through

$$J = A(a^2 + b^2 + c^2)/36. \tag{2.20}$$

With these two pieces of information, unique star triangles can be identified in an image. This method does have the drawback of requiring at least three stars in every image. Deciding on the right star pattern recognition algorithm usually involves trades such as speed versus memory space or constraints such as a limited number of light sources. Both of the methods discussed in this section will be considered when choosing a light source and building the star catalog for the SimSat star dome.

2.5 Attitude Determination Algorithms

The last step in coming to an attitude solution is to utilize the vector sets in an attitude determination algorithm. This section will briefly cover some of the attitude determination algorithms commonly used. First, deterministic attitude determination will be covered with the TRIAD algorithm. Then, a more popular approach, the optimal QUEST algorithm will be covered, which is optimal in the sense that if the uncertainty of each measurement is known then the QUEST algorithm will yield the most accurate solution. Then, some other algorithms are mentioned for completeness.

2.5.1 TRIAD Algorithm.

Once a set of vectors have been formed with representations in both the body and inertial frame then an attitude determination algorithm can be applied to find the rotation from the inertial frame to the body frame. Arguably the simplest algorithms that accomplish this task are deterministic and assume at least one measurement is perfect, not accounting for relative accuracy statistics of the sensors involved. The TRIAD algorithm is one such algorithm and is named TRIAD because it constructs two new basis triads from two measurements [27]. Assume that inertial vectors $\hat{V}_1$ and $\hat{V}_2$ have corresponding body frame vectors $\hat{W}_1$ and $\hat{W}_2$, then these vectors are related through the rotation matrix $\boldsymbol{R}^{\boldsymbol{bi}}$ as shown in Equation (2.21).

$$\hat{W}_1 = \boldsymbol{R}^{\boldsymbol{bi}}\hat{V}_1 \text{ and } \hat{W}_2 = \boldsymbol{R}^{\boldsymbol{bi}}\hat{V}_2 \tag{2.21}$$

However, since there are four pieces of information in the two measurements the algorithm cannot produce an exact solution for the rotation problem. The TRIAD algorithm solves this by discarding part of the second measurement when constructing the two basis triads, as shown in Equation (2.22) and Equation (2.23). This means that the TRIAD gives a solution that will perfectly match $\boldsymbol{R^{bi}}\hat{V}_1$ to $\hat{W}_1$, but will not exactly match the second vector set [24]. For this reason, the more accurate sensor should always be used as the first vector set in the TRIAD algorithm.

$$\hat{r}_1 = \hat{V}_1 \quad \hat{r}_2 = (\hat{V}_1 \times \hat{V}_2)/|\hat{V}_1 \times \hat{V}_2| \quad \hat{r}_3 = \hat{r}_1 \times \hat{r}_2 \tag{2.22}$$

$$\hat{s}_1 = \hat{W}_1 \quad \hat{s}_2 = (\hat{W}_1 \times \hat{W}_2)/|\hat{W}_1 \times \hat{W}_2| \quad \hat{s}_3 = \hat{s}_1 \times \hat{s}_2 \tag{2.23}$$

The two basis triads are put into observation ($\hat{s}$ vectors) and reference ($\hat{r}$ vectors) matrices [24]. These two orthonormal bases sets are multiplied to find the rotation matrix solution, as shown in Equation (2.24).

$$\boldsymbol{M_{ref}} = \begin{bmatrix} \hat{r}_1 & \hat{r}_2 & \hat{r}_3 \end{bmatrix} \tag{2.24a}$$

$$\boldsymbol{M_{obs}} = \begin{bmatrix} \hat{s}_1 & \hat{s}_2 & \hat{s}_3 \end{bmatrix} \tag{2.24b}$$

$$\boldsymbol{R^{bi}} = \boldsymbol{M_{obs}}\boldsymbol{M_{obs}^T} \tag{2.24c}$$

The TRIAD algorithm is simple and can be calculated relatively quickly; however, there are severe limitations. While the TRIAD algorithm is simple and can be effective if the first vector set comes from a relatively accurate sensor, if more vector observations are available they cannot be added into the TRIAD algorithm and therefore the full array of information available may not be utilized. Other algorithms, such as the Quaternion Estimation (QUEST) algorithm are optimal estimates and can take in any number of vector observations.

2.5.2 QUEST Algorithm.

An optimal estimate of the attitude of the spacecraft can be obtained through the minimization of a loss function, which measures the deviation between the body frame vectors and the rotated inertial vectors. This can be represented through a quadratic loss function involving n vector sets, such as the one shown in Equation (2.25).

$$L(\boldsymbol{R}^{bi}) = \frac{1}{2}\sum_{i=1}^{n} a_i|\hat{W}_i - \boldsymbol{R}^{bi}\hat{V}_i|^2 \tag{2.25}$$

The weights a_i can be used to weigh different vector sets as more important than others depending on the accuracy of each respective measurement and their sum can be set equal to one ($\sum_{i=1}^{n} a_i = 1$). The development of the QUEST algorithm involves first turning the problem into a maximization problem by changing the loss function into a gain function:

$$g(\boldsymbol{R}^{bi}) = 1 - L(\boldsymbol{R}^{bi}) = \sum_{i=1}^{n} a_i \hat{W}_i^T \boldsymbol{R}^{bi}\hat{V}_i \tag{2.26}$$

At this point the problem is approached by breaking $\boldsymbol{R}^{bi}$ into its equivalent quaternion representation and then finding a bilinear form of the problem that incorporates the quaternion constraints [24]. The solution is a quaternion that is an eigenvalue of this bilinear form of the gain function and quaternion constraint. The QUEST algorithm can accommodate more measurements and directly output a quaternion, although it is computationally slower than the TRIAD algorithm in almost all cases. For example, using two measurements for both algorithms the TRIAD algorithm found a solution in 143 floating point operations, while the QUEST algorithm took 190 [15]. The accuracy comparison between the two methods depends on the accuracy variation between each vector set provided, but the QUEST algorithm will always minimize the loss function according to the weights a_i.

2.5.3 Other Algorithms.

There are several variations on the TRIAD and QUEST algorithm that have advantages in certain situations. Landis Markley investigates the processing time and accuracy of some of the more common variations: the Symmetric TRIAD, Optimized TRIAD, and various Direct Quaternion methods [15]. Applying these different algorithms may be prudent depending on the accuracy requirements, individual star local determination accuracy (both inertially and optically), and update rate requirements.

2.6 Summary

This chapter covered the foundation necessary to understand this thesis effort. Firstly, in Section 2.1, spacecraft attitude dynamics were presented to explain proper rotation representations and attitude determination mode basics. In Section 2.2, starfield representation methods were discussed so that real star light properties could be understood and compared to previous attempts to make indoor star trackers. In Section 2.3, star trackers' development and technical attributes were expounded upon to understand the relevant aspects in a simulated star tracker development. Then Section 2.4 discussed the ways that raw image data is processed into a meaningful set of inertial and body frame vectors. Finally, Section 2.5 briefly reviewed some of the algorithms used in determining a spacecraft's attitude from vector observations.

III. Methodology Development

The methodology employed in this thesis effort revolved around fully understanding what aspects of the star tracker and star dome system affect the accuracy of the solution. The approach changed during the course of the research as different elements were discovered to be more or less important. This chapter shows the development of that approach, and so some of the preliminary results are included to help make the narrative easier to understand. First, this chapter will delve into the test set up of the experimental apparatus on the optics bench and what was gained by separating the system from SimSat while the tests were being run. Next, preliminary studies were done using a few OLED panels to determine what aspects of the problem influenced the accuracy the most. Then, the method for fully populating the star dome is discussed. The software algorithm and star catalog of the system are also discussed. Finally, the accuracy validation approach used when the system was moved back to hanging above SimSat is discussed.

3.1 Optics Bench Test Set Up

The dome needed to be taken down from its position hanging about eight feet off the floor above SimSat, as shown in Figure 1.1, to make it easier to work on. This section covers the approach used to secure the dome to an optics bench to more precisely control the experimental environment. This allowed the dome to be rigidly fixed relative to the camera. This also facilitated the use of more precise rotation measurement stepper motors that could be used as a first check of the rotation accuracy. Moving the dome also had the advantage of allowing other students to work on SimSat for other research activities while permitting this thesis effort to focus purely on improving the star tracker system accuracy. The first step in moving the dome was building a cage so that the risk of the dome flexing or cracking during the move would be eliminated. After this was done, the dome was taken

down from above SimSat, recall Figure 2.9 and mounted to the cage. Then the entire cage was affixed to a large optics bench. Figure 3.1 shows the initial set up on the optics bench with the supporting cage brace circled in red.

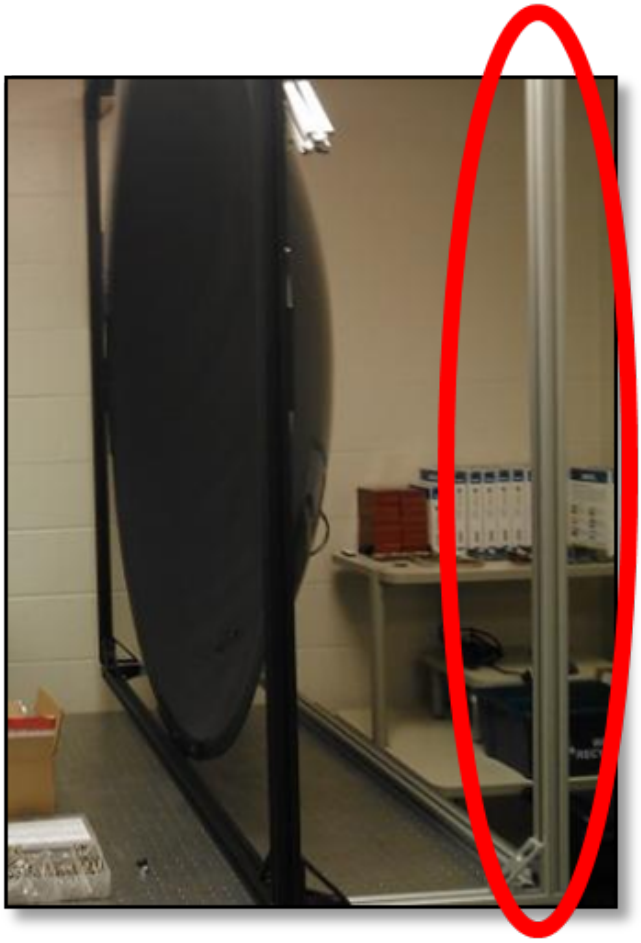

Figure 3.1: SimSat Star Dome Moved to Optics Bench

The next step was setting up the camera and rotation equipment near the center of the dome. The initial positioning was course and based on the dome's nominal specified spherical radius of 48 inches. This initial positioning allowed familiarization with the equipment, OLED panel programming, and image processing. The rotation equipment used to move the camera was two stepper motors from Thor Labs. The initial camera set

up is circled in red in Figure 3.2. In this figure there is also an inset of one of the panel patterns used for initial testing and familiarization.

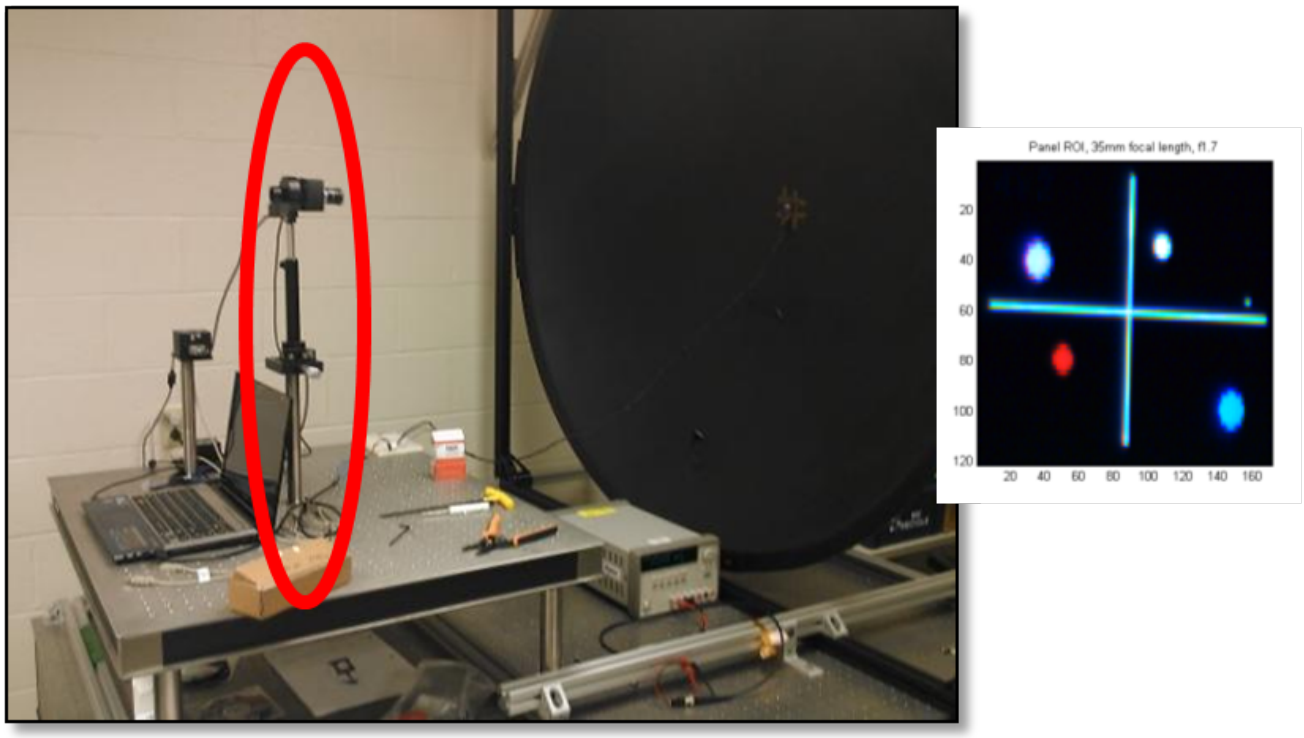

Figure 3.2: Full Dome Initial Setup, Panel Inset

The degrees of freedom of the camera rotation stages are shown in a more detailed CAD model in Figure 3.3. A Thorlabs PRM1Z8E motorized rotation stage was used to rotate the camera around the boresight axis (X-axis). This rotation stage has a reported bidirectional repeatability of 0.1 degrees, but can achieve a minimum incremental motion of 25 arcsec [30]. For the Z-axis, a Thorlabs CR1-Z7E motorized worm drive rotation stage was used since it can hold up to 25 lbs and has a reported repeatability of less than 0.0167 degrees [29]. For both of these motor stages, motor controller software allows the user to see the absolute rotation. For the optics bench test, there is no ability to rotate around the Y-axis. The cost and complexity of adding another precision rotation stage did not justify

the extra ability to test all three axes when about one-third of the dome's surface is still able to be tested with this much simpler setup.

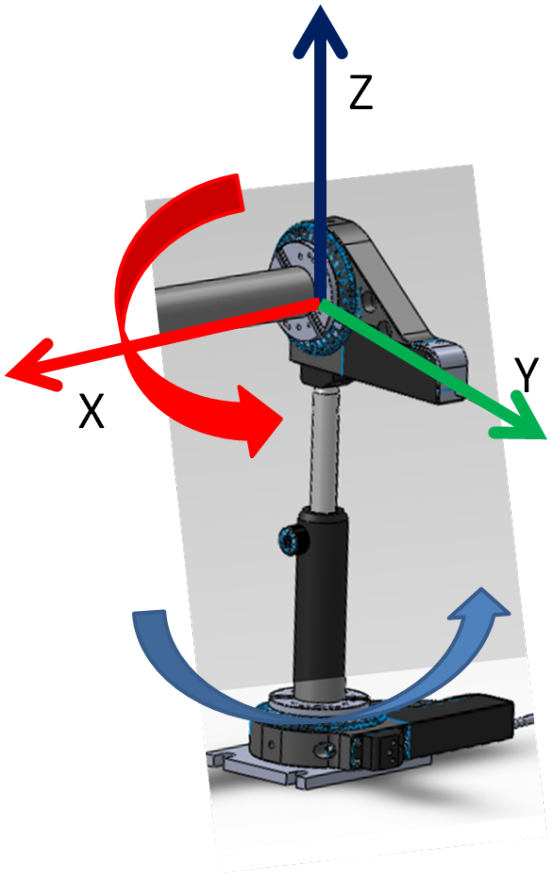

Figure 3.3: Rotation Stage Setup and Camera Frame Axes

With the dome set up as shown in Figure 3.2, the caged dome is cantilevered at one end. This setup is susceptible to even small forces that cause vibrations about the fixed axes whenever the dome was bumped. To minimize any possible displacement problems from a lack of stiffness during testing, a better mounting solution had to be devised to prevent any dome movement. By adding triangular braces running the length of the optics bench, the

top of the dome cage would be fixed as well which would greatly stiffen the system. This was done as shown in Figure 3.4, with the added triangular supports circled in red.

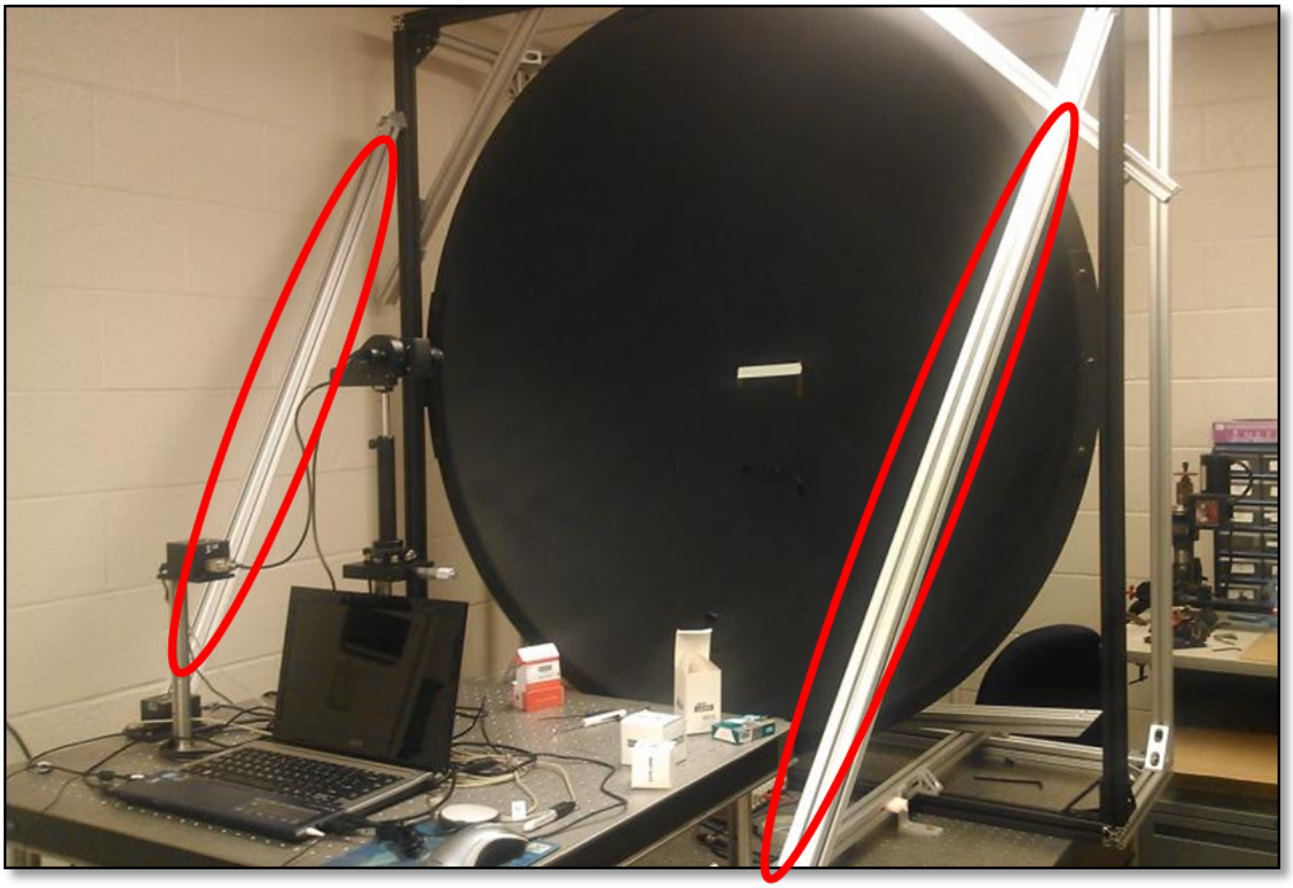

Figure 3.4: Stiffening Dome with Triangular Braces (Shown in Red Ellipses)

Once the dome was sufficiently stiffened, a FaroArm Edge coordinate measurement arm was used to locate the centroid of the dome, which is where we want to place the center of rotation for the camera rotation stages. Figure 3.5 shows the FaroArm Edge arm positioned next to the dome along with a plastic cover that was used to better control ambient light conditions, as needed. Even with the FaroArm Edge arm's reported ability to locate points in 3D space to less than one tenth of a millimeter, the dome's ellipsoidal shape

makes the actual centroid is more difficult to locate. The center of rotation was placed at the centroid calculated by the FaroArm. Since the dome is not a sphere, the centroid used will not necessarily be the center of rotation, so the system's absolute accuracy will suffer unless this can be adapted for through software, which is discussed later in Section 3.4.

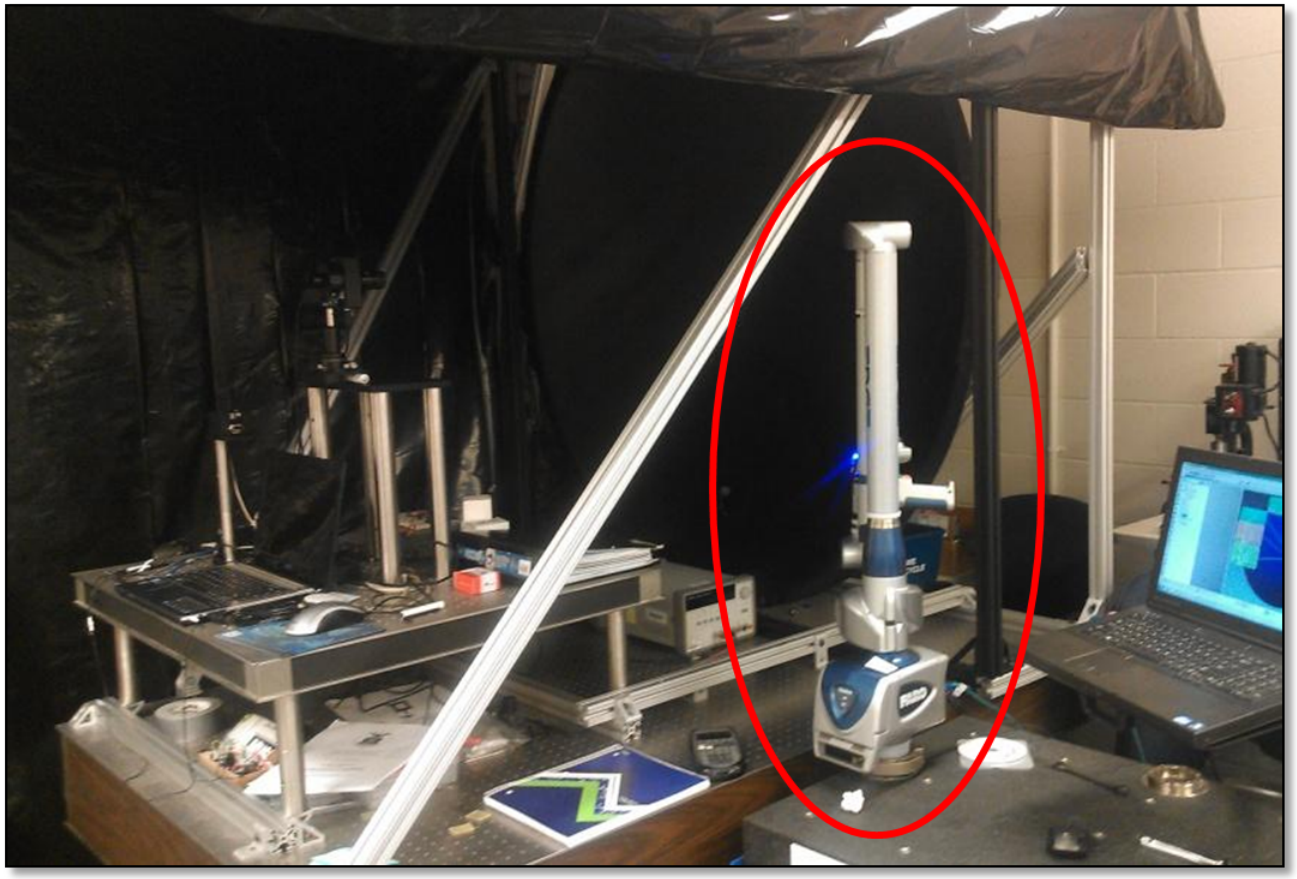

Figure 3.5: Dome Setup with FaroArm (Shown in Red Ellipse)for Finding Centroid of Dome "Sphere"

The FaroArm Edge will also be used later to test a catalog building method by measuring known points on the panel and for accuracy verification. Once the dome setup was complete, testing various aspects of the camera, lens, and light sources began with the goal to reduce noise in the system.

3.2 Preliminary Accuracy Tests

Since noise and accuracy of this star tracker system is of great concern, we will now go into more depth about the process used to determine what are the significant terms that cause an increase in noise or a drop in accuracy. In this section, the noise equivalent angle (NEA) will be further discussed since that is the noise floor of the system. Then each "subsystem" (light sources, light collection, and algorithms) will be examined to see what the effects are on the NEA. Preliminary results are shown here because the analysis derived from them reveals the thought process used to drive the methodology forward and ultimately come to a better pseudo-star-tracker system.

3.2.1 Reducing Noise Equivalent Angle.

Before delving into the subsystem level analysis of the error in the star tracker system, it is beneficial to expand upon the NEA, which is a main figure of merit for the system's accuracy. The NEA of a star tracker determines the smallest rotation that the system can discern because the NEA represents the rotation amount that the tracker will record when seeing the same optical stimulus with no actual rotation. All star trackers have the poorest accuracy about the camera boresight axis, as discussed in Section 2.3.3. Which is also true in our system, as shown in Figure 3.6. In this figure, 3-2-1 Euler Angles are used to calculate the rotation recorded about each axis. Only one OLED panel is used and it has five stars of different magnitudes. Forty images are taken and the rotation calculated is recorded (see Section 2.4.1 for original algorithm flow). The larger spread deviation about the X-axis (boresight) is what determines the NEA, which is the standard deviation of the measured rotations about zero when the camera is kept static. In this figure, the NEA about the X-axis is about 0.03°, while the other axes have NEA values in the low thousandths-of-a-degree range.

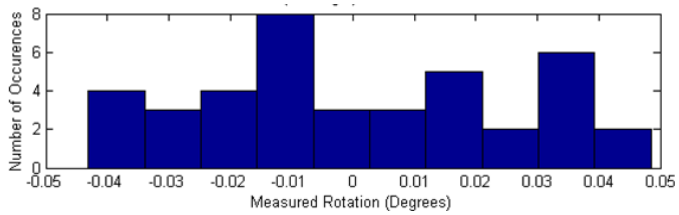

(a) Boresight (X-Axis) Calculated Rotation, $NEA_X = 0.03$ Degrees

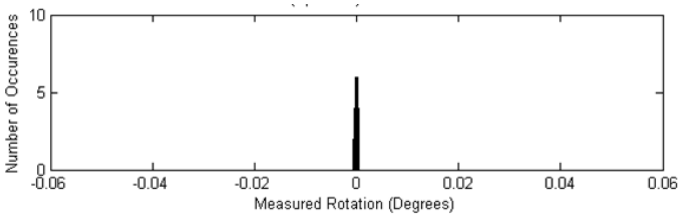

(b) Y-Axis Calculated Rotation, $NEA_Y < 0.0005$ Degrees

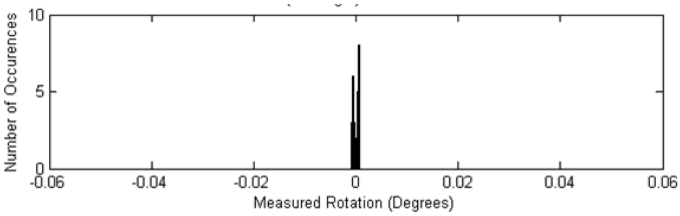

(c) Z-Axis Calculated Rotation, $NEA_Z < 0.0005$ Degrees

Figure 3.6: Initial NEA Testing Revealed Much Higher than Expected NEA about Boresight (X-axis)

Lack of repeatability about the boresight axis results from the noise of the system causing variation of the centroid locations. The initial reasoning behind the large boresight axis error is that it is affected most by this noise since it has centroid uncertainty in both off-axis components which determine the rotation. Studying the NEA_X value was the initial focus of the research effort so as to understand what affects this value and how to lower it. Clearly, discernible rotations need to be greater than the NEA for the system to accurately

record them. Many factors influence the centroid uncertainty, from star brightness to different optics settings.

Brightness levels are mainly used to help distinguish certain stars from other stars; however, brightness also affects the accuracy by changing the centroid variation of the system. For example, when contrast ratios were examined to see brightness differentiation levels, the NEA was also checked to see if only changing the contrast ratio affected the NEA. Figure 3.7 shows this problem, with the histogram in the middle showing the highest NEA value calculated from 40 frames at CR=5 and the histogram at the bottom with the lowest NEA value calculated from 40 frames at CR=11.

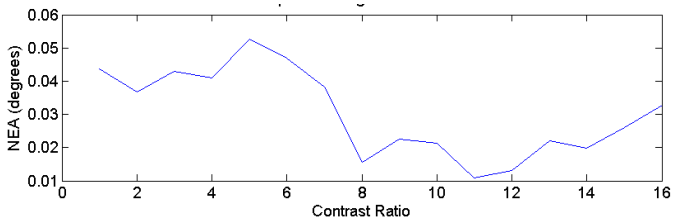

(a) NEA Changes with Contrast Ratio

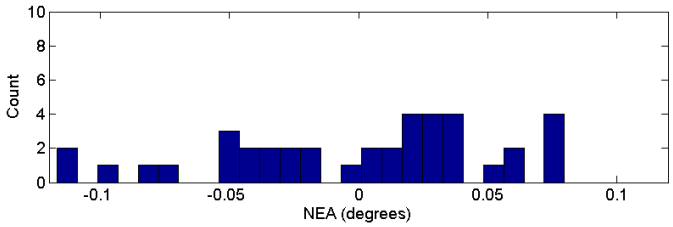

(b) Calculated X-Axis Rotations at Contrast Ratio=5

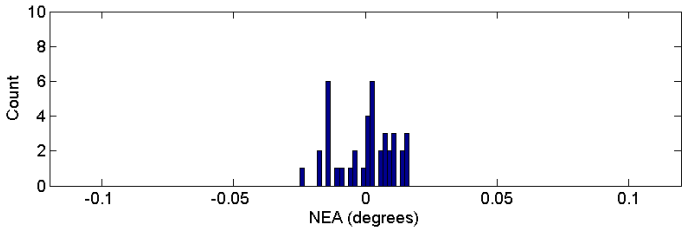

(c) Calculated X-Axis Rotations at Contrast Ratio=11

Figure 3.7: Contrast Ratio Affecting NEA

Figure 3.7 is meant to serve as an example of how one of the factors that should not directly affect the NEA value actually can have a large impact as the information travels through the system. Understanding these effects is essential to lowering the NEA and having the most accurate system possible.

3.2.2 Light Source Accuracy Effects.

Since the light emission is being controlled through the use of OLED panels, which is not true for real star trackers observing real stars, there are more parameters that we are able to be investigate and control to determine their effect on accuracy. First the number of stars in an image was examined. Then star size and star color were briefly looked at to see if there are any extreme cases. Contrast ratio was already discussed in terms of NEA, but it was also examined in terms of how many different brightness levels were discernible by the camera. Finally, the largest effect was found to be from the spread of stars in an image and inaccuracies accrued near small angles from the ambiguity of the axis of rotation.

3.2.2.1 Number of Stars.

The number of stars in an image should increase the accuracy of the QUEST algorithm. However, that assumes that all the stars have the same uncertainty in their location, which is not necessarily the case. Another important aspect of the number of stars in an image is the number of angles between star pairs that can be made on the panel. Calculating angles between stars on a panel is essential to the cataloging process in the interstar angle catalog method, which is what this research effort was initially using. Having more uniquely identifiable angles allows more unique catalog bins which can both make the catalog search faster and increase the number of total stars that can be placed on the dome for a given set of brightness bins.

In order to test if the camera could distinguish a single OLED pixel increase in distance between stars, stars were populated on the panel in the pattern shown in Figure 3.8a and

Figure 3.8c. Arranging the star rows horizontally and vertically was a check to ensure that there would be no surprises in the pixel sensitivity across either direction.

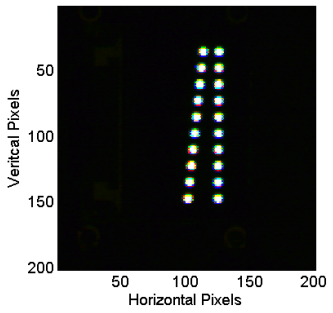

(a) Cropped Camera Image, Horizontal Angles

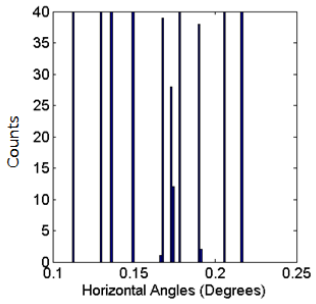

(b) Horizontal Angles Histogram, Zero Overlap

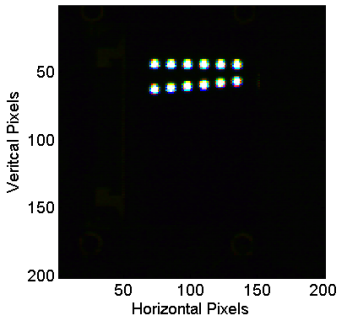

(c) Cropped Camera Image, Vertical Angles

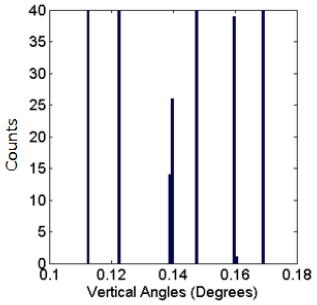

(d) Vertical Angles Histogram, Zero Overlap

Figure 3.8: One Pixel Increase in Angle between Stars at Center of FOV Shows Clear Unique Detection

Taking this data and fitting a linear relation allowed the expected angle to be seen on the camera once the OLED pixel distance was known. Figure 3.9 shows this linear relationship ($R^2 = 0.99$ in both lines).

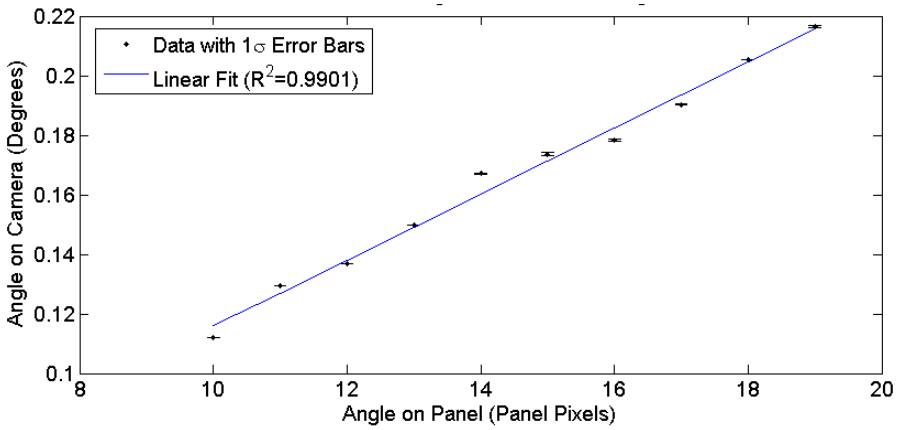

(a) Horizontal Angle Test OLED Pixel to Angle

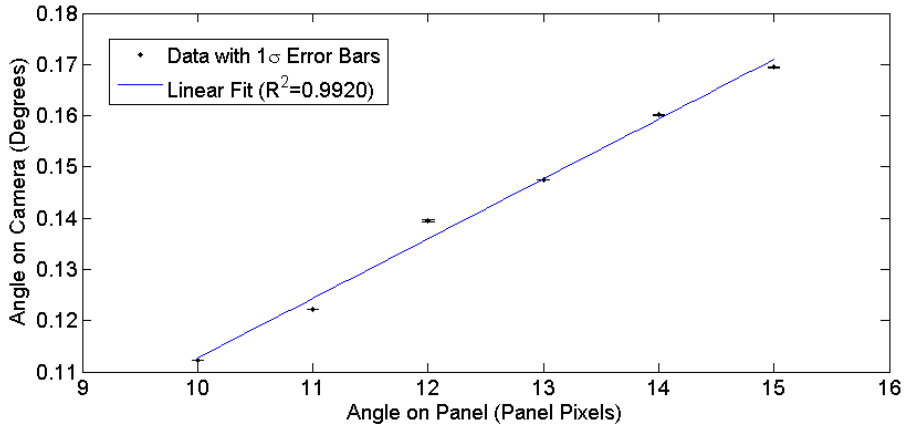

(b) Vertical Angle Test OLED Pixel to Angle

Figure 3.9: Linear Relationship Between OLED Pixel Separation and Measured Angle

This is as expected; however, most lenses have some amount of distortion, as discussed in Section 2.3.4, that will cause these angles to appear larger or smaller depending on where in the FOV of the camera they appear. To test the lens distortion of the camera and see if the linear relationship shown in Figure 3.9 could be used in cataloging efforts, the camera was rotated to put the panel around the edges of the FOV and to retest the angle measurements as shown in Figure 3.20, which will be discussed in more detail in Section 3.2.3.3.

3.2.2.2 Star Size.

Theoretically, the brightness of a star should not directly affect the accuracy of the attitude solution as long as enough light hits the sensor to make an accurate centroid since only the centroid of the star is used to create the vectors used in the rotation solution. Since the OLED panels used in this research can produce more than enough light to stimulate the sensor reliably, this should not be a large concern. To confirm this, many different brightness magnitudes were tested to see if their centroid uncertainty varied. Brightness is also crucial in star identification since having more uniquely identifiable brightness levels will expand the star catalog allowing for more total stars on the dome. The three aspects tested were star size, star color, and panel contrast ratio.

The effect of the size of stars was tested using nine white stars displayed on one screen as shown in Figure 3.10.

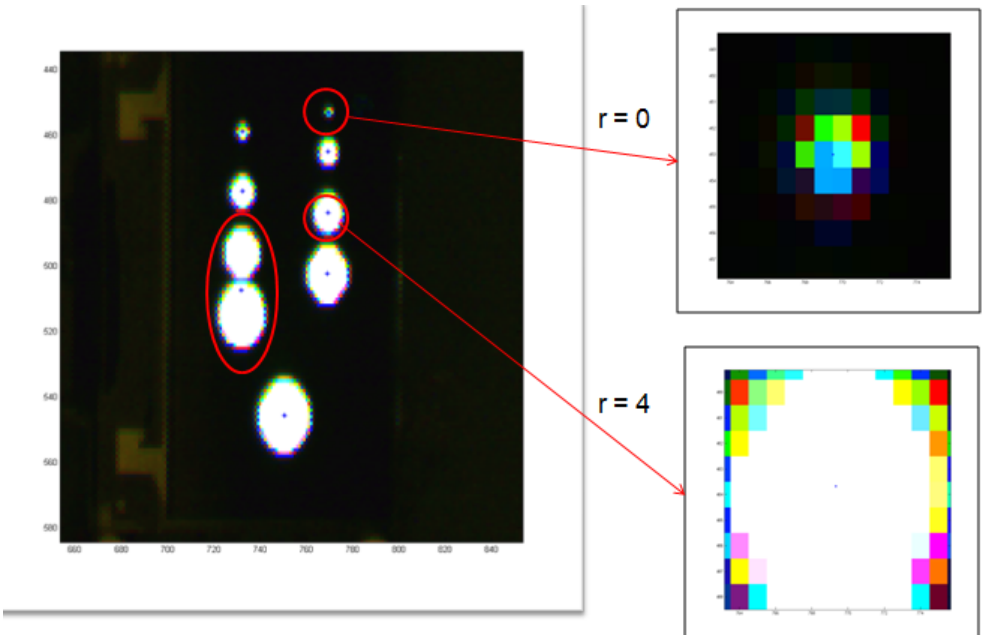

Figure 3.10: Star Size Shows no Clear Correlation to Centroid Variability

As shown in the inset figures on the right, the size of the star does impact the color interpolation algorithm inherent to the camera, as smaller stars have less bins to interpolate near and appear as their separate camera pixel base colors instead of white. The top inset star shows a radius zero star (a single OLED pixel is illuminated), while the bottom inset shows a radius four star.

Figure 3.10 also shows the centroid of two stars mixed together by the algorithm, shown by the leftmost red ellipse. This set a lower limit on how close stars can be to one another (two OLED pixels in distance). This terminology will be used going forward when describing star size. While there was no conclusive pattern with the variation of the centroids as the size of the star changed, it was later noticed that the centroiding algorithm may be coupled closely with star size in centroid uncertainty, which is discussed in Section 3.2.4 and shown in Figure 3.28. To limit the number of variables, star size was mainly used for brightness differentiation within a panel with stars of size radius one to radius five being utilized.

3.2.2.3 Star Color.

Star color was briefly analyzed during the preliminary portion of the research. The OLED panels can display many different colors and hues, some of which are picked up with more variance than others by the CCD. Figure 3.11 shows nine different colors tested for centroid variability over 40 images. It was found that orange and cyan colored stars had the least centroid variation; however, the star color is also closely coupled with star size and the centroid algorithm thresholding. To limit the number of variables, color was chosen to be white for further testing, since, after the importance of spreading stars around the FOV was discovered as discussed in Section 3.2.2.5, the focus shifted to algorithmic effects.

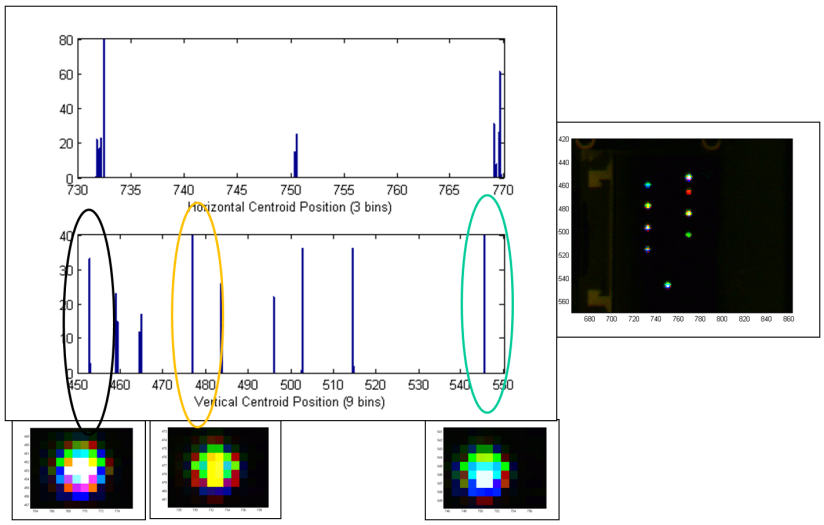

Figure 3.11: Preliminary Color Testing Revealed a Weak Dependence that is Confounded with Star Size (Ellipses Have Their Respective Star Images Shown Under Them)

3.2.2.4 Contrast Ratio and Brightness Bins.

Determining the maximum number of discrete brightness bins will determine how many unique star fields can be placed on the dome. Theoretically more stars per image will increase accuracy by the square root of N where N is the number of stars used in the QUEST algorithm. However, that assumes that all star measurements have the same accuracy, which is not necessarily true since different brightness values have different centroid measurement consistency values. Thus, more stars are usually better, especially if their centroid accuracy can be quantified so the algorithm knows which measurements to weight accordingly.

Thus far, white stars of varying size and contrast ratio have been investigated to determine how many unique brightness levels can be discerned using size 1-5 stars and using all available contrast ratios on the panel (1-16). By selecting the contrast ratios that have the least overlap (1,3,7, and 16), each star size was plotted in its own histogram, as shown in Figure 3.12.

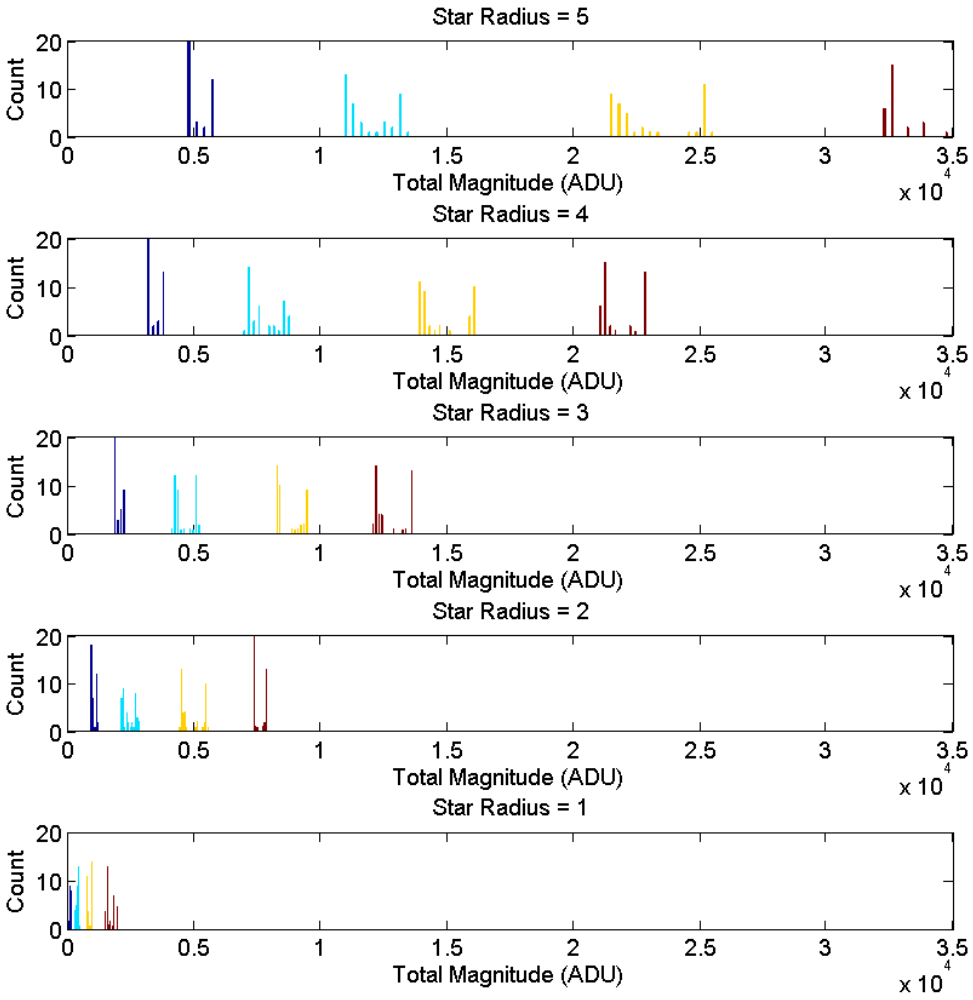

Figure 3.12: Brightness Histograms of each Star Size

From these brightness histograms, 11 star size and contrast ratio combinations were chosen that had no overlapping brightness values as shown in the combined histogram in Figure 3.13.

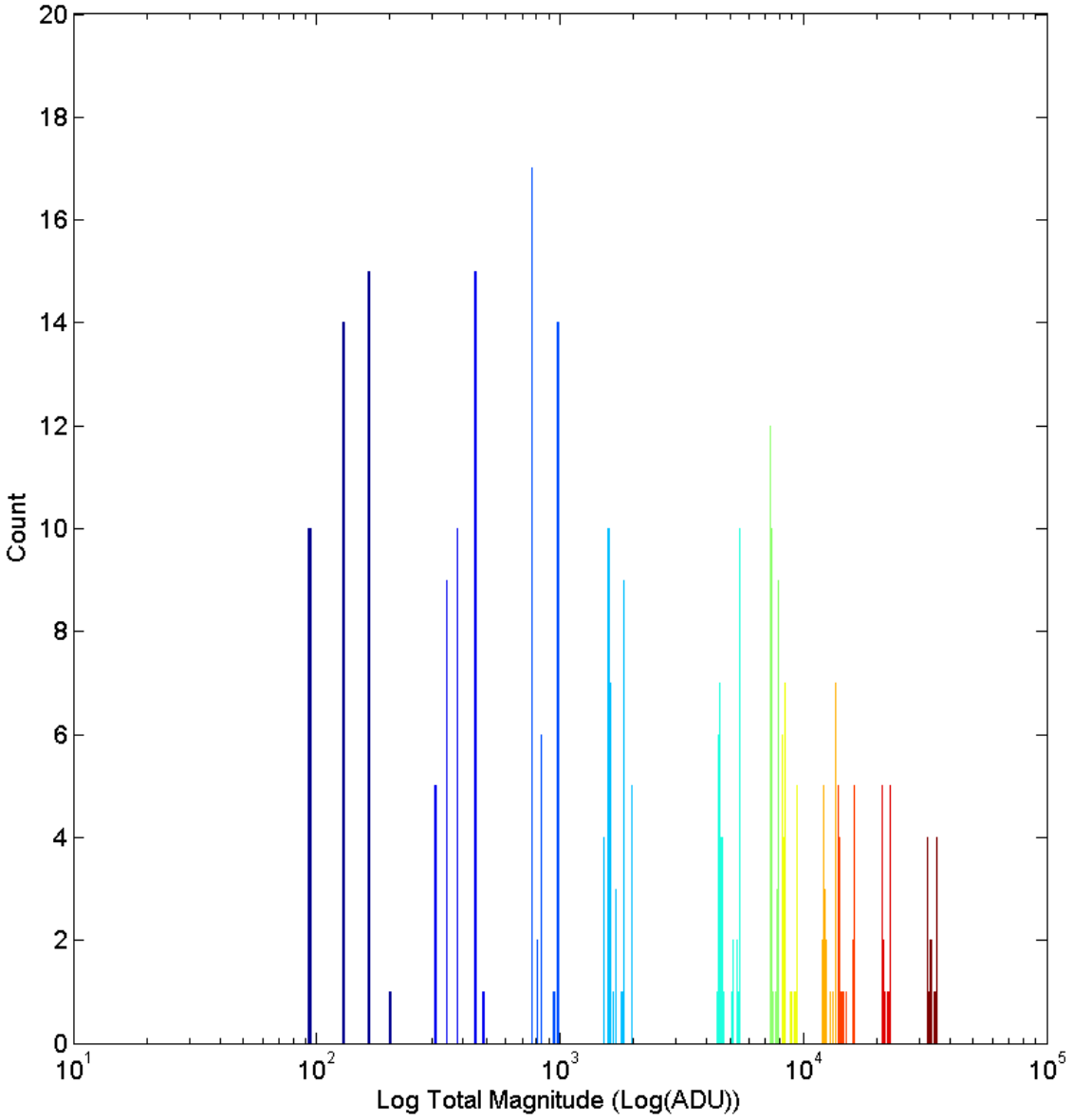

Figure 3.13: Histogram Showing 11 Brightness Bins

Using the 11 brightness values and the 82 angle values, there are a total of 5,412 unique patterns based on

$$P = \theta_U \frac{(BB+1)!}{2 * (BB-1)!} \tag{3.1}$$

where θ_U is the number of unique detectable angles, BB is the number of unique brightness bins, and P is the number of unique star patterns. 5,412 unique patterns is more than enough since there are only 125 panels on the dome. What this analysis shows is that there are plenty of brightness options available so choosing the brightness values (through color, contrast ratio, or size) that yield the lowest centroid variation is the critical factor.

Choosing several colors is a possibility since the specific magnitude is also known for a given contrast ratio. Specific magnitude refers to the average brightness per pixel of a star, which is a function of contrast ratio and color. Figure 3.14 shows the specific magnitude for the different contrast ratios used in the previous analysis. If a different color has a lower centroid variation then it could be used instead of white, or if star size is the most important factor then a combination of colors can be used since they will have different specific magnitudes.

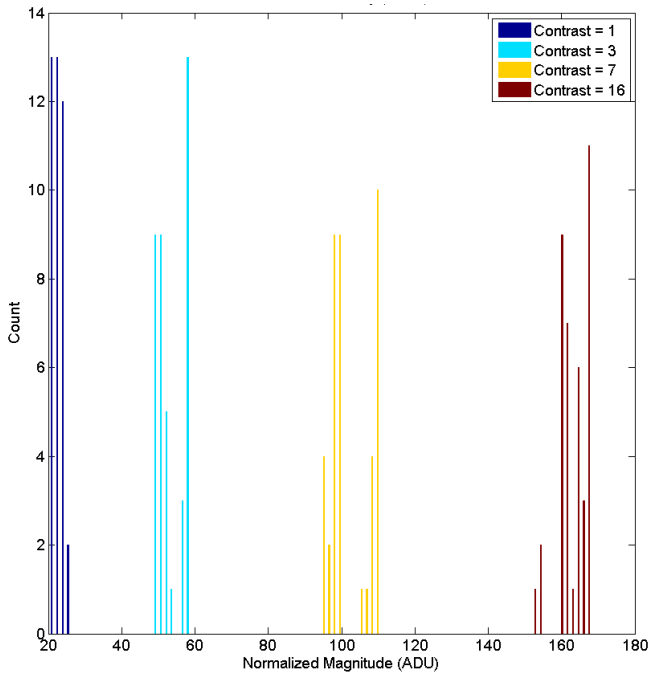

Figure 3.14: Specific Magnitude of White Stars at Various Contrast Ratios

3.2.2.5 Spread of Stars in an Image.

By spreading out the stars across the image, large gains can be made in accuracy for small rotations. Since a small rotation about the Z-axis can appear like a small rotation about the X-axis if the star panel is directly above the optical axis, having more panels in the FOV gives the QUEST algorithm the necessary information to differentiate the two rotations. This effect is referred to as the "cosine effect" in this thesis, and is shown graphically in Figure 3.15.

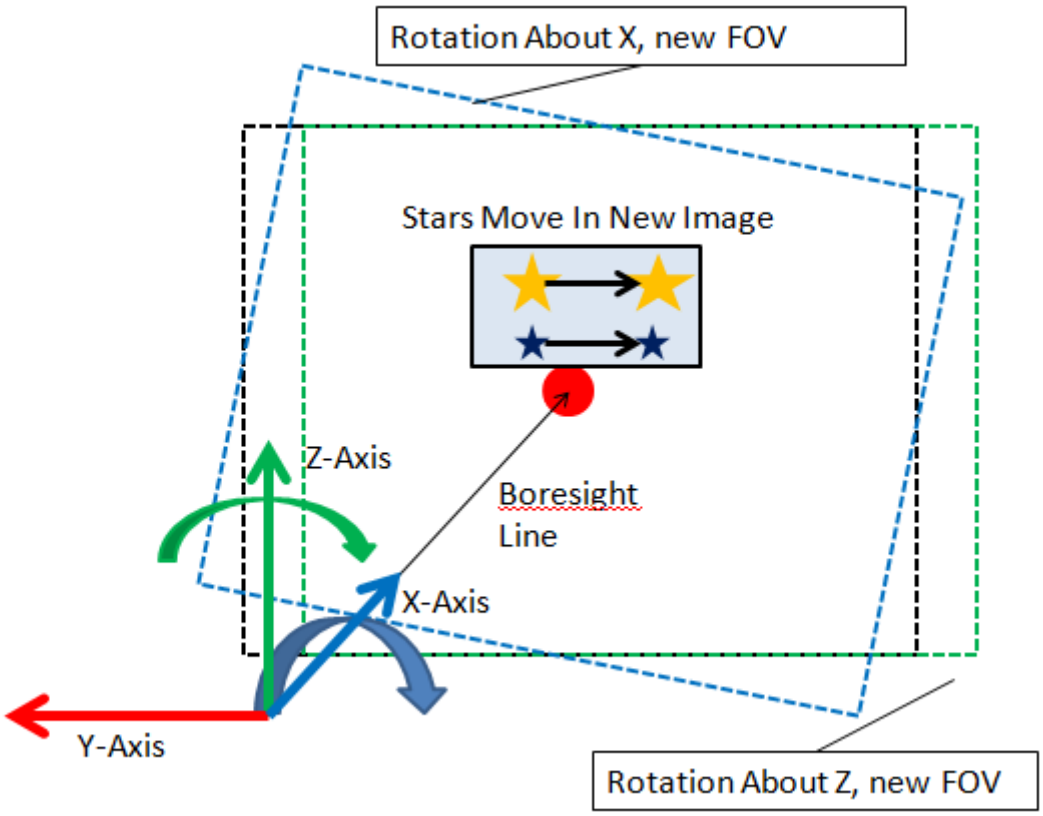

Figure 3.15: Cosine Effect Graphic: The Stars in the Image Do Not Contain Enough Information to Distinguish Small Rotations Between the Z-Axis or X-Axis

The stars and panel shown in this graphic are magnified to more clearly show the movement. This effect is only a real problem when small rotations are attempted ($< 1°$). The stars "movement" is depicted with the arrows and could have been caused by either a rotation about the Z-axis or about X-axis. If more stars are added around the FOV then error for this effect can be mitigated.

Testing this mitigation strategy involved rotating around the Z-axis by 0.01 degrees and recording the rotation solution produced by the camera using a single panel with two stars compared to a set of two panels using three total stars. Figure 3.16 shows the calculated 3-2-1 Euler Angles at the bottom of the image based on only using two stars at the center of the FOV. The rotation was found using the QUEST algorithm to find the quaternion and then converting that quaternion to 3-2-1 Euler Angles. There is about 0.3 degree error about the X-axis since there is not enough information to differentiate the rotations. By just adding one more star near the edge of the FOV, as shown in Figure 3.17, the accuracy increases dramatically as the calculated X-axis rotation changes from -0.31 degrees to -0.016 degrees, which is a 95% accuracy increase.

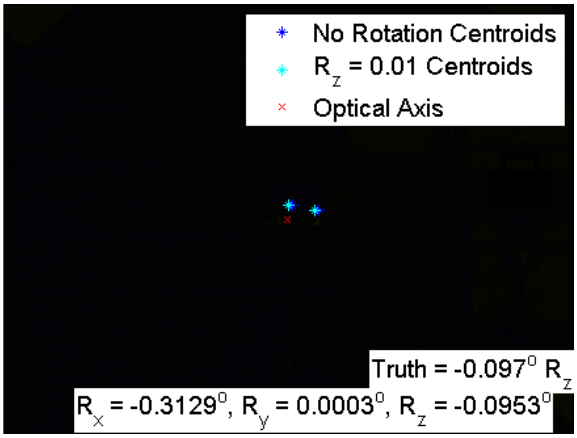

Figure 3.16: Calculated Euler Angles Using Only One Panel Yields Inaccurate Solution From Axis Ambiguity

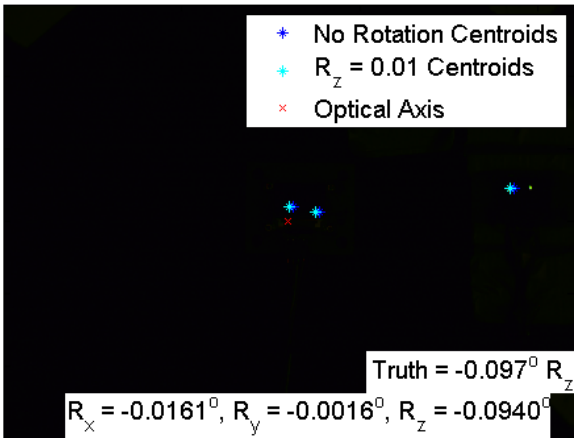

Figure 3.17: Calculated Euler Angles Using Only Two Panels Spread Across the FOV Improves the Axis Ambiguity Problem

Having stars more spread out around the FOV also has a drastic effect on the NEA. For example, in the two figures above NEA decreases by 84% from 0.056 degrees to 0.0092 degrees.

3.2.3 Light Collection Accuracy Effects.

Investigating the different aspects of the light collection process required understanding the optics of the camera lens and the CCD sensor performance. For space-rated star trackers, these aspects of the system can be very expensive since these components need to survive the space environment. For this experimental laboratory setup, the focus was on understanding what could be done to improve accuracy based on what could be controlled and changed easily.

3.2.3.1 Focal Length.

The optics portion of the light collection chain governs how the light coming off the star dome is focused to form an image. Focal length, aperture setting, and lens distortion were investigated, while the focus setting was left at fully focused since the "stars" in this experiment are not true point sources, since even a single focused OLED pixel covers more

than four CCD pixels, so defocussing is not required to spread the light over several pixels for centroiding purposes.

The focal length of the optics and the size of the sensor determines the sensitivity of the system in terms of angular distance per pixel. By multiplying by the number of pixels across the sensor, the total FOV can be obtained. Thus an increasing focal length will decrease the FOV, but increase the angular sensitivity per pixel. The total FOV can be estimated as follows

$$\phi_{FOV} = 2 \arctan\left(\frac{d_{pixel}}{2 \times FocalLength}\right) \tag{3.2}$$

where ϕ_{FOV} is the angular FOV across the dimension of the sensor described by d_{pixel}, which is the length in millimeters of a given sensor dimension. For example, if the width of the FOV was to be calculated then the width dimension of the CCD sensor would be used. Figure 3.18 shows two cropped images taken with two different focal length lens that are the same size in terms of sensor pixels since both images are cropped to 100 x 100 pixels.

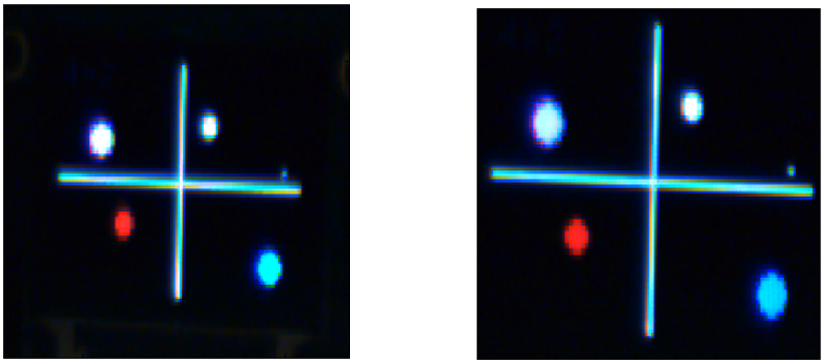

(a) 25mm Focal Length (b) 35mm Focal Length

Figure 3.18: Cropped Images with Same Number of Pixels Comparing Two Different Focal Lengths

Figure 3.18a was taken with a 25mm focal length lens and has a $11.5° \times 15.3°$ FOV, which gives $0.00875°$ angular resolution per pixel. Figure 3.18b was taken with a 35mm focal length lens and has a $8.25° \times 11°$ FOV, which yields $0.00625°$ angular resolution per pixel. The smaller angular resolutions translates to better distance resolution.

3.2.3.2 Aperture.

Cameras are usually specified by their focal length and f/no. This is because exposure time is proportional to the square of the f/no since the flux density at the image plane varies as $(D/f)^2$, where D is the current aperture diameter and f is the focal length. The square root inverse of this flux density is defined as the f/no, or f/D. Some common f/no settings are shown in Figure 2.11. Notice that they increase by a factor of $1/\sqrt{2}$, which corresponds to a decrease in flux density by half.

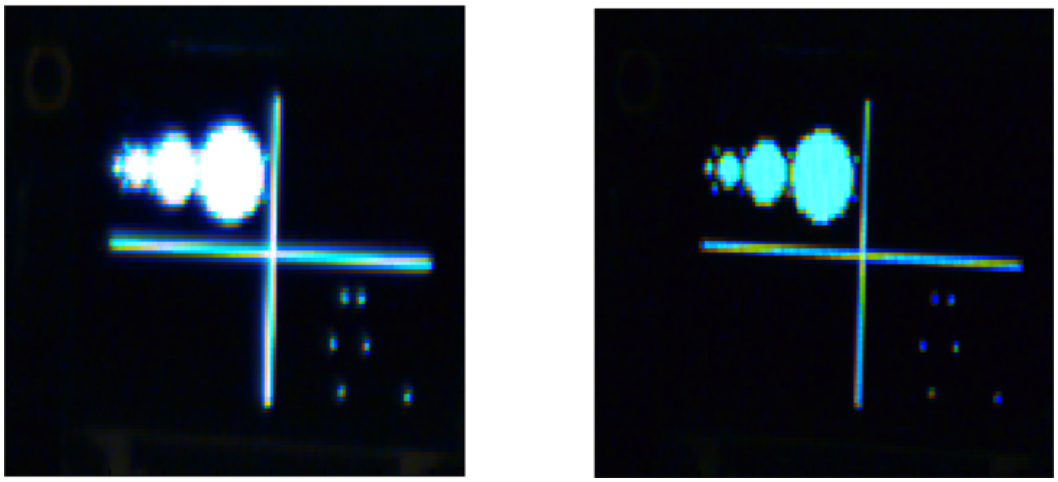

(a) f/1.4 Shows Difficulty Focusing with Small Depth of Field

(b) f/5.6 Shows Reveals Crisper Image, but Less Light Flux

Figure 3.19: Cropped Images Taken with 25mm Focal Length Comparing Two Aperture Settings

Increasing f/no also increases the depth of field of an image, meaning the distance at which things are in focus is increased. The decreased light density and increased sharpness of an image is shown in Figure 3.19. Aperture setting is coupled with many of the star brightness characteristics. Reducing the coupling can be accomplished by having the same specific brightness (brightness per pixel), which can be affected via color selection or contrast ratio. Setting specific star brightness to be the same across an image will help with the aperture setting have more predictable effects across the star dome.

3.2.3.3 Lens Distortion.

This section examines the effects of lens distortion across the FOV with a 25mm lens. Having pin cushion or barrel distortion will cause angles to appear different sizes on the sensor just from coming from different parts of the FOV. If the angle between two stars is still clearly distinct across many portions of the FOV, this implies that lens distortion will have a minimal effect when it comes to star pattern recognition.

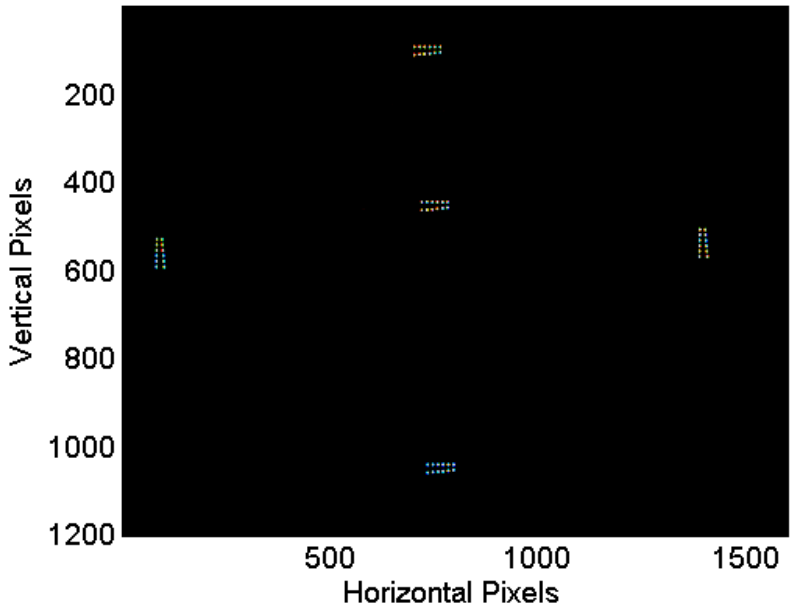

Figure 3.20: Angles Remeasured Across the FOV (5 stacked images)

While there was some distortion and increased variance in the angle measurements, there was still no bin crossover and each angle still had its own unique bin. There was also no noticeable pattern in the distortion (such as angles near the edges of the FOV being consistently larger or smaller), likely meaning there is no dominant distortion characteristic of the lens, it just had general imperfections across the optical plane. The histogram, Figure 3.21 showing all 200 angle measurements (40 samples at five different positions) clearly shows the six angle bins with no overlap.

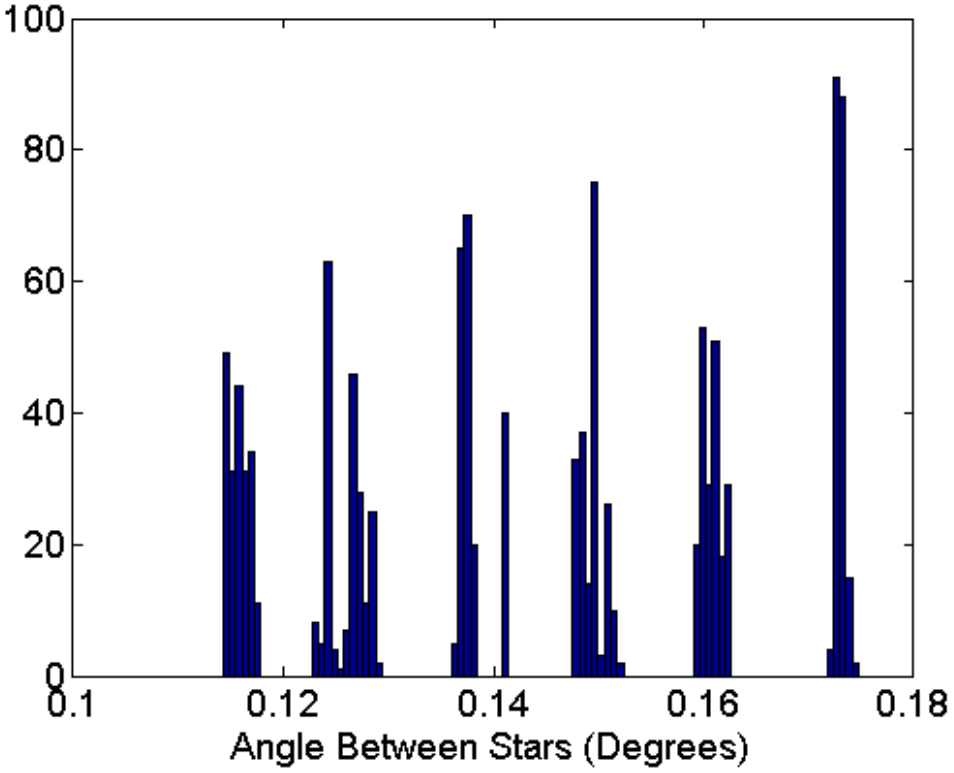

Figure 3.21: Histogram Showing Six Angle Bins

Extrapolating this analysis to include all angle sizes from eight panel pixels (0.096°) to 90 panel pixels (1.04°) allows for 82 possible angle bins. While there is certainly more variance, which can be seen in the growth of the error bars in the linear fit as shown in

Figure 3.22, the means aproach the true mean making the overall fit better and the errors bars are still small enough to permit making a single pixel change a separate angle bin. If the error bars were to shown with a three standard deviation error value, then there would be some overlap between the measurements; however, this is a very minor chance since there was not a single measurement that was close to overlapping and if that does occur in the algorithm then there will be other stars to verify the correct star has been identified.

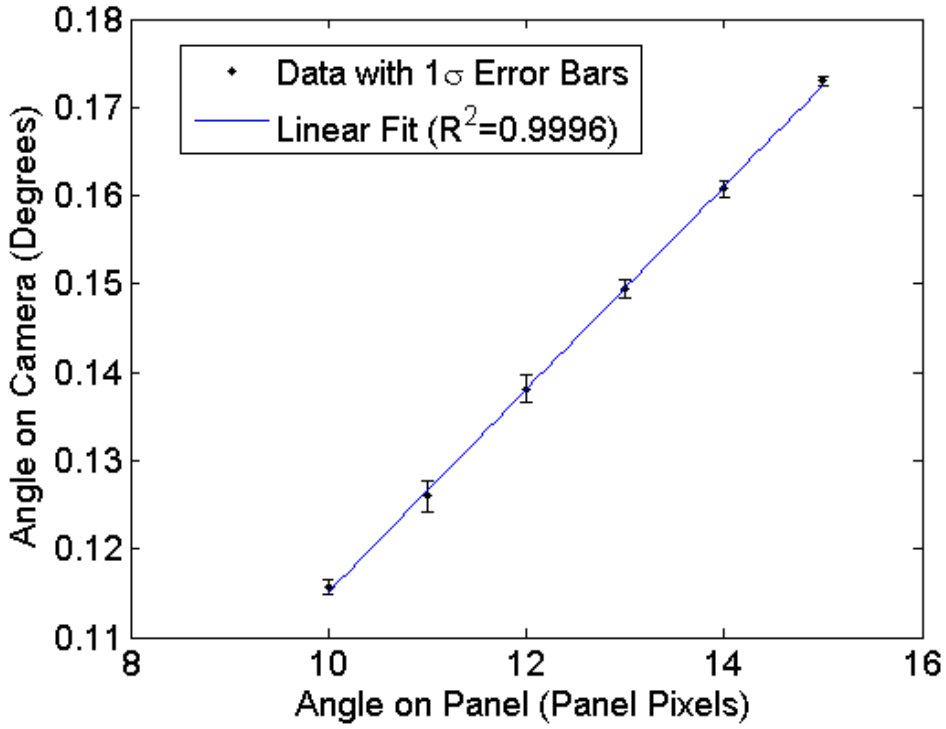

Figure 3.22: Fit of Pixel Width on OLED Panel to Measured Angle

3.2.3.4 Camera Calibration.

The camera being used, like most second generation star trackers is a Couple Charged Device (CCD). These detect light by converting photons into electrons and storing those electrons in wells (each pixel). The current tests have been done with a color Lumenera 205c CCD.

Thermal frames were not taken since integration time could not be set to zero with the camera, but dark frames provide a good baseline of thermal electron noise and with the SNR in terms of photon flux from the panel this should not be a major concern.

Dark frames were created to examine readout noise and detect any hot pixels. Taking one dark frame results in many "warm" pixels that come about as a result of thermal background noise and may not necessarily be indicative of hot pixels are systematically reading out higher than other pixels. A single dark frame that has been scaled up by a factor of three is shown in Figure 3.23.

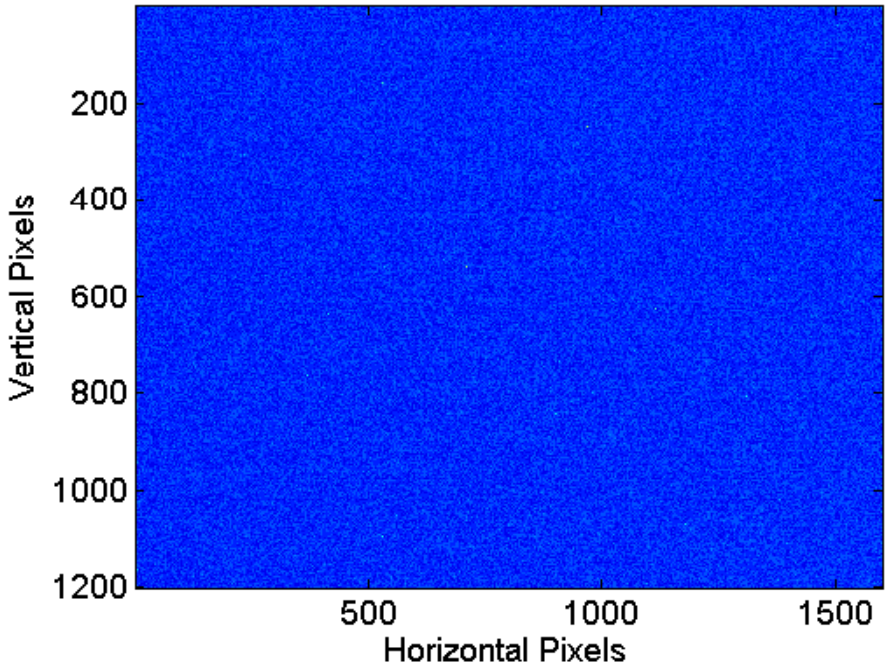

Figure 3.23: Single Dark Frame

In order to reduce random thermal noise, 40 dark frames were taken and averaged together in a master dark frame that reveals some of the hot pixels in the CCD (a few have been circled in Figure 3.24). The average pixel value in the master dark frame is 3.03 out of 255, while the hot pixels can have values up to 15. These hot pixels can cause problems

if the magnitude of the stars being used is near the hot pixel value because the centroid algorithm is based off the maximum intensity in the image and it may confuse a hot pixel for a star extension. However, the master dark frame can be subtracted from every image to account for pixel variations and solve this problem. Ideally dark frames should be taken every time the camera is used and a new master dark frame created for every viewing session, but as along as the brightness of the stars being used in testing is at least twice the maximum pixel value then using the same base dark frames should not cause any issues.

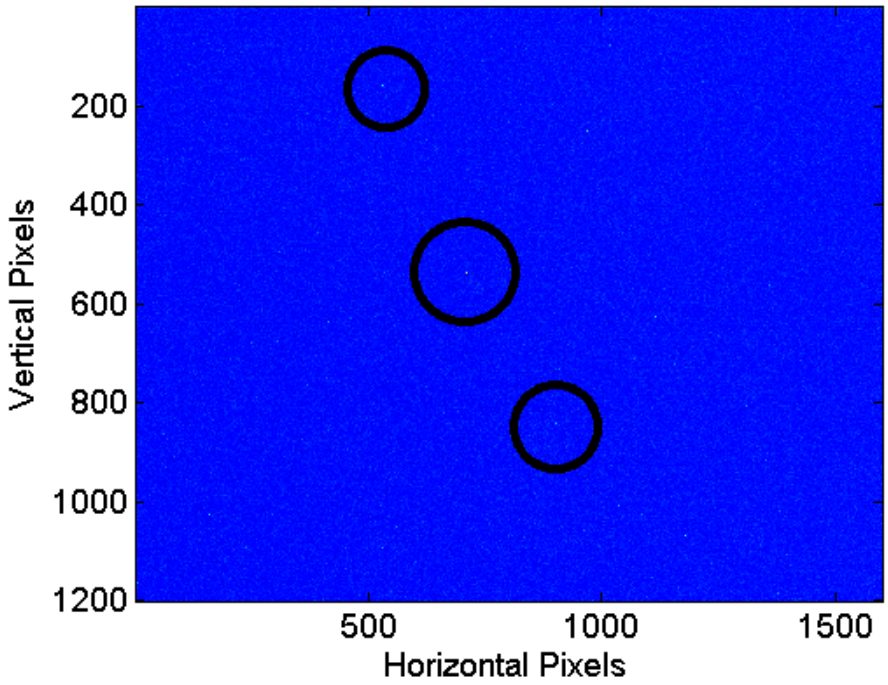

Figure 3.24: Master Dark Frame Taken by Averaging 40 Dark Frames with a few Hot Pixels Circled

The last type of calibration frame that will be used are flat frames. These frames are used to take into account CCD sensitivity variations and vignetting issues of the whole optical system. Flat frames get their name because they record the response of the optics and CCD to a uniform (flat) field of light. These frames can be made by putting a diffuse

surface infront of the camera and shining a light on it so that it is approximately uniformly illuminated. Then frames are taken and can be combined to create a master flat frame in a similar way to the master dark frame was created.

3.2.3.5 Color Interpolation.

The color CCD creates color images by interpolating between different colored pixels on the 1200x1600 grid. The pixel color sensitivity pattern is similar to that shown in Figure 3.25.

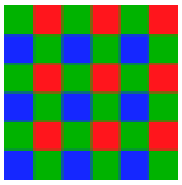

Figure 3.25: CCD Pixels Color Mosaic Example

This interpolation pattern has an effect on star centroid accuracy since it determines how much light intensity is recorded by the CCD. Even though the star may be outputting light in a circular pattern, since that light is not evenly recorded by the different color sensitive pixels, it will not be evenly spread out in a circle. This is shown well by zooming in close on a star, such as in Figure 3.26.

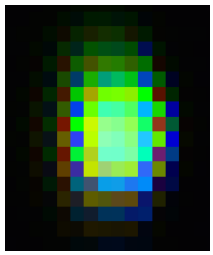

Figure 3.26: “White Star”: CCD Pixels are Interpolated to Give RGB Image (notice that edges of the star do not have neighbors to interpolate and stay single colored)

Notice that the green-red-blue-green (GRBG) 2x2 matrix is visible near the edges of the star were there is not enough light on the dark side of the star to properly interpolate the color. In order to reduce problems associated with using a color sensor, a grayscale CCD was ordered and was utilized for the final system tests. The tests done to compare the grayscale CCD with the color camera are described in Section 4.1.1.

3.2.4 Algorithmic Accuracy Effects.

Another area of the system that was investigated to see how accuracy can be improved was the software used to find centroids from the collected light, construct vectors from those centroids, and then calculate the rotation solution. The different aspects of the centroiding algorithm were investigated to see how changing the intensity threshold of what is considered a star in the image affected the centroid uncertainty.

Changing the max star threshold value for the centroiding algorithm has a clear effect on centroid deviation in a given image, as shown in Figure 3.27.

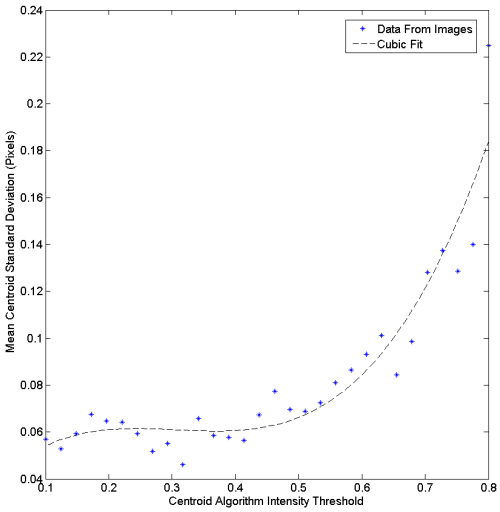

Figure 3.27: The Effect of Centroid Algorithm Percent Intensity Parameter on Average Star Centroid Uncertainty

This effect is caused by excluding certain pixels from the algorithm if they are below the max intensity found in the image. As the percent intensity of this max intensity is increased, then fewer pixels will be considered part of the star since they are lower in intensity than the threshold value. Figure 3.28 shows logical star positions, meaning either red for yes there is a star there or blue for no star, for four different threshold values. As the threshold is increased, star area is decreased so any small deviation from true shape causes a larger change in the centroid. However, having too low of a threshold causes the algorithm to include extraneous pixels near the star that also distort the shape.

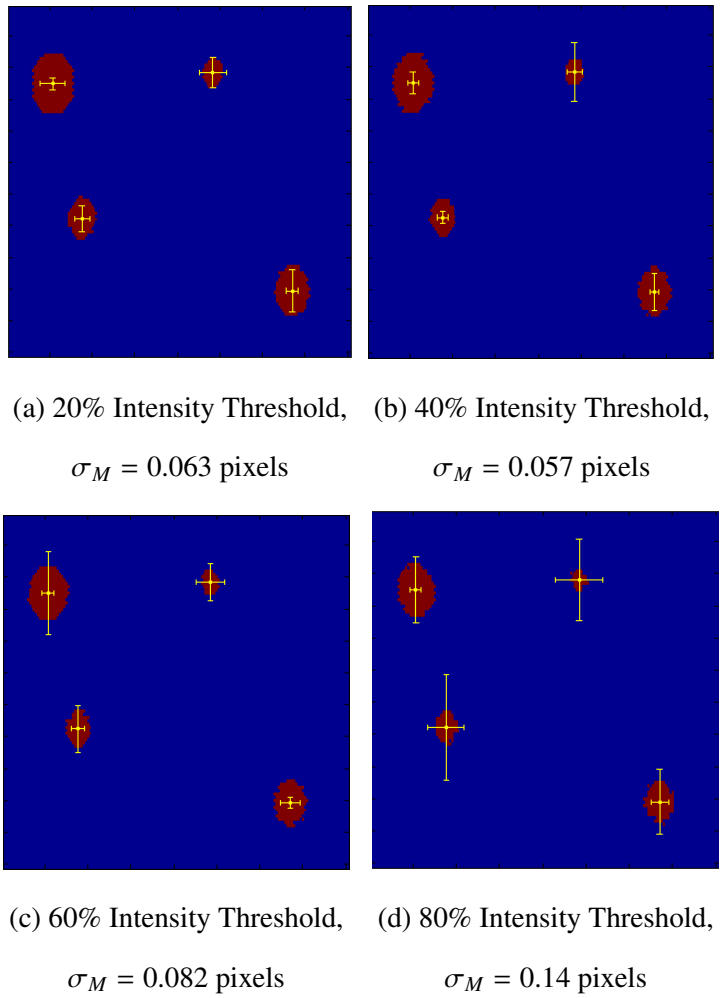

(a) 20% Intensity Threshold, σ_M = 0.063 pixels

(b) 40% Intensity Threshold, σ_M = 0.057 pixels

(c) 60% Intensity Threshold, σ_M = 0.082 pixels

(d) 80% Intensity Threshold, σ_M = 0.14 pixels

Figure 3.28: Logical Star Areas after Threshold (error bars depict 100 σ deviation)

As demonstrated in Figure 3.28, the brightness of a star can be controlled in terms of centroid deviation by changing the centroiding algorithm intensity threshold. Note that in Figure 3.28 the error bars represent 100 times the standard deviation for a given star. This was done to compare relative uncertainties since they can be easily seen in the image. Realizing this allows the user to focus on controlling the software on the camera side instead of trying to optimize the light output of the OLED panels.

3.3 Fully Populating the Dome

This section will explain how the dome was fully covered with panels to create a full starfield, meaning two panels are always in the FOV, and all the different factors that affect the layout of that starfield. First, the mounting solution of the panels is discussed because we need to mount flat panels to a curved dome surface. This is followed by a discussion on how the panel mount allows more cataloging and calibration options because the location of each panel must be accurately determined to generate a star catalog. Next, the parameters, such as FOV and panel density, important to deciding how the panels will be placed around the dome are expounded upon. Last, a brief overview of how the panels are currently wired for power and reprogramming is presented.

3.3.1 OLED Panel and Plastic Backing.

While work was being done on setting up the dome on the optics bench, the best method to represent the stars was decided. Based on the OLED panels large viewing angle, many brightness options, many star placement options (96x64 pixels), low power consumption, and relative ease of programming the 4D Systems 0.96 inch diagonal OLED module was chosen. Their small size prevents errors from placing non-spherical objects on the curved dome surface. These OLED panels would need to be mounted to the dome in a way that is cheap, fast, and reversible in order to minimize man hours needed to create the dome and allow panels to be swapped out in case of a panel failure.

In order to mount the panels to the dome, a 3D printed plastic panel backing was created, shown in Figure 3.29 and Figure 3.30. This panel backing offers several advantages over just placing the panels directly onto the dome:

- Holes slightly smaller than the diameter of the FaroArm Edge tip allow a plane to be fit consistently that is parallel to the screen surface.
- The backside of the panel can be curved to approximately match the nominal curvature of the dome which provides a better flush fit
- Raised standoffs allow the panel to be screwed into the mount while permitting cables from other panels to run underneath.

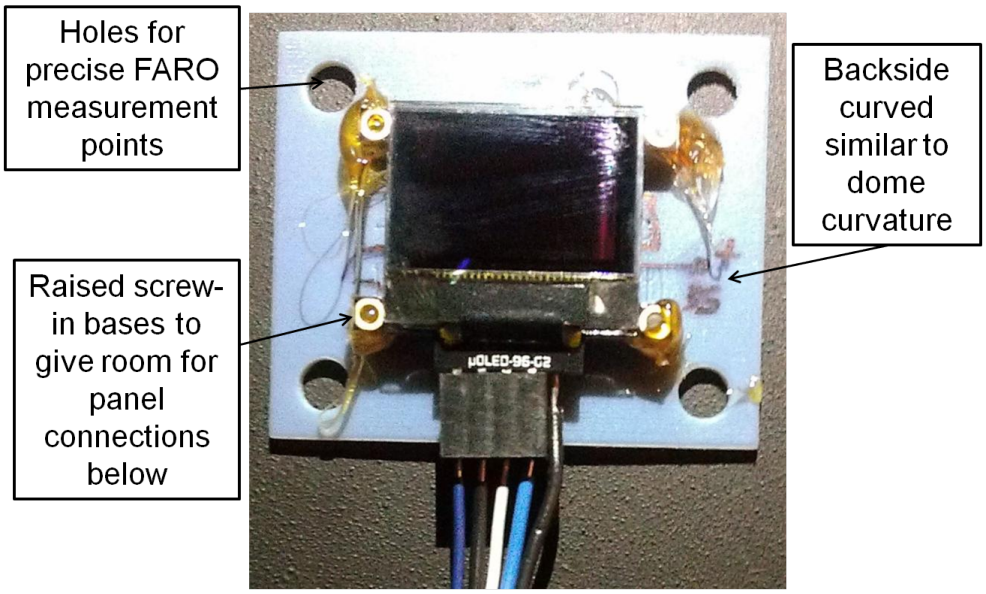

Figure 3.29: OLED Panel Affixed to Dome

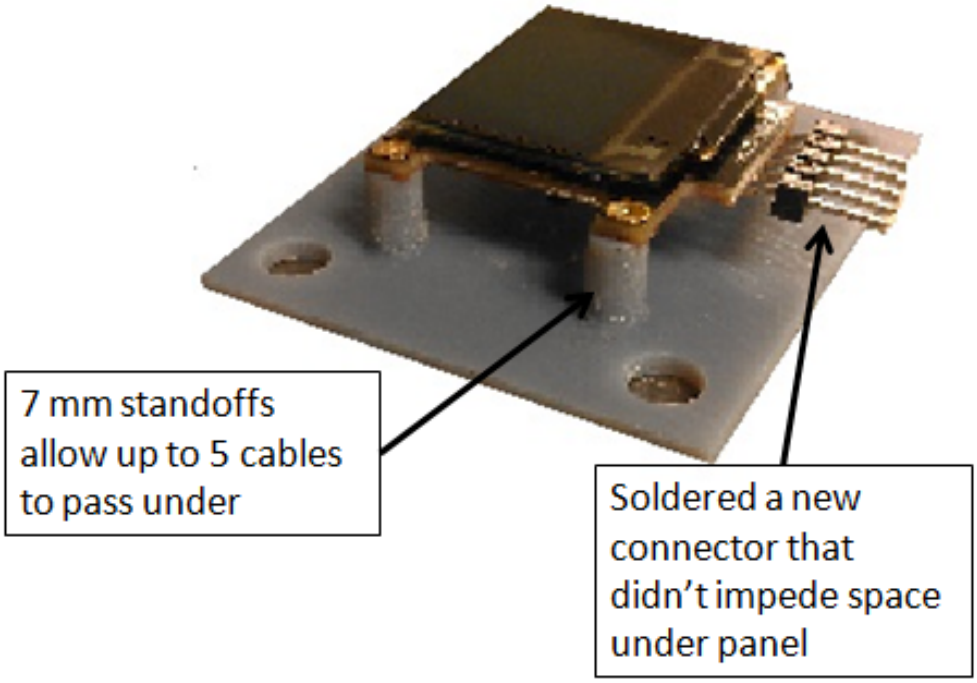

Figure 3.30: OLED Panel and Mount Sideview

The plastic backings are hot glued to the dome which resulted in a secure, but not permanent fit. The final design also included a standoff height of 7 mm, which was important for allowing cabling from other panels to pass under a given panel. This precluded the need to drill holes into the dome to connect to each panel and also kept the wires organized. Another essential aspect was that when the panels were placed they could be done so approximately with the main concern for the overall panel placement pattern and not very precise positioning restrictions because there locations were later measured using the FaroArm Edge.

3.3.2 Deciding Upon the Population Scheme.

One of the main goals of this research effort is to allow SimSat to determine its attitude with an external reference over its entire range of motion, which requires a fully populated star dome so that the star tracker can always have enough panels in the FOV to accurately

come to a rotation solution. The largest cost in the population of the star dome is by far the OLED panels themselves, which cost around $40 each, so minimizing the number of panels is desirable as long as accuracy goals can be reached.

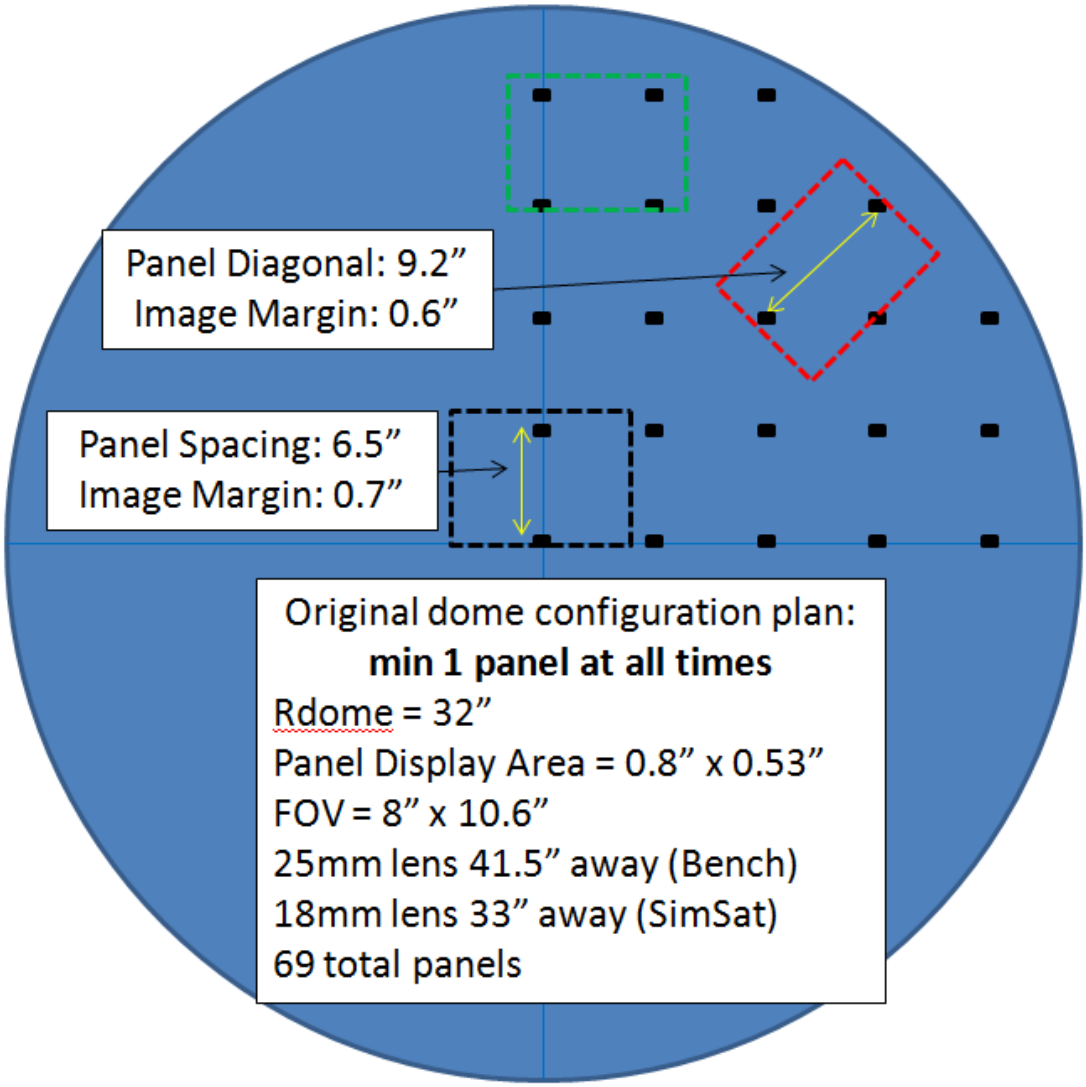

Figure 3.31: Initial Panel Population Scheme Based on 1 Panel always in FOV

Initially, the full population of the dome was based upon minimizing the number of panels under the constraint that at least one was always visible to the camera, which was

later increased to two panels. Based on the constraint of one panel always being in view, the pattern shown in Figure 3.31 was developed. Based off the inch-wise FOV on the dome (which is a function of camera focal length and distance from the dome) minimum side length of 8 inches, the panel spacing was worked out to be 6.5 inches. This value gives about 0.6 inches of image margin, which means that in the worst case (red FOV box in Figure 3.31) another panel should appear in the image when the original panel is 0.6 inches from being out of the image. This guarantees at least one full panel will be in the FOV. However, as the thesis effort evolved, the realization came that one panel in the FOV would not result in the desired system accuracy.

The cause of the drop in accuracy with just one panel in the FOV is explained in detail in Section 3.2.2.5, but it has to do with the cosine effect of not being able to discern a rotation about either different axes based upon one set of closely placed data (one panel with several stars). In order to remedy this issue in the panel population design, the requirement was changed to always have at least two panels in the FOV. With the original lens focal length of 25mm, this would almost triple the cost. So in order to not have too severe of an increase from panel number increase, a varifocal lens was ordered that can have a minimum focal length of 12 mm, which allows a larger FOV on the dome, which lead to a cost increase of 1.8 times, instead of almost 3 times. Figure 3.32 shows the final population design. This design will have anywhere from two to six panels in the FOV.

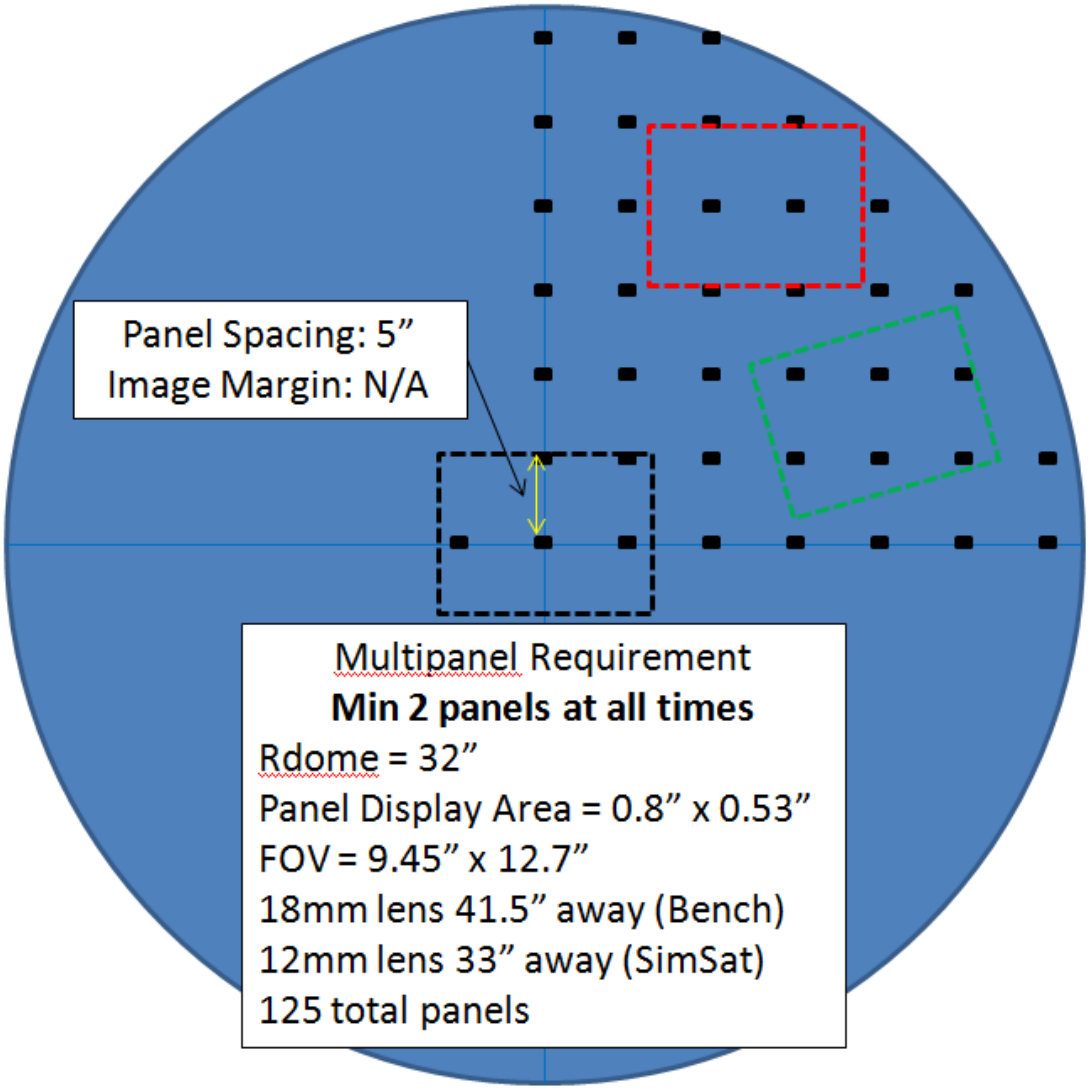

Figure 3.32: Final Panel Population Scheme Requiring at least 2 Panels always in camera FOV

Both of the panel population schemes, minimum of one or two panels in the FOV, involved panels that were aligned horizontally and vertically and not in a spherical pattern. When this effort was first started, circular panel arrangements were initially considered but it turned out that horizontally aligned panel rows actually required less total panels than the method of circular rings and spacing those rings out based on minimum distance required.

The linear arrangement also facilitates neater cable management since the connectors from other panels can pass through the space in-between each panel and its plastic backing. In order to minimize the number of panels that a wire would have to pass under to reach the backside of the dome, they were oriented different directions, as shown in Figure 3.33. In this figure, the different color panels correspond to the orientation of the wiring towards the backside of the dome. Note that in Figure 3.33, the panels have been enlarged to show context and are not to scale.

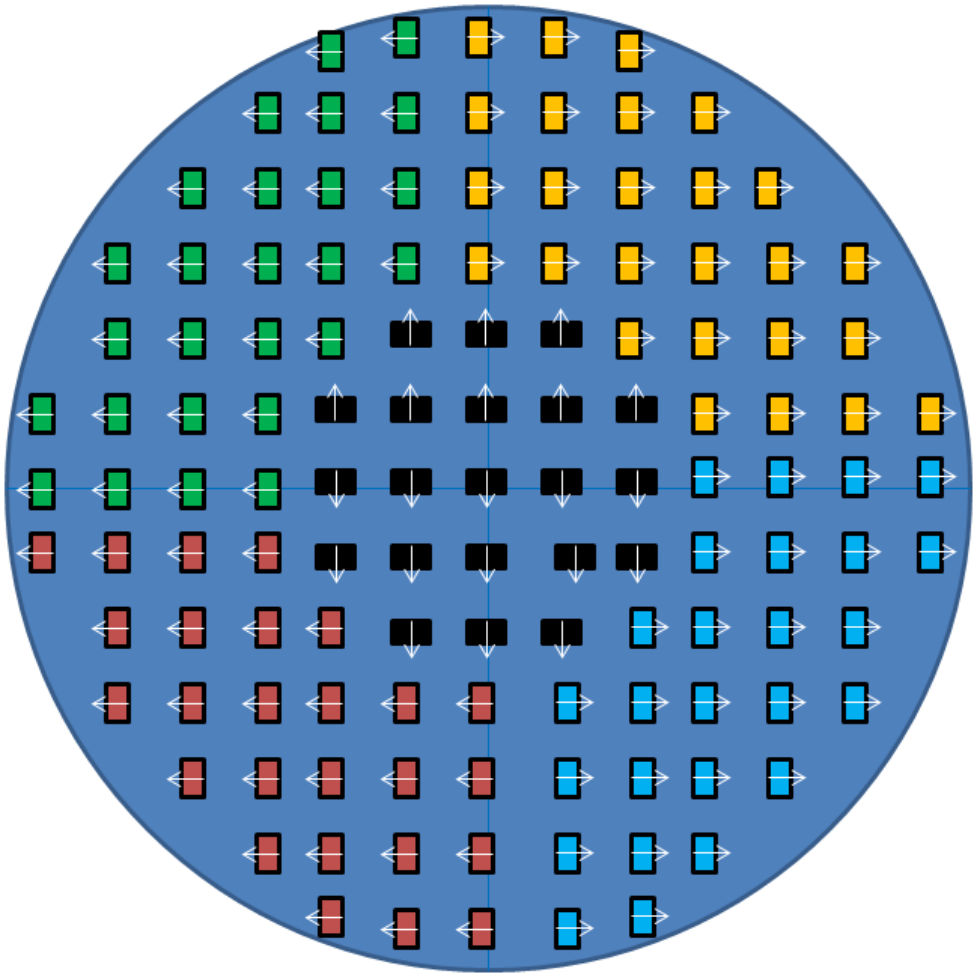

Figure 3.33: Panel Orientation on Dome for Reducing Maximum Cabling Under a Single Panel

In this scheme, the maximum number of wiring sets going under one panel is five. This set up is also how the different regions of the dome are powered. Each different color is supplied by a 5V power supply. Each of the four outer quadrants has 26 panels, while the center quadrant (black color) has 21 panels. The reasoning behind this power scheme is that there may be times when only the center region will be tested, so power can be conserved by isolating that separate from the rest of the dome. since each panel draws around 20 mA with the latest star patterns, the total power draw is 12.5 Watts for the whole dome, but only 2.1 Watts for the center region.

Once the panel spacing and orientation was decided upon, the population of the dome could physically begin. While placement did not have to be exact, it has to be close to the nominal spacing of 5 inches between panels and lines of panels needed to stay parallel. In order to get the first panel set on the dome, two strings were set under the mounting screws of the dome, which crossed at the midpoint, as shown in Figure 3.34.

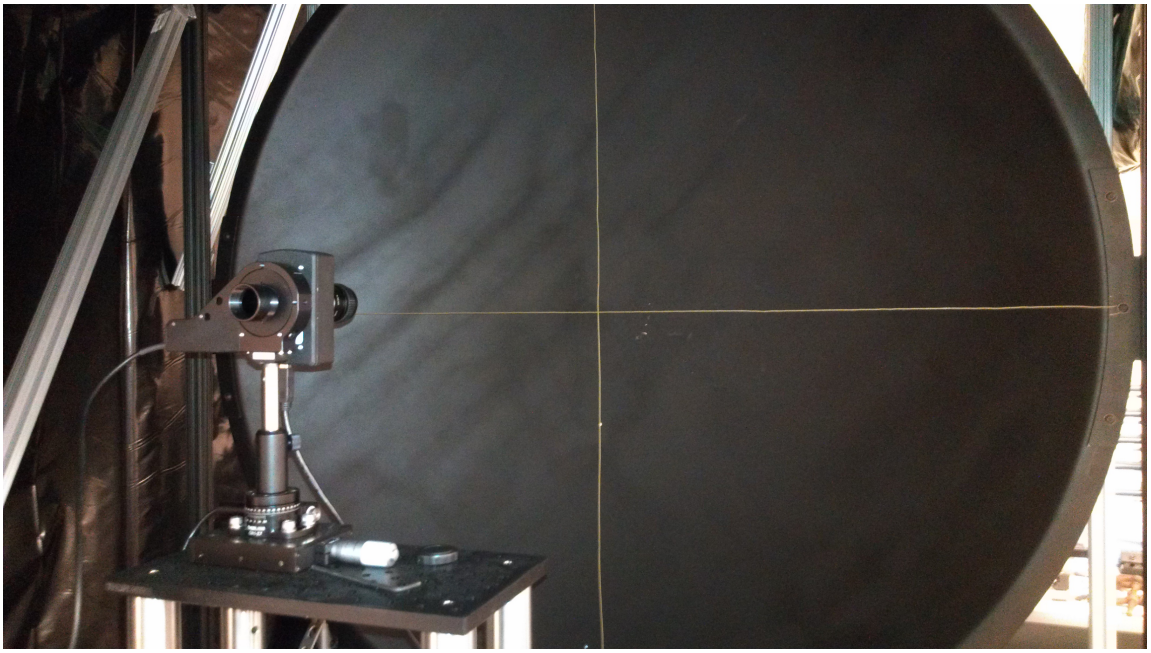

Figure 3.34: Strings Fixed to Sides of Dome to Allow Easy Centering

Following the intersection of the lines to the dome allowed the first panel to be placed at the center with reasonable confidence (verified within a quarter of an inch with a measuring table). This center point is important mainly for equal spacing of the panels across the dome, so high precision is not required. After the center panel was placed, the strings were then ran under it so that they would be closer to the dome. This is shown in Figure 3.35. This allowed a visual check to make sure the first row and column of panels was being placed in a parallel fashion.

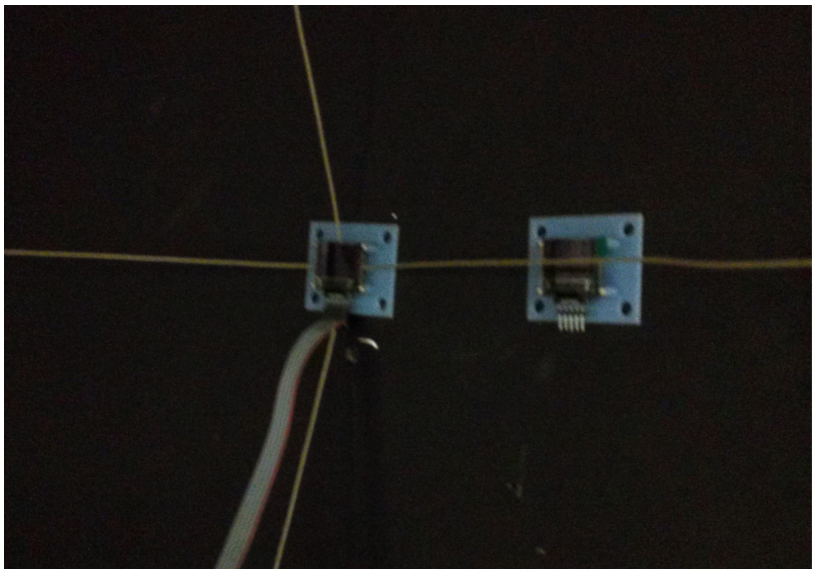

Figure 3.35: Strings Passed Under Center Panel to Allow Line Visualization

Placing panels utilized a measuring tape from the far end of a panel. Five inches was measured and lightly scored on the dome to indicate where that same edge should be placed for the next panel. This was done in two places to ensure a straight line was created. Eventually the entire dome was populated, as shown in Figure 3.36.

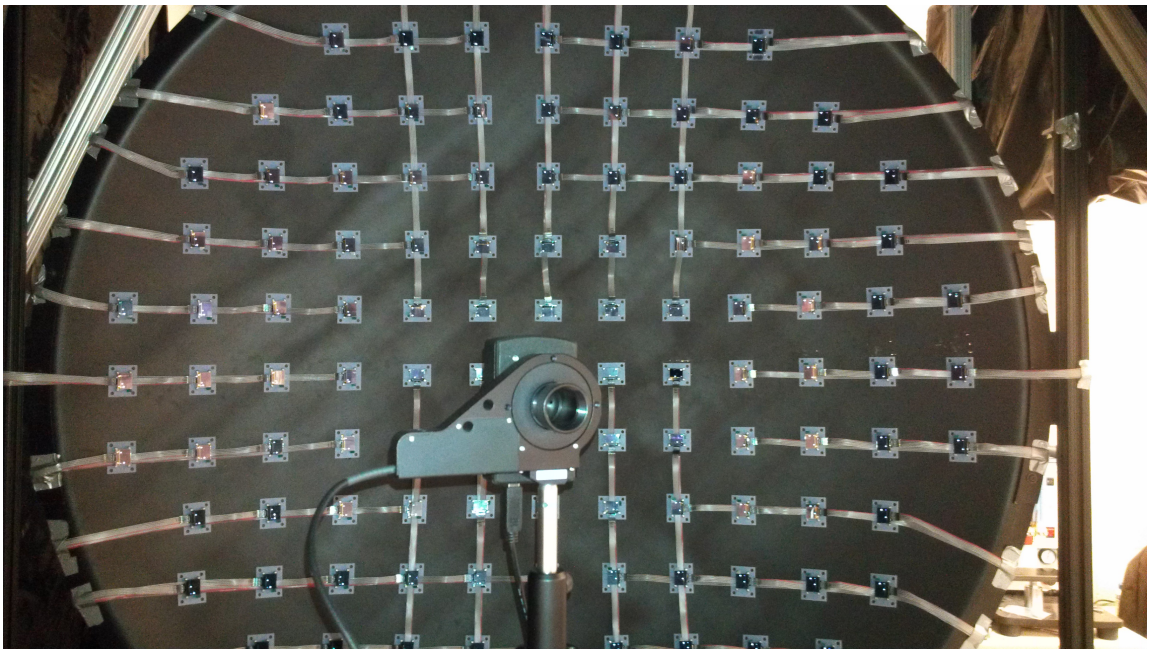

Figure 3.36: Fully Populated and Wired Dome

3.3.3 Panel Programming Network.

Now that the process of creating the dome has been explained, the current wiring and programming access state of the dome will be elaborated upon. Automatically reprogramming all the panels from one fixed computer is the ideal goal for this set up; however, due to parts and manpower limitations the panels are currently connected to breadboards at the end of every row. All five USB connections (+5V, TX, RX, RES, GND) are carried to the breadboards, but only +5V and GND were connected for all except the middle panel. A sideview of the dome shown in Figure 3.37 shows how the wires wrap around to connect to these breadboards.

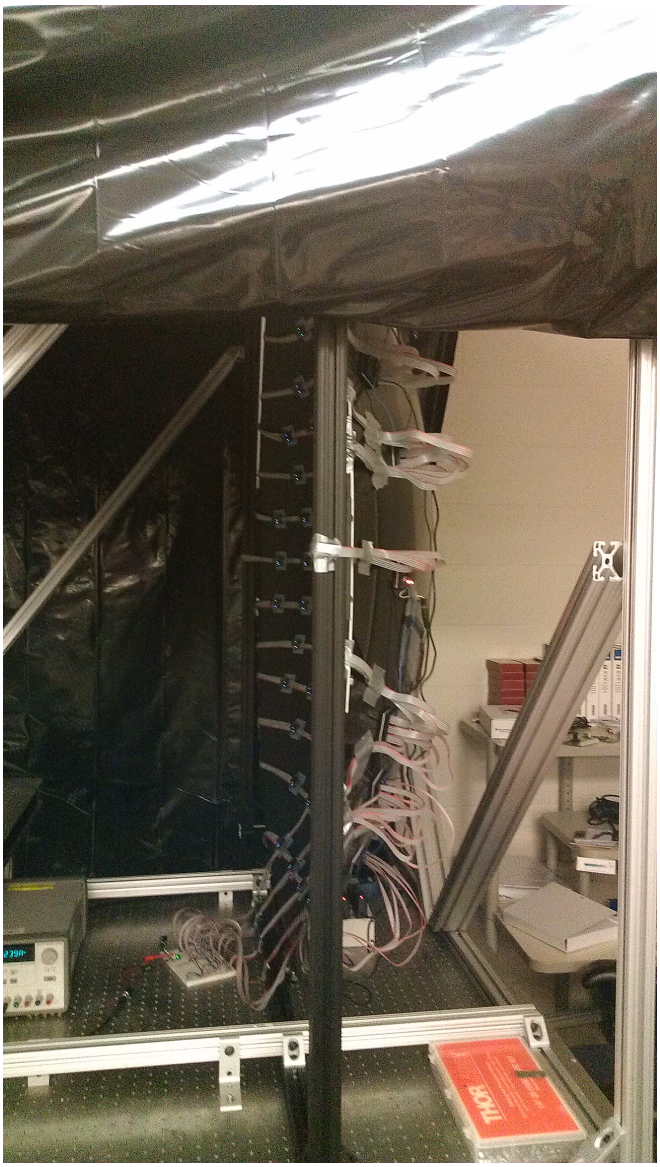

Figure 3.37: Powering the Panels via Breadboards

Currently the center panel can be easily reprogrammed since it is connected to the SimSat ground station computer. The rest of the panels would have to be connected to manually once at a time to reprogram, which is why the current catalog method was chosen to be as robust as possible, discussed in Section 3.4.1. Having one panel easily reprogrammable does allow different star recognition algorithms to be tested and other

simple testing to be done quickly. In order to ensure that the programs loaded into the other OLED panels represented a robust design (every panel had a unique starfield), a different approach was taken to cataloging which is the topic of the next section.

3.4 Catalog Development

This section will detail the approach used to develop a robust star catalog because it is one of the most important parts of the system since the catalog is what every measured vector will be compared to in order to solve for the current attitude of SimSat in terms of quaternions. First, the reasoning behind developing a catalog based off three stars per panel will be explained and the basic relations that allow each panel to be identified with extreme confidence will be revealed. Then, the methods for generating this catalog will be investigated. The first method covered will be utilizing the FaroArm Edge to measure coordinates of each panel in 3D space which can then fix the star vectors relative to the center of rotation. The other approach to cataloging is utilizing the camera, but that requires knowing the camera's orientation relative to the inertial frame.

3.4.1 Planar Triangle Catalog.

Starting from the simple interstar angle catalog capabilities discussed in Section 3.2.3.3 it was clear that the system could discern a change in one OLED pixel quite confidently. A feasible pattern design going forward could be just utilizing two stars per panel and having a few different brightness levels. However, adding another star per panel would allow different triangle based catalog methods to be tested and should also increase the solution accuracy since the star density would be higher. By utilizing a planar triangle based approach to identifying star patterns, a relatively simple star field can be generated with well defined relations.

Initially, the approach described in Section 2.4.3 was applied, which involves calculating the area and polar moment of each triangle. However, since each panel could be programmed to any pattern that the user desires, a simpler approach was developed that

utilizes well defined relations between each OLED pixel and star magnitude measurements. By having three clearly distinct stars (different sizes) on one panel, the side lengths of the star triangle can be calculated and used directly for cataloging as long as they are set sufficiently apart.

Three stars, one in each corner except the upper left, were programmed to display on the OLED panel to determine the maximum spacing difference of each unique triangle. These three stars were different sizes so they could be identified separately by magnitude on a per panel basis. See Figure 3.38 for reference during this explanation. The bottom stars are separated by 83 *x* pixels for zero overlap, while the right stars are separated by 48 *y* pixels for zero overlap. In order to have uniqueness for each panel, we need at least 125 unique triangles.

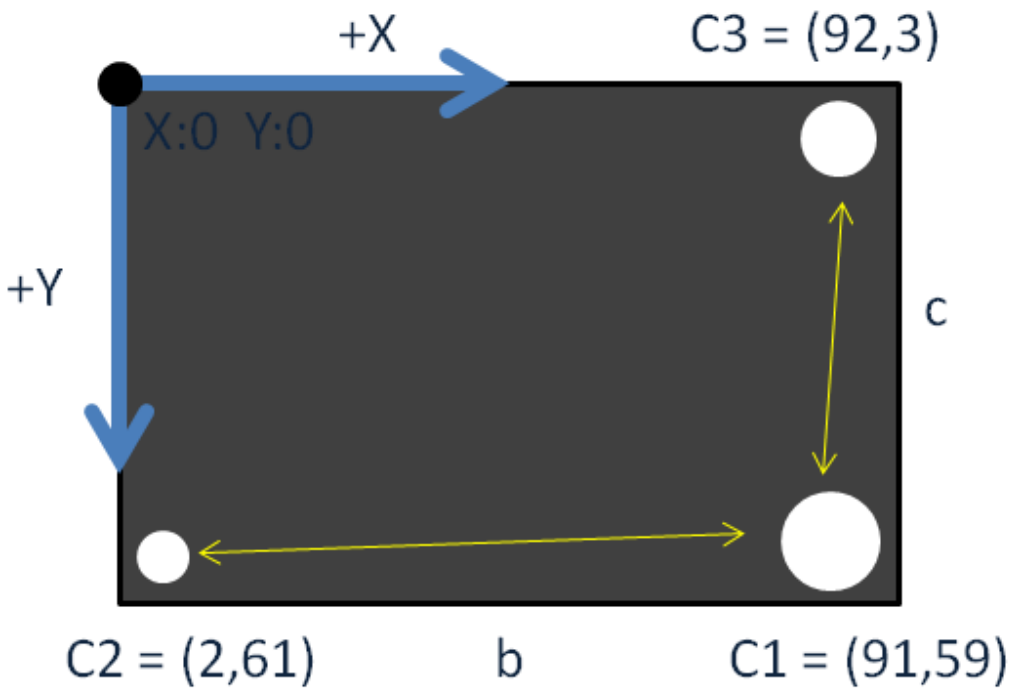

Figure 3.38: x0y0 Triangle Example with Star Centroids in OLED Pixel Units

After testing different increment sizes, the best solution found was 14 x-increments (0 to 13) and 9 y-increments (0 to 9) which results in 126 unique triangles. Each "increment" moves the respective star by 5 pixels closer to the bottom right star. By moving only two stars in one direction each, the side lengths can be directly correlated to a panel number, which is an x-increment and y-increment of each respective star. For example, a panel number of $x1y3$ means the x star has moved 1 increment and y star has moved 3 increments.

The star with centroid c1 never moves in any of the panels and is always radius 4. The star with centroid c2 (only for $x0y0$) moves closer to star c1 as x-number increases. This star also always has a fixed radius of 2 pixels for every panel. This decreases the length of b as follows

$$b_{OLED} = \sqrt{(89 - x * dx))^2 + 2^2} \tag{3.3}$$

where x is the x-number of the panel and dx is the pixel spacing between x-numbers, which is currently five. Similarly, star currently at c3 moves closer to c1 as y number increases, which decreases side c. Length c can be found through a similar equation

$$c_{OLED} = \sqrt{1 + (56 - y * dy)^2} \tag{3.4}$$

where y is the y-number of the panel and dy is the pixel spacing between y-numbers, which is currently five. Both b and c can be converted into their expected CCD pixel values by multiplying by the relation found during the size calibration detailed in Section 3.5.1. Another advantage of this method is that every panel can be set to the same contrast ratio. This allows the optics and image processing algorithms to be optimized exactly for that specific brightness level since it will be on every panel.

In order to ensure that these values would be easily distinguishable over all 126 different panel patterns, the $x0y0$ pattern was displayed and imaged 40 times. The standard deviation was calculated from those 40 trials and then multiplied by 10 to get an extreme

worst case noise value. The OLED pixel values were calculated over all possible patterns from $x0y0$ to $x13y8$, then converted to CCD pixels and the worst case noise factor was multiplied by a random normal distribution and added to the nominal CCD pixel value. The resulting histogram is shown in Figure 3.39.

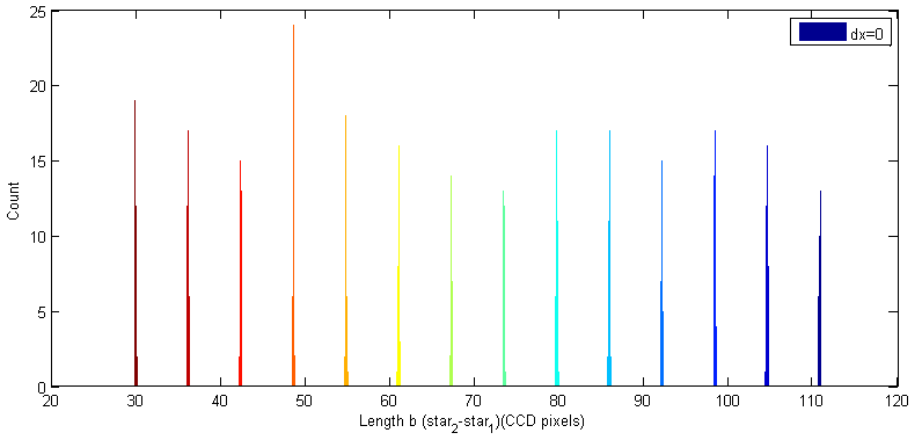

(a) Length B Extrapolated with 10σ Noise Added

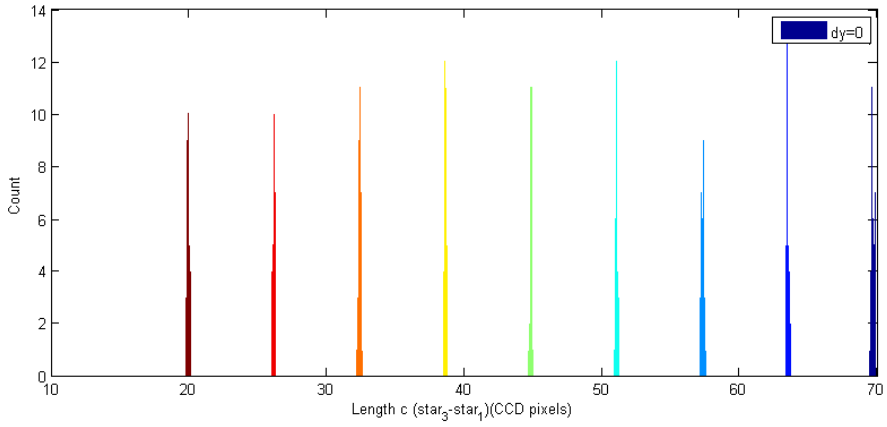

(b) Length C Extrapolated with 10σ Noise Addedd

Figure 3.39: Lengths B and C of All Possible Triangles Showing High Robustness

There is zero overlap even with the noise amplification, which leaves plenty of margin for the small errors that will arise from distance changes over the surface of the dome.

Being able to identify panels over the entire dome allows the non-spherical attribute of the dome to be accounted for via cataloging if the distance to each panel can be properly recorded. Recording that distance is one main advantage of cataloging utilizing the FaroArm Edge, which is discussed in the next section.

3.4.2 Inertial Vector Generation via Coordinate Measuring Machine.

This section will go in depth on the process required to generate a star catalog using the FaroArm Edge CMM and discuss some of the advantages and disadvantages of this method. Utilizing an external measurement system such as the FaroArm to record the position of each panel requires knowing which triangle is programmed onto which OLED screen. In order to make this process simpler, every OLED screen also has the panel number printed faintly in gray in the upper left corner (similar how it is displayed in Figure 3.38). Also the panel numbers follow a predictable pattern on the dome, which is shown in Figure 3.40.

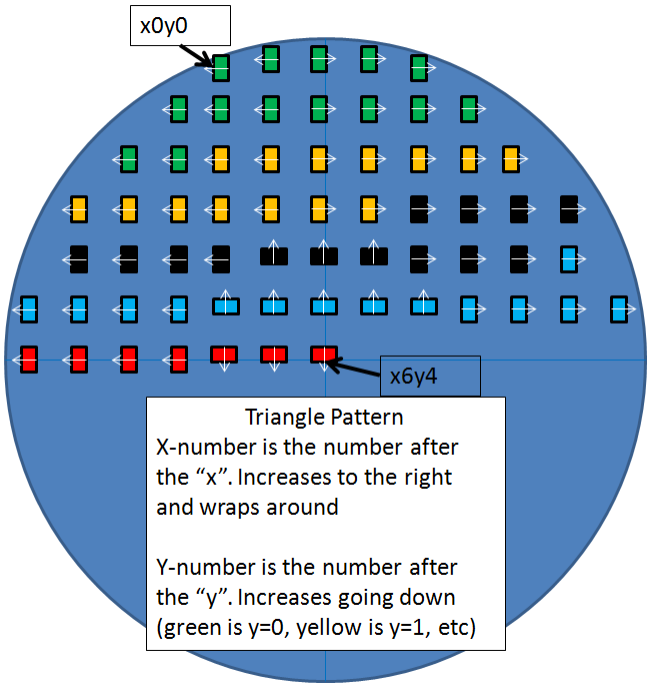

Figure 3.40: Programmed Triangles with Location on Dome

Once this pattern is known, the user just has to be consistent when measuring points with the FaroArm Edge. First, the axes and origin must be defined. On the optics bench, the axes were the camera frame axes when centered on the dome and the origin was the intersection of the two rotation stages' axes. Once these are defined, panel points can be recorded in this frame. This process is shown in Figure 3.41.

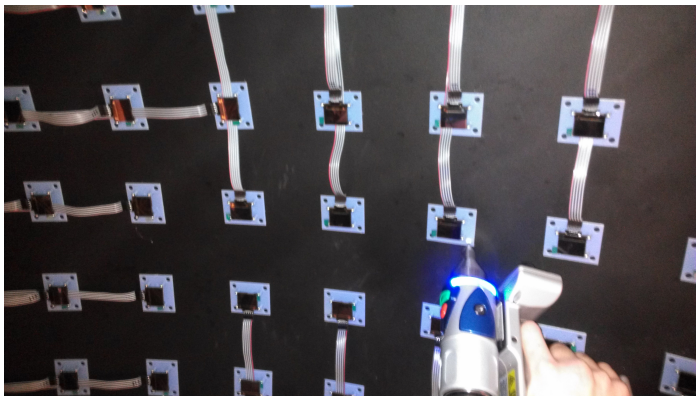

(a) Touching Panel Mount Indents to Generate Points

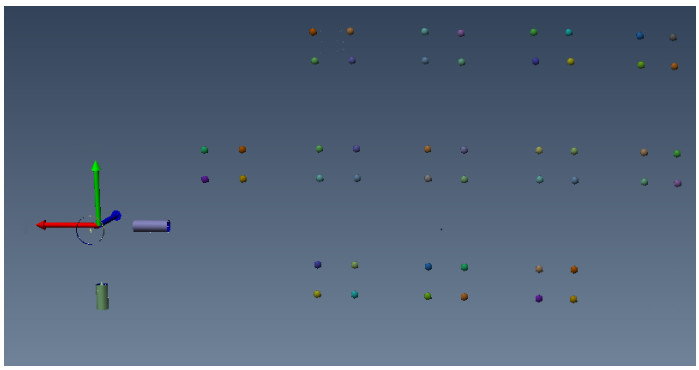

(b) FaroArm Point Cloud and Axes on Optics Bench

Figure 3.41: Physically Generating Panel Locations through FaroArm Edge

This process was repeated once the dome was moved back to above SimSat. The air bearing upon which SimSat sits was used to create a sphere object, as shown in Figure 3.42a. The centroid of this sphere is the origin of the coordinate system. The flat

cylinder top around the air bearing was used to create a plane to set the Z-Axis straight up (normal vector of this plane). This created the coordinate system shown in Figure 3.42b, which also shows all the cataloged panel points.

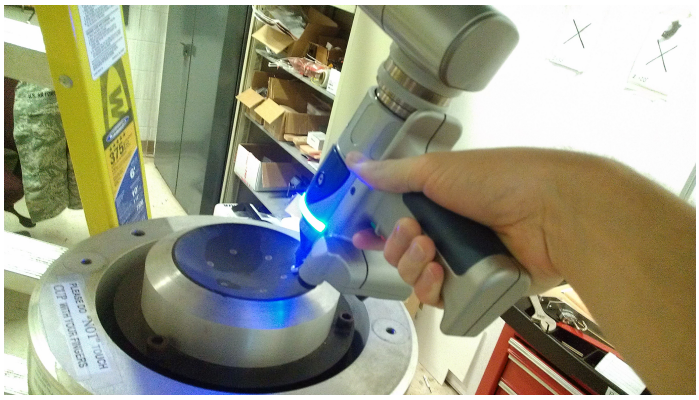

(a) Creating Sphere from Air Bearing to Find Center of Rotation for SimSat

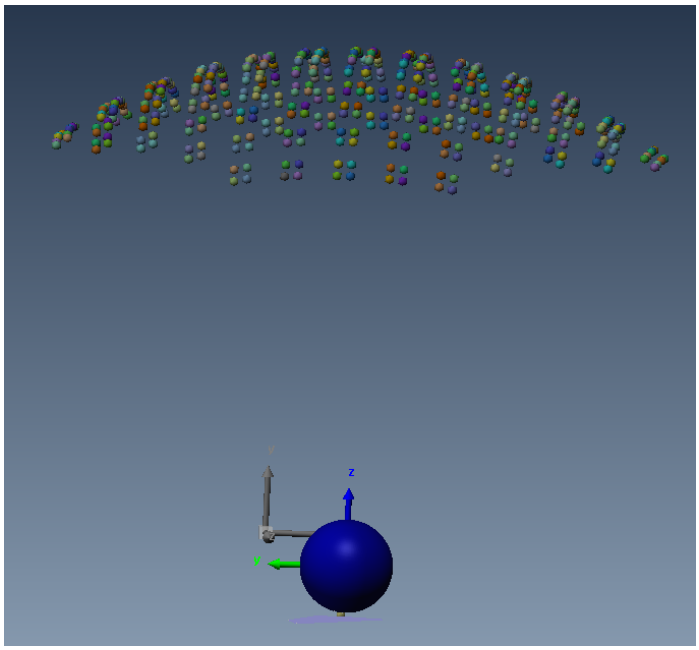

(b) FaroArm Edge Point Cloud and Axes on SimSat Frame

Figure 3.42: Physically Generating Panel Locations through FaroArm Edge in SimSat Frame

After this was done, there was a realization that a mistake was made and the Y-Axis or X-Axis were not set pointing a particular direction in relation to the physical geometry of the SimSat setup. This was a major oversight since it prevented truly knowing the position

of each panel, although their relative positions were still known. This oversight is discussed further in Section 4.2.

The user must be careful to record the points in the some order (CW or CCW) since for each panel a normal vector is calculated that is later used to locate the actual star centroids. Measuring the four points on each panels allows a plane to be fit using least squares. The centroid of the plane can also be calculated. This centroid gives the vector to the center of each panel mount. The vector to the surface of the OLED screen can then be calculated by simple vector addition as follows

$$\vec{r}_{Oxy} = \vec{r}_{Mxy} + \hat{n}_{Mxy} h_{screen} \tag{3.5}$$

where $\vec{r}_{Oxy}$ is the vector to the center of the OLED screen, $\vec{r}_{Mxy}$ is the vector to the panel mount, $\hat{n}_{Mxy}$ is the normal vector of the panel mount, and h_{screen} is the distance of the OLED screen from the panel mount along the normal vector. From $\vec{r}_{Oxy}$, the local screen coordinates can be used to position each star depending on which triangle was on that panel. Local screen coordinates are found from the panel mount catalog points. The local screen coordinates and the entire catalog process is shown pictorially in Figure 3.43.

Local "Y" ($\hat{r}_y$) is found by subtracting catalog point 1 from catalog point 2 and making a unit vector. Local "X" ($\hat{r}_x$) is found by subtracting catalog point 3 from catalog point 2 and making a unit vector. The distance along the local x or y screen axis to the fixed radius 4 star can be found through the following relations:

$$dx_1 = (91 - CP_x) \tag{3.6a}$$

$$dy_1 = (59 - CP_y) \tag{3.6b}$$

where dx_1 is the local x-distance in OLED pixels, CP_x is the center point along the local x-axis where $\vec{r}_{Oxy}$ is, dy_1 is the local y-distance in OLED pixels, and CP_y is the center point

along the local y-axis where $\vec{r}_{Oxy}$ touches the screen. Similiar relations can be developed for the other two stars (which depend on x and y increment numbers, described in Section 3.4.1, recall that dx and dy are equal to 5 OLED pixels):

$$dx_2 = (92 - CP_x) \tag{3.7a}$$

$$dy_2 = (3 + dy * Y_{num} - CP_y) \tag{3.7b}$$

$$dx_3 = (2 + dx * X_{num} - CP_x) \tag{3.8a}$$

$$dy_3 = (61 - CP_y) \tag{3.8b}$$

These values can then be converted into inches since each OLED pixel is 0.00835 inches square. This allows every star to be uniquely located through the following relation

$$\vec{r}_I = \vec{r}_{Oxy} + dx_i * \hat{r}_x + dy_i * \hat{r}_y \tag{3.9}$$

where $\vec{r}_I$ is the stored inertial vector for a given star and $*$ indicates scalar multiplication.

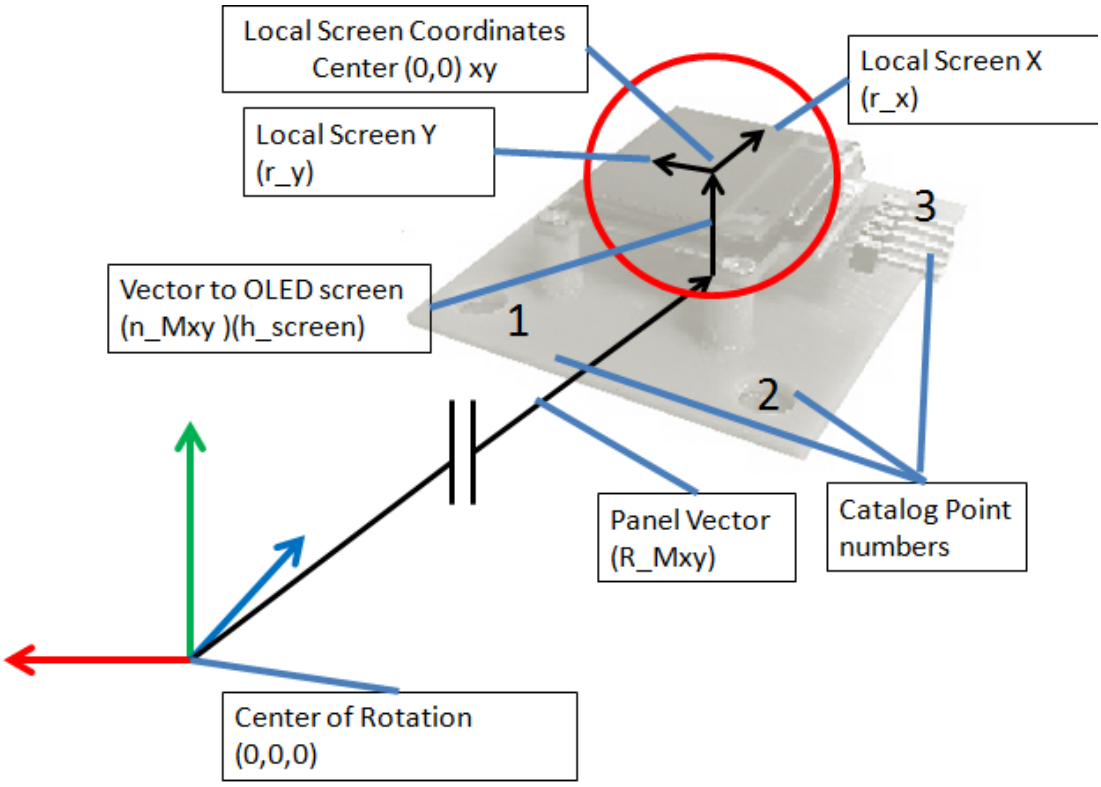

Figure 3.43: Knowledge of Panel Vector Allows Individual Star Vectors

One of the key assumptions this method hinges on is that the OLED screen is parallel to the panel mount. In order to check this, a plane was made on the screen and the normal vector from the screen plane was made in a dot product with the normal vector of the mount plane. Taking the inverse cosine of the dot product showed an angle between the two vectors of 0.102 degrees. This may induce some error into the star vector calculation method described previously, but there are larger issues with the FaroArm catalog method, which will be described next.

Another advantage that the FaroArm arm gives us is the ability to know the distance of each panel to the center of rotation. If the dome was a pure sphere then each panel would have the same distance; however, from trying to fit a sphere to the dome using the FaroArm arm revealed a 5% deviation from spherical shape. Figure 3.44 shows the measured vector

length deviations from the mean, which shows a surprisingly random deviation instead of a deviation that corresponds to dome coordinates.

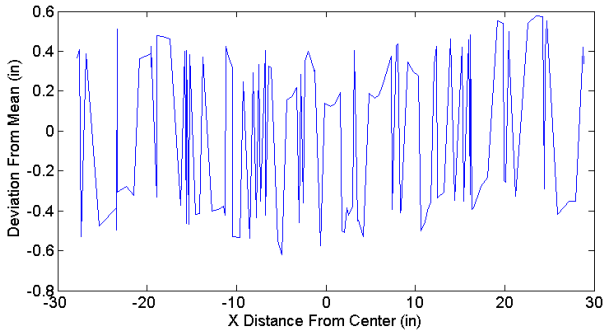

(a) Measured Vector Length Deviation From Mean Across X-coordinates

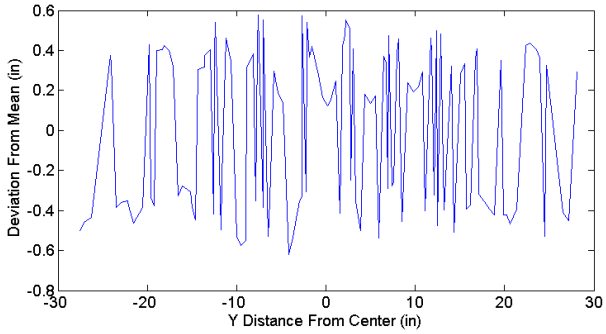

(b) Measured Vector Length Deviation From Mean Across Y-coordinates

Figure 3.44: Vector Length Deviation Showing no Correlation Across Dome Coordinates, Possibly From Bumping Dome When Measuring

The dome was shown to be an elliptical shape by Jorge Padro, so one would expect the mean variation to be positive near the outer edges in one direction and negative in the other. The randomness may be from dome vibrations caused by lack of lateral stiffness in the current dome hanging method, as shown in Figure 3.45. When measuring the dome

with the FaroArm, any slight bump would cause the dome to shake back and forth for several seconds.

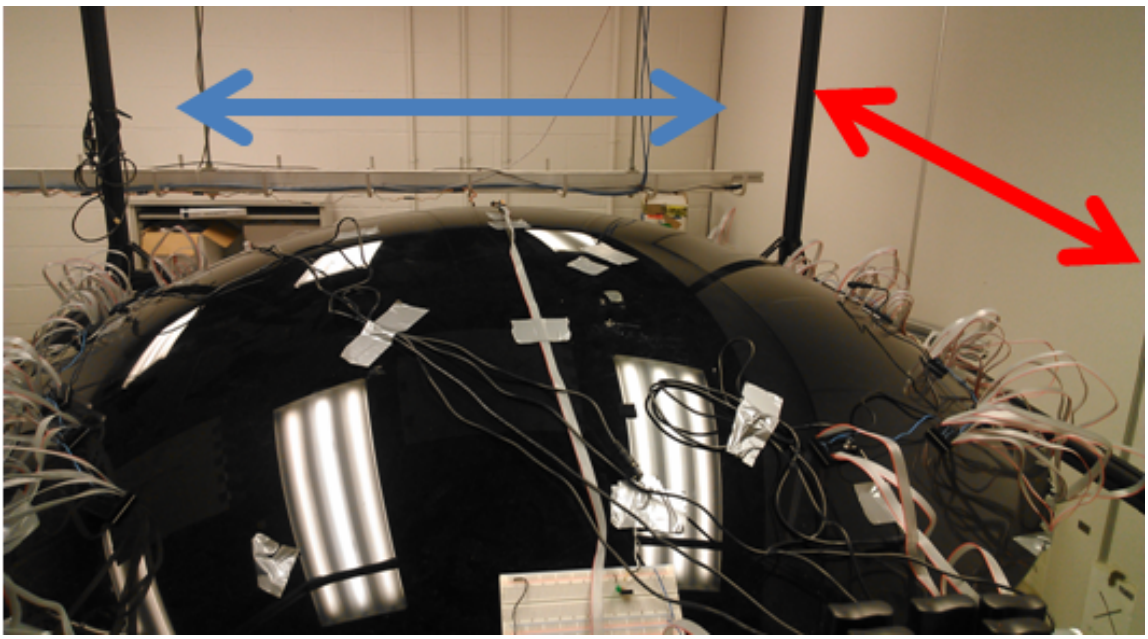

Figure 3.45: Top of Dome when Mounted Above SimSat Showing Weak Lateral Support, Shakes Easily in Blue and Red Arrow Directions

Because this stiffness issue was address late in the research, the main testing done in Section 4.2 was with the camera based catalog, which is described next.

3.4.3 Inertial Vector Generation via Camera.

This method still relies on an external attitude measurement when initially cataloging, but it does not require absolute knowledge of each panel's location, only the recorded location from the camera's perspective. In order to store the vectors seen by the camera in an inertial frame, the current attitude from the external source is stored in a rotation matrix, R^{ci}. The user inputs the camera's current Euler Angles to create this matrix. When the vectors are recorded by the camera, they are stored in the inertial frame by applying the transpose of the matrix, $(R^{ci})^T$. On the optics bench, the attitude measurement was done

with the Thorlabs rotation stages, while on SimSat the FaroArm was used to calculate the current attitude.

The process of using the FaroArm involves taking two points on SimSat which set the zero position (form the inertial set). As SimSat is rotated to a new position, the same points on SimSat are taken and the rotation is calculated using the QUEST algorithm. The points used were two of the holes previously drilled into the main SimSat frame, shown in Figure 3.46.

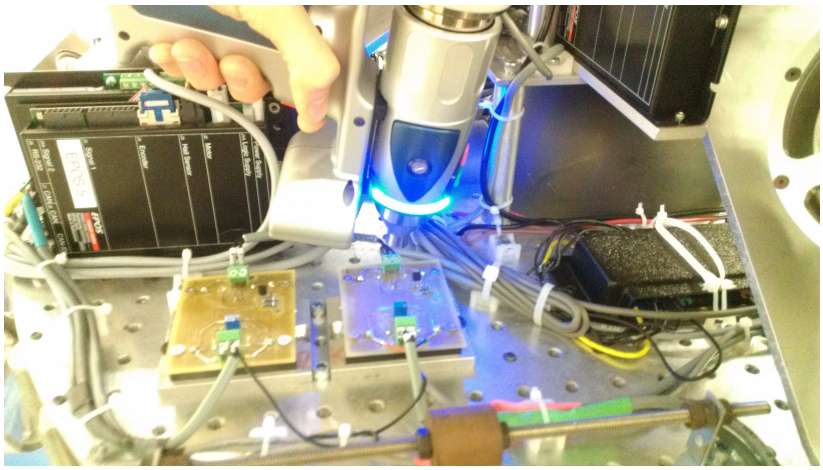

Figure 3.46: Using Holes on SimSat as Points for Vector Creation

This method works reasonably well as long as SimSat is secured in a fixed position, which is covered in more depth in Section 4.2.2.

3.5 MATLAB Algorithm Changes

Now that the new catalog methods have been described, some of the other algorithm changes will be covered in more depth. A large portion of the code is still very similar to the work done by Jorge Padro, which was covered in Section 2.4.1. The major additions to the software revolve automatically calibrating the image size, panel grouping and identification, and distance correlation correction from the FaroArm catalog.

3.5.1 Image Size Calibration.

Knowing distances in a given image in inches and OLED pixels (we know center panel is x6y4, so we know the distance in OLED pixels and in inches since we know the size of OLED pixels) allows us to measure how large those relations appear in CCD pixels on the camera. This allows us to determine the relation between CCD pixels and OLED pixels (necessary for panel ID) and also how large the field of view is in inches (necessary for vector construction). As a check, if we know the distance to the image, we can also estimate the focal length.

From the x6y4 panel, three separate distances are measured, one between each star pair (c1-c2, c2-c3, c1-c3). These distances are each known in real inches (0.3007,0.5774,0.4929 respectively). From the centroids of these stars, the distance in CCD pixels is calculated. An "inches per CCD pixels" is calculated with the average of each of these measurements in inches divided by the respective measurement in CCD pixels. A higher focal length will lead to a lower inches per CCD pixels value (since the camera will be further zoomed in, so less real inches are covered for the same amount of pixels). The standard deviation between the three measurements is also recorded. This value is usually between 0.9×10^{-4} and 1.2×10^{-4} inches per CCD pixels, which shows a consistent measurement. Converting inches per CCD pixel to OLED pixels per CCD pixels involves simply dividing by the size of each OLED pixel.

3.5.2 Panel Grouping and Identification.

With an accurate expected size correlation of OLED pixels to CCD pixels, the star patterns described in Section 3.4.1 can be quickly identified. However, before that the raw star centroids need to be grouped by panels present in an image. In order to do this, stars are only kept if they are within a certain distance of other stars. Currently this distance is 1.5 inches. This method rejects partial panels which may be at the edge of the FOV.

The panel grouping function that performs this task relies on the fact that the centroiding algorithm will sort the stars from most bright to least bright. This means all of the c1 stars (radius of 4) will be in the top section of the centroid list coming into the function. From this, if two stars are within the 1.5 inch radius they will be kept and added to the resorted centroid data. All of the stars within that distance are then dropped from the original list after being placed in the new list. If only one or no stars are within this distance, that star's centroid is dropped from the list.

This process produces a new list of star centroids sorted by panel. The order of the panels in the list since they will be stored in that same order and are converted to vectors as a panel group (3 centroids at a time). A pictorial view of what the function does is shown in Figure 3.47.

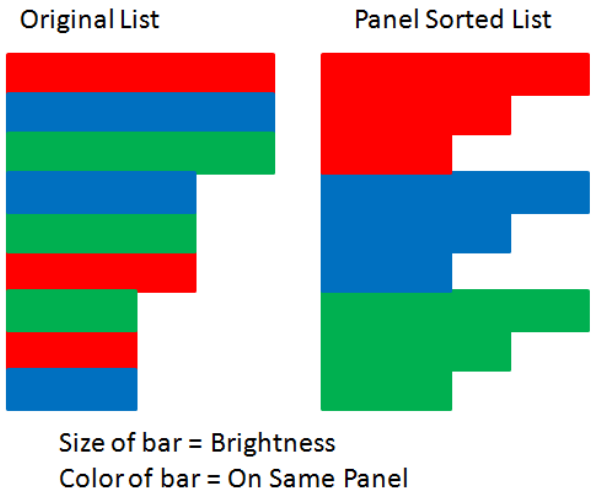

Figure 3.47: Grouping Star Centroids

Now that the centroids are sorted by panel, the panels present in the image will be identified. Each panel has a unique *b* length and *c* length, as described in Section 3.4.1. Since we can relate the x-number through Equation (3.3) and the y-number through

Equation (3.4), these distances can be calculated for each panel and the minimum deviation from the ideal value is selected as the panel numbers. The only missing piece is knowing the relation of OLED pixels (which is known and relates to the panel numbers) to CCD pixels (which is measured from relations between stars on a single panel). These value is determined before the rest of the software is run as described in Section 3.5.1. From this function we now know which panels are in a given image and which centroids relate to the stars on those panels. The next task is to convert those centroids into vectors that can be compared to the inertial catalog. Knowing the distance to each panels allows us to more accurately convert the centroids to vectors, as described in the next section.

3.5.3 Distance Correlation Correction.

As shown in Section 3.4.2, the distance to each panel is not the same. The vector length correction method described in Section 2.4.1, assumes that this distance is the same. However, since we know the distance to each panel, this value is used instead of the nominal dome radius to create vectors from the star centroids. The effect of this addition has not been isolated, but it may be an area of future work after the dome has been stiffened and re-cataloged.

3.6 System Validation Approach on SimSat

The FaroArm has a reported certainty in position of 0.091 mm (1σ), so to determine the "NEA" of this method of calculating attitude this uncertainty was added to the two original points taken by the FaroArm. The attitude was then calculated over 40 trials to see how much the calculated attitude from zero. The noise with this method came out to be 0.0063 degrees in the worst case about a single axis. This tells us that if our solutions from the camera match the FaroArm solutions within that amount, then the system can achieve an accuracy level of at least that much, but we cannot verify accuracy levels below that amount.

IV. Results and Analysis

This chapter will be about summing up the results from the optics bench test and then focusing on the current performance of the system at the end of this research effort. It will present the results for the accuracy and other relevant parameters that were developed in the methodology section.

4.1 Optics Bench Experiment Results

This section will cover the results of the tests performed on the optics bench. The goal of moving to the optics bench was to try and narrow down on possible sources of error with the camera and optics, test the capabilities of the OLED panels, and make the full population of the dome easier to accomplish since the dome would not be directly overhead. However, the absolute accuracy of the system at this point was not the main focus since that would depend on precisely knowing the center of rotation, which would have to be recalibrated for at SimSat once the dome was moved back. First, the results of the comparison tests between the two cameras (Lu205c being the color camera and the Lw235m being the monochrome camera) will be presented. Then, the influence of ambient light on the NEA is briefly covered. Next, the center swath of the dome is tested. Finally, a short investigation into the actual repeatability and accuracy of the rotation stage used is discussed.

4.1.1 Camera Comparison.

This thesis effort began using a color camera, the Lumenera Lu205c. As the effort evolved, it was became apparent that maybe the color filter placed over each pixel as described in Section 3.2.3.5 might be causing an increase in the NEA and a subsequent loss in accuracy since each pixel is not receiving full light input. The camera also automatically interpolates between pixels to guess the true color, so the star appears to have many different

colors and corresponding intensity values as a result of the filter pattern and not purely a normal intensity decrease from the centroid. This pattern is shown in Figure 4.1, where the black and white camera (Lw235m) has a intensity decrease much more uniform spatially than the color camera.

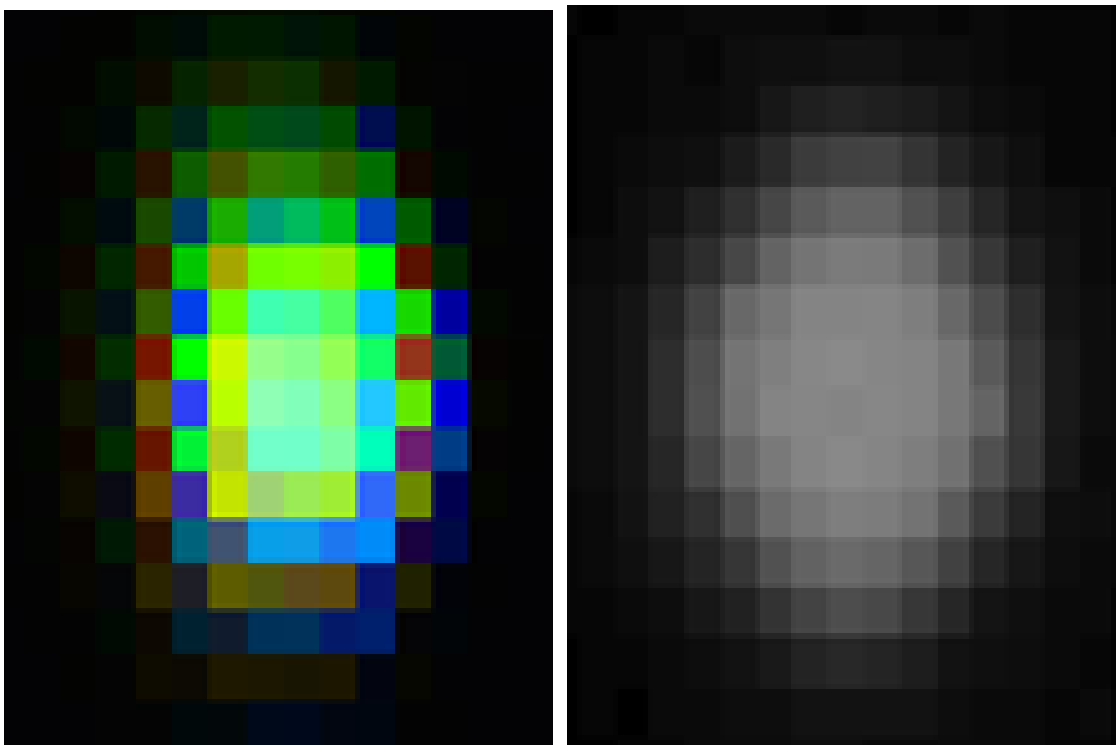

(a) Lu205c Color Star Picture Showing Jagged Intensity Decrease From Color Filters

(b) Lw235m Monochrome Star Picture Showing Spatially Uniform Intensity Decrease

Figure 4.1: Color vs. Monochrome Star Picture

In order to compare these two cameras, the same optic piece was used. A 25mm lens was used because it allowed three starfields in the FOV on the optics bench. Both accuracy and NEA were tested simultaneously in the following manner. First, the three star fields were cataloged with the method described in Section 3.4.3, and then rotated about the X-axis (boresight) and Y-axis (up/down) 2.5 degrees each. This is recorded as position 1

in Table 4.1 for the Lu205c color camera and in Table 4.2 for the Lw235m monochrome camera. Position 2 is another 2.5 degree rotation about each axis for a total of 5 degrees each. The error is then calculated based on the assumption that the rotation stages are "truth". This assumption proved to be inaccurate, as discussed in Section 4.1.4.

Table 4.1: Lu205c Color Camera Results

Component	Position 1	Position 2	Mean
EA_X Error (deg)	0.0277	0.7567	0.3922
EA_Y Error (deg)	0.0726	0.1367	0.1074
EA_Z Error (deg)	0.2425	0.3445	0.2935
NEA (deg)	0.0022	0.0016	0.0019

Table 4.2: Lw235m Monochrome Camera Results

Component	Position 1	Position 2	Mean
EA_X Error (deg)	0.3028	0.3941	0.3485
EA_Y Error (deg)	0.0344	0.0572	0.0749
EA_Z Error (deg)	0.0285	0.1214	0.0458
NEA (deg)	0.0012	0.0009	0.0010

Taking the root mean square of the errors results in an estimate of the magnitude of the total angular error. For the Lu205c, this value is 0.5009 degrees, compared to 0.3593

for the Lw235m. At this point in the research, the center of rotation was not precisely fixed relative to the dome as it would be when moved back to SimSat. For this reason, the angular error was not a huge driving factor in the decision on which camera to go with. The main decision was based upon the NEA, since that is the ultimate noise floor for the system. In this regard, the Lu205c (0.0019 degrees) had a 90% increase in noise angle over the Lw235m (0.001 degrees). This fact, along with the consideration that the Lw235m had to transfer only one third of the data made it a clear favorite.

The Lw235m only needs to pass one full 1216x1616 frame, while the Lu205c has to download three 1200x1600 frames (one for red, blue, green respectively). In order to confirm the suspicion that the Lw235m should allow a better update rate of the system, a simple speed test was conducted. First, ten pictures were taken with each camera and then fourty pictures were taken. These values were recorded and a linear fit was taken to estimate startup time and how many seconds each picture took to transfer. These tests are summarized in Table 4.3.

Table 4.3: Camera Capture and Download Speed Comparison

Camera	Time for 10 Pics (s)	Time for 40 Pics (s)	Startup Time (s)	Second/Picture
Lu205c	3.1	10.2	0.73	0.24
Lw235m	1.6	4.3	0.70	0.09

There is also another advantage utilizing the Lw235m in that it has a better sensitivity to light, so the aperture setting of the lens can be set to a lower value if needed. Increasing the aperture would allow a greater depth of focus in the image in case dome distance variability causes some stars to be out of focus relative to the other stars (which would

make the centroiding algorithm inconsistent). The greater flexibility when it comes to aperture settings also permits different ambient light conditions, which is the focus of the next set of results.

4.1.2 Ambient Light Influence Tests.

Since the optics bench allows easily control of external light through the plastic shroud, tests were performed to ensure that the system could operate in variety of light conditions so that the SimSat room would not need to be modified for successful operation. The general light conditions tests were as follows:

- Full shroud coverage allowing minimal ambient light to fall on the dome, as shown in Figure 4.2b. This light condition is most similar to how the SimSat room would be if the lights were turned off when testing.

- Half shroud coverage which allows diffuse light reflecting off the floor and some of the walls to reach the dome. This case is most similar to how SimSat would operate under normal light conditions since the walls and floor is the same material. This set up is depicted in Figure 4.2d.

- No shroud cover at all which was designed as a worst possible test case. This situation has a light directly above the dome(see Figure 4.2e), which would never happen in the SimSat room. However, if the system can operate in this light condition then we know that it can definitely operate above SimSat.

(a) Fully Shrouded Optics Bench

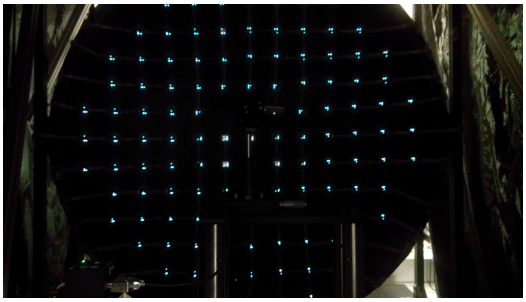

(b) Fully Shrouded Internal View

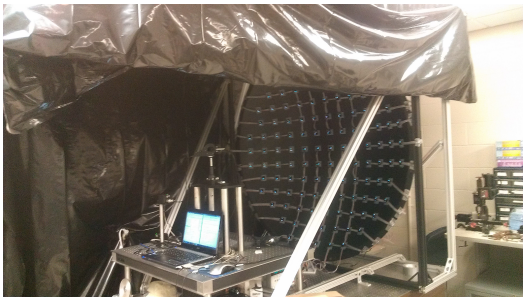

(c) Optics Bench Half Shrouded

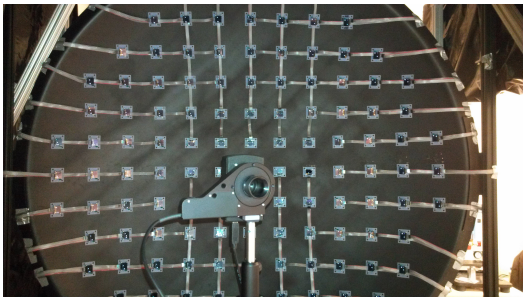

(d) Half Shrouded Internal View

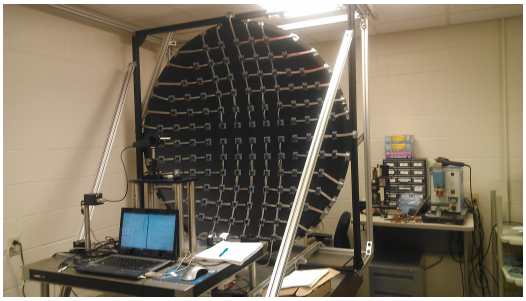

(e) Optics Bench No Shroud

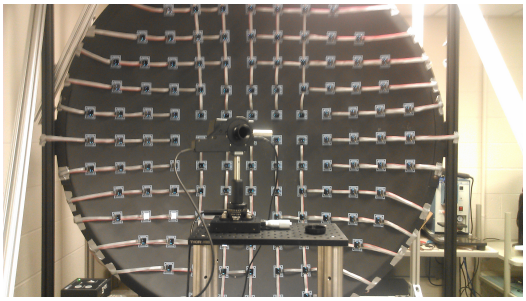

(f) No Shroud Front View

Figure 4.2: Different Ambient Light Testing Conditions

All of the preliminary tests described in the methodology were performed with the setup shown in Figure 4.2c. The main focus on these tests were if the NEA would be affected under adverse light conditions and how the centroiding algorithm would have to be adapted to change the sensitivity of star detection. As described in Section 2.4.1, there are two main thresholds the user can select, area and intensity. If a pixel is below the percentage

intensity chosen of the brightest pixel in the image, then it will not be considered part of a star. Continuous sections of these "stars" make up an area; however, the algorithm will reject the star if it does not meet the area threshold. This allows small reflective bright spots to be easily rejected without raising the intensity threshold to high to not allow enough light from the real stars. The test results under the various light conditions are summarized in Table 4.4.

Table 4.4: Ambient Light NEA Comparison

Shroud Condition	NEA (arcsec)	Intensity Lim	Area Min (pix^2)	Avg. False Stars
Fully On	2.28	0.15	6	0
Half On	2.26	0.30	12	0.2
Fully Off	1.93	0.4	16	16.4

This table shows that the algorithm can perform effectively under all light environments. Also note that the NEA is lower here than in the tests in Section 4.1.1. This is likely from the addition of the new 12mm-36mm varifocal lens being utilizing near 17mm focal length to allow a wider FOV that includes nine panels at time. These results also show that the centroiding algorithm will likely have to be adjusted slightly to account for the light conditions present in the SimSat room. This confidence in the adaptability of the system allowed the research to move forward to verifying the performance of the cataloging methods over a large section of the dome.

4.1.3 Full Dome Center Swath Tests.

Initially, the FaroArm catalog method described in Section 3.4.2 was attempted. However, the accuracy at the zero point was more than one degree in two axes, so the focus

shifted to the camera cataloging method. The FaroArm method was tested again once the dome was above SimSat and the center of rotation was more precisely known. The next step was to verify the camera catalog methodology and better understand the system by cataloging multiple panels and sweeping across the dome to see how accuracy varied. This is depicted graphically in Figure 4.3.

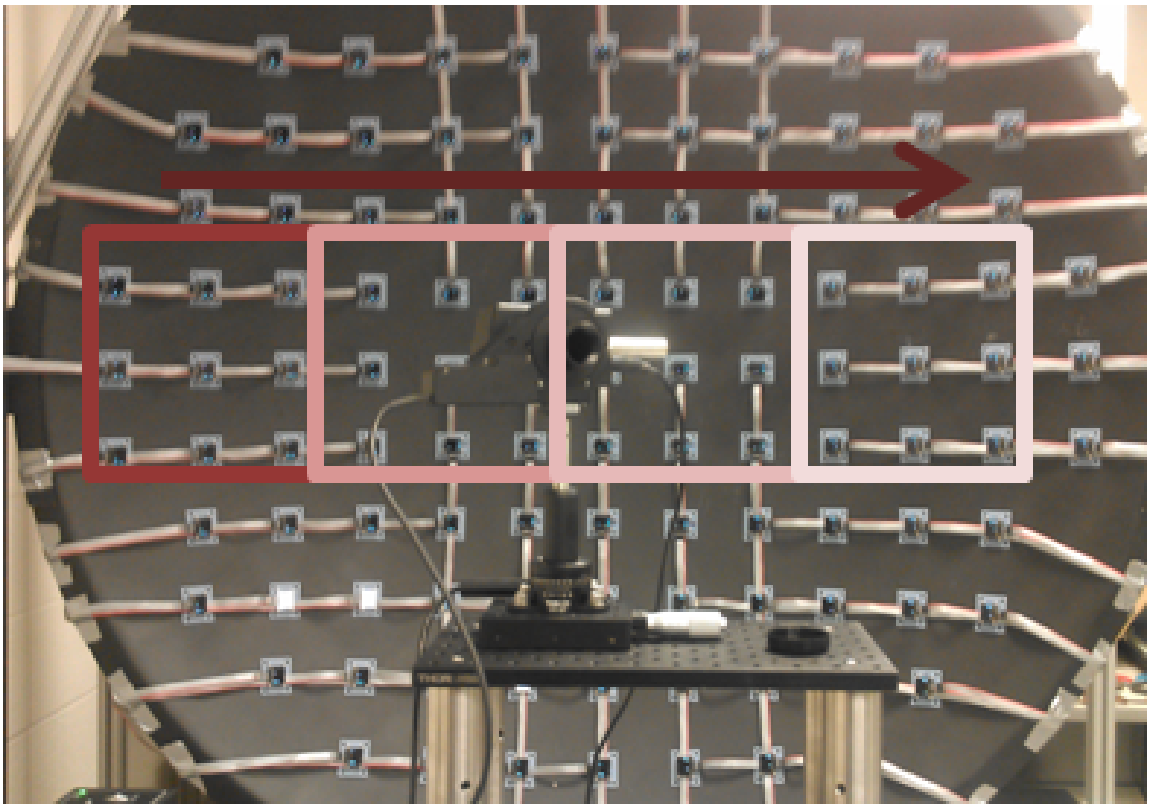

Figure 4.3: Catalog Sweep Process: Each Square is One Catalog Section and Error is Lowest When Two Different Catalog Sections Are Not Both Used

First the left side of the dome was cataloged utilizing the Euler Angle position given by the rotation stages, then the camera was rotated 18 degrees to see a whole new set of nine panels and the process repeated from -30 to 24 degrees (Euler Angle Y) which cataloged the center swatch of 36 panels. After the cataloging is complete (done from darkest red to

lightest red shown in Figure 4.3), the camera was rotated back to the original position at -30 degrees Euler Angle Y. The camera was then rotated by 2 degrees at the time and the rotation solution was recorded. The error from each Euler Angle is shown in Figure 4.4.

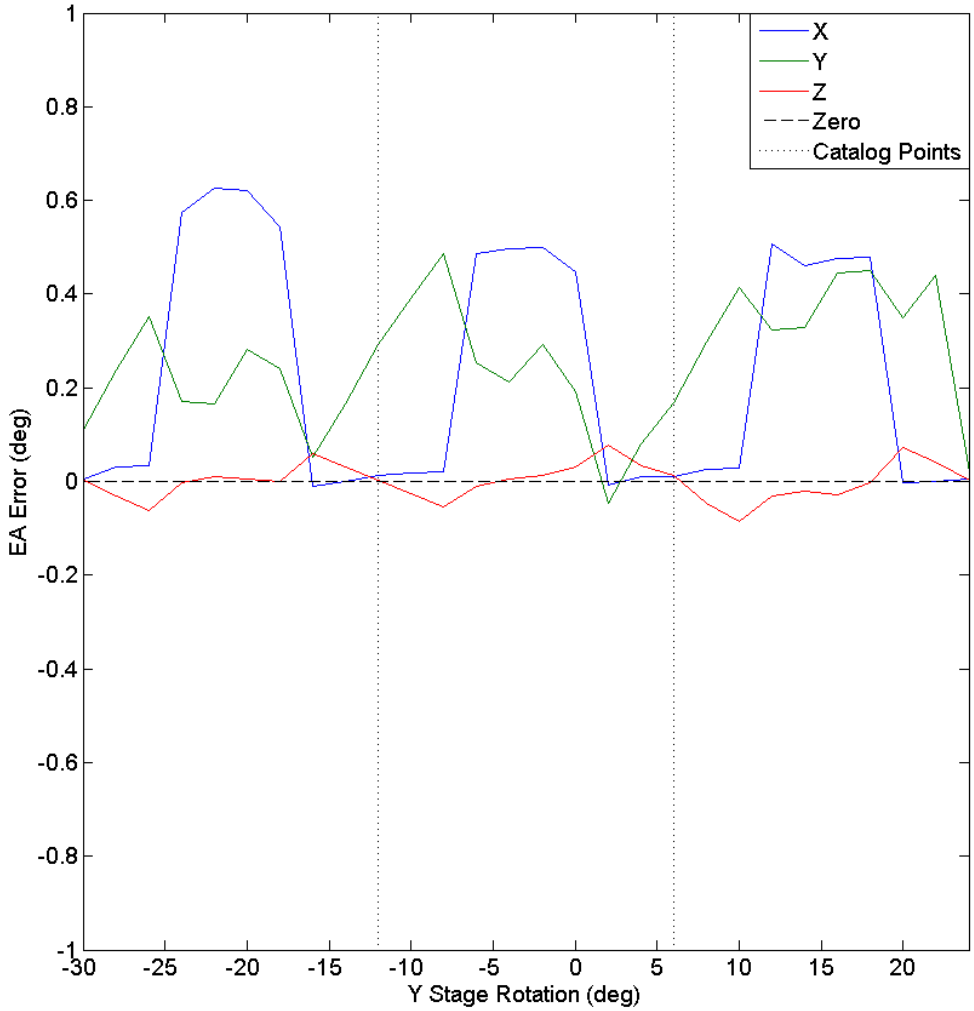

Figure 4.4: Error in Each Euler Angle When Sweeping Across Dome Fully Cataloged

The striking increase in error between catalog points comes from utilizing catalog information coming from two different images. This could be an effect from lens distortion since the edges of each image will be used when cataloging. One way to avoid this is to only use information from two different catalog images when absolutely necessary. However, this error may also be an artifact in the inaccuracy of the rotation stages to begin with, so it will be more extensively tested on SimSat.

Upon more closely examining the error trend present in Figure 4.4, the error pattern is clearly visible. The error about the Z axis is almost sinusoidal and the error about the X axis jumps up to consistently the same level. This suggests that the error is systematic and can be accounted for through more testing.

Another test was performed that followed the same catalog routine as previously described. This time a full sweep was done with the X stage set at 0 degrees, shown in Figure 4.5a. Then, the X stage was rotated 45 degrees and the sweep across the Y-axis was repeated, shown in Figure 4.5b. Next, the X stage was rotated another 45 degrees, for a total of 90, which is shown in Figure 4.5c. Finally the X stage was returned to zero and the sweep was performed again to test for consistency, see Figure 4.5d.

If the rotation stages were repeatable to their reported levels then the repeat of the X stage at 0 degrees should reveal a similar error pattern to the original sweep (Figure 4.5a). However, the X error is near 0.75 degrees throughout the entire final sweep (Figure 4.5d). The other sweeps also show an error pattern. The lack of consistency really pointed at something being wrong with the accuracy of the rotation stages, so that was the next point of investigation.

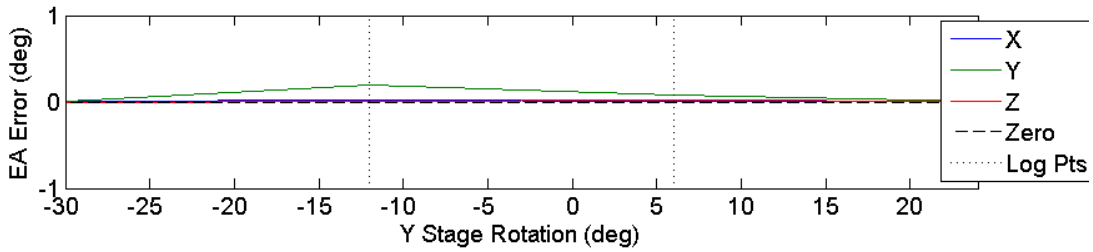

(a) Catalog Sweep With X-Stage at 0°

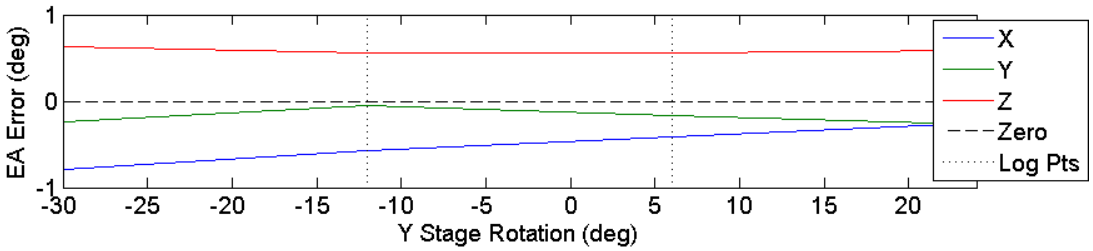

(b) Catalog Sweep With X-Stage at 45°

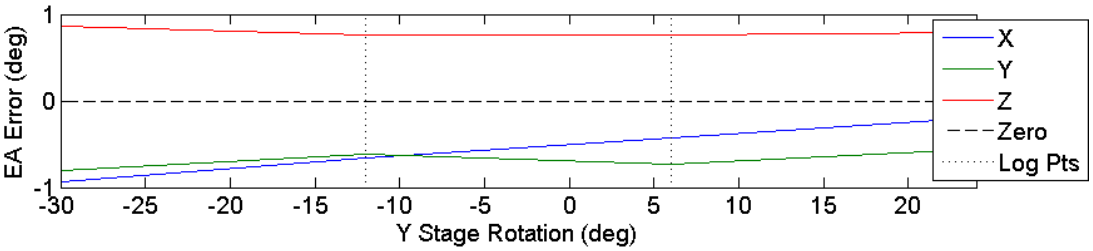

(c) Catalog Sweep With X-Stage at 90°

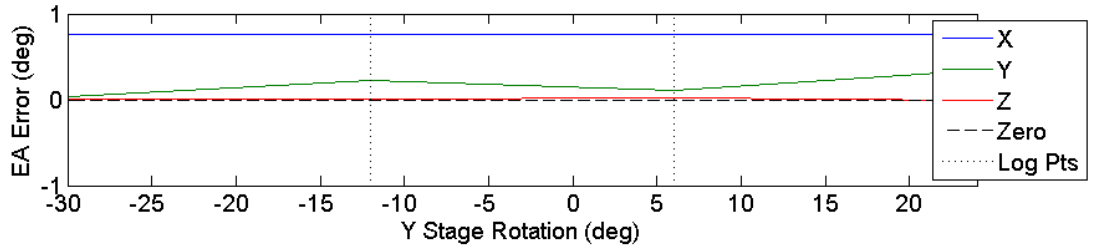

(d) Catalog Sweep With X-Stage at 0° to Check Consistency

Figure 4.5: Error in Each Euler Angle When Sweeping Across Dome Fully Cataloged With an X-Rotation

4.1.4 Lack of Calibration in Rotation Stages.

With the NEA being so small compared to the error found when comparing the measurement to the rotation stages' position, the idea that the accuracy of the rotation stages might be worse than listed was formed. The problem was hypothesized to be coming from gear lash when the system starts up or changes direction. In order to investigate this, each stage was commanded by its smallest incremental step up and then decremented by this same amount. The first test with the X rotation stage is shown in Figure 4.6.

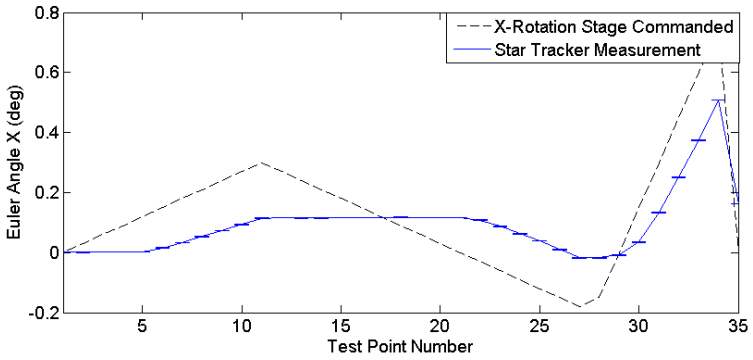

(a) Gear Lash Effect Apparent as Measurement Lags Behind Commanded Position

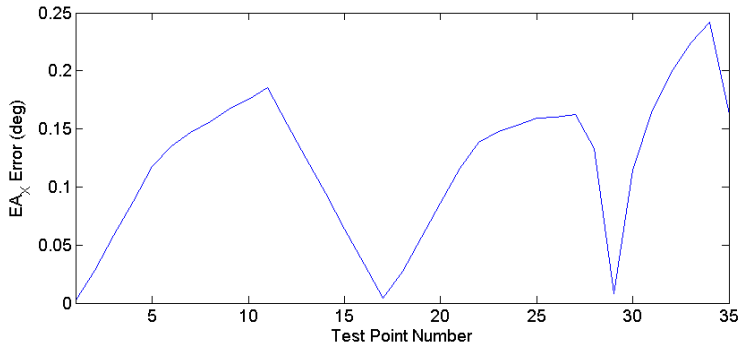

(b) Trajectory Errors May Also be Present Shown by Error Arcs Instead of Sharp Lines

Figure 4.6: X-Rotation Stage (PRM1-Z8E) Gear Lash Effect

The latency between the commanded and the measured is apparent in Figure 4.6a. Another problem is also revealed in Figure 4.6b. Once the measured angle value begins to change, the error should be fixed at a constant offset value assuming this is when the actuator gear catches and actual rotation begins. Instead it appears the error grows and then plateaus above the initial offset value.

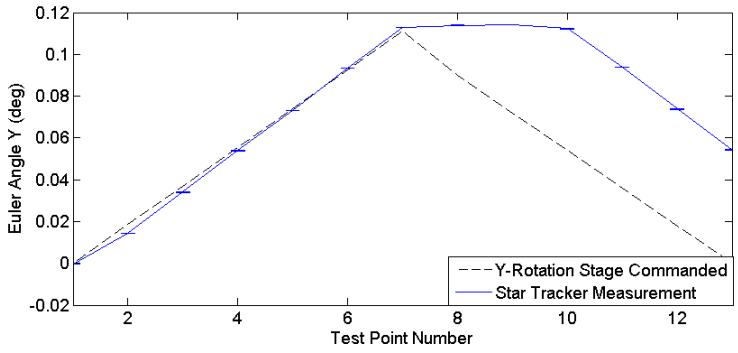

(a) Gear Lash Apparent When Changing Directions in Y-Rotation Stage

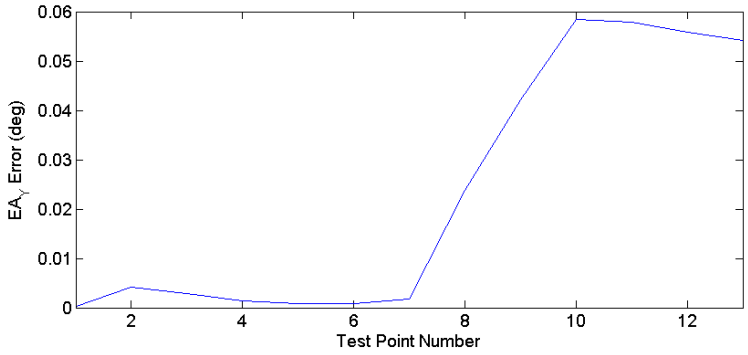

(b) Trajectory Errors Also Present in Y-Rotation Stage, But Less Severe

Figure 4.7: Y-Rotation Stage (CR1-Z7E) Gear Lash Effect

In Figure 4.7 the Y Axis rotation stage's gear lash problem is clearly shown as it transitions from one direction back to the other. There is less of an error creep problem with this rotation stage and as once it stages moving, the error stays constant.

Although these issues with the rotation stages prevented the high precision measurement that was expected, there much gained through there utilization on the optics bench. If this effect was discovered earlier, then the proper calibration techniques could have been performed, but this effect was not realized until late in the this research. However, the feasibility and basic performance of the system was shown to be acceptable on the optics bench and full panel population was achieved, so the next step was to test the accuracy with the dome mounted back above SimSat.

4.2 Back on SimSat

This section will discuss the current state of the SimSat star tracker system. After moving the dome back above SimSat, the centroiding algorithm parameters were adjusted to best match ambient light conditions by reaching a similar NEA. After this was done, tests were performed to reveal the true accuracy of the system. First, rotations focused on just the center of the dome were performed to provide a quick validation of the methods used and limit other performance variables, such as the dome distance variability. Then, the entire center swath of the dome was cataloged in a method similiar to Section 4.1.3 to ensure accuracy over a large range of motion. Testing of the entire dome will take place once the dome structure is fully reinforced.

4.2.1 Rotations Near Center.

In order to quickly valid the approach on SimSat without dome radius variations causing too much of a problem tests pointed near the center of the dome were performed first. The camera based catalog approach was used first since that was the most successful on the optics bench. Then the FaroArm built catalog was utilized to compare.

4.2.1.1 Utilizing Camera Based Catalog.

Since camera catalog feasibility was demonstrated on the optics bench, this was the first approach tested. A set of stars could be cataloged and then SimSat could be manually rotated. After this manual rotation the FaroArm method was utilized to verify accuracy as discussed in Section 3.6. This first initial test just focused on rotating SimSat around the camera's boresight axis, as depicted in Figure 4.8.

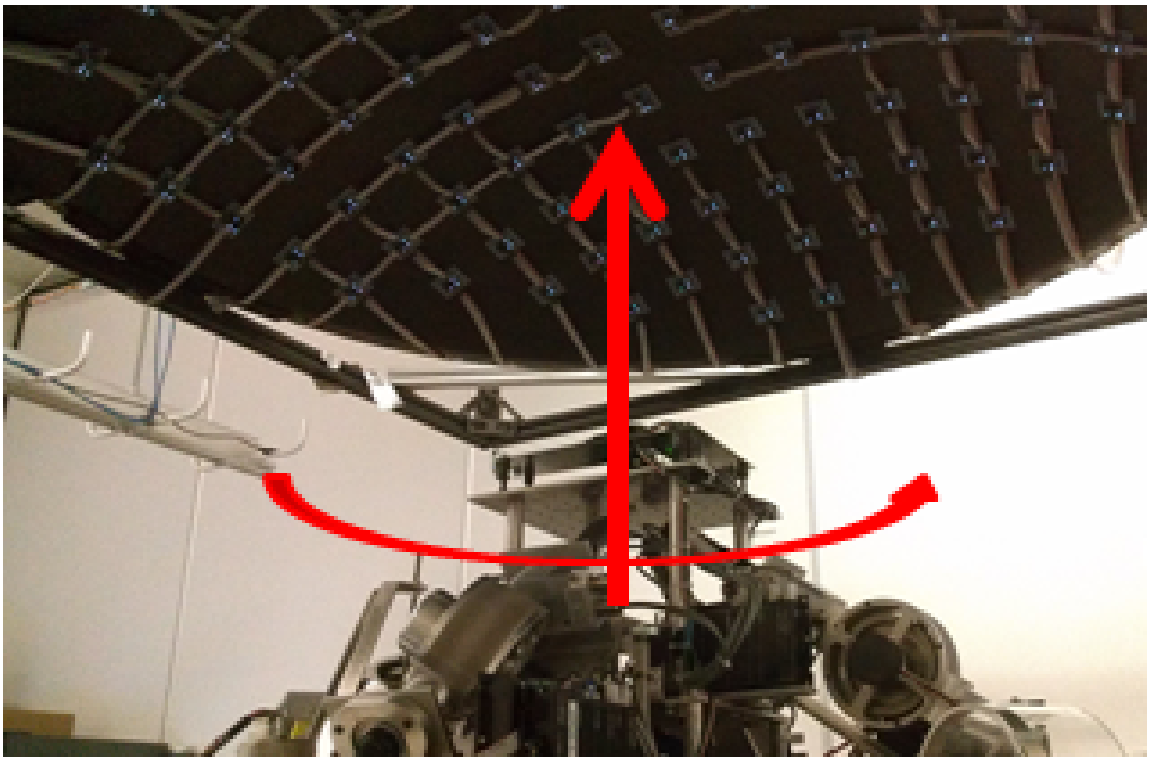

Figure 4.8: SimSat Test 1 Set Up, Rotation About Boresight

The manual rotation values were approximately 8, 18, and 24 degrees. After each rotation SimSat was lowered back down upon the air bearing with the air compressor running. The vectors were recorded with the FaroArm and the camera. the results of these tests are summarized in Table 4.5.

Table 4.5: SimSat Star Tracker Accuracy Test 1

Component	Position 1	Position 2	Position 3	Mean
EA_X Error (deg)	0.0029	0.0121	0.0182	0.0111
EA_Y Error (deg)	0.0096	0.0177	0.0018	0.0097
EA_Z Error (deg)	0.0108	0.0045	0.0427	0.0193

These results show the real accuracy of the system and a root mean square error of 0.0243 degrees. This is a great starting point, especially since the focal length used was around 20 mm, so only three star panels were visible. The expected FOV on SimSat was actually higher than anticipated, so the focal length can be decreased to around 12 mm to capture nine panels in the FOV. The FOV being higher than anticipated was probably from a calculation mistake, but this allows a variety of focal lengths to be effective, which adds to the depth of testing possible. Comparing the 12 mm FOV with the 20 mm FOV is shown in Figure 4.9.

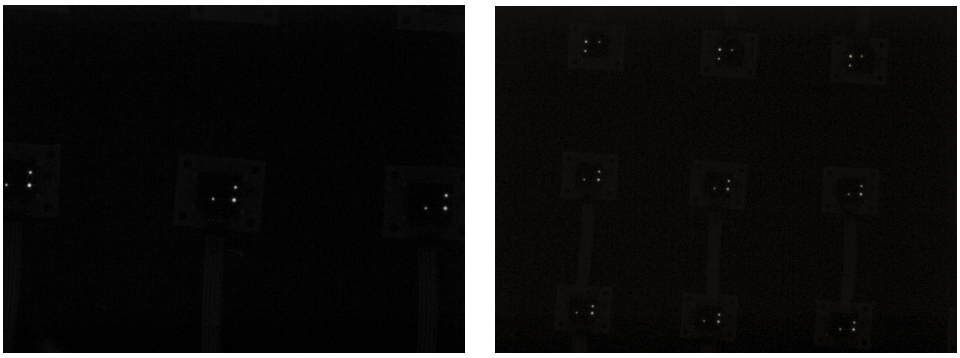

(a) Lw235m View, Approx 20mm focal (b) Lw235m View, Approx 12mm focal

Figure 4.9: 12mm vs. 20mm Focal Length Comparison on SimSat

The extra panels in the FOV allows for faster cataloging of the entire dome if the solution is as accurate. The same method was applied with this FOV. The stars were cataloged and then SimSat was rotated around its boresight axis. In this case, the rotation was 3 degree and then 10 degrees. The results were not as accurate and are summarized in Table 4.6.

Table 4.6: SimSat Star Tracker Accuracy Test 2

Component	Position 1	Position 2	Mean
EA_X Error (deg)	0.0478	0.057	0.0524
EA_Y Error (deg)	0.0014	0.0361	0.0188
EA_Z Error (deg)	0.107	0.0948	0.1009

Using the 12 mm lens setting resulted in a root mean square error of 0.1152 degrees, which is 4.74 times higher than using the 20 mm lens setting. There could be several possible reasons for this drop in accuracy:

- First, a drop in focal lengths means a loss of angular resolution per pixel. However, this effect should manifest in the NEA as well since any small stimulus variations should be magnified in their uncertainty when converted to vectors with a loss of real angular (and inchwise) resolution. The NEAs of both set ups were comparable (2 arcseconds for 20 mm and 2.5 arcseconds for 12 mm), so this is probably not the main cause

- Another possibility is that the lens has increased distortion at the far ends of the varifocal range. According to the Computar Ganz M3Z1228C Spec Sheet, the distortion can be up to -2.6% when at minimum focal length.This could cause the

NEA to stay comparable since the same optical stimulus would not be largely affected by distortion since it will be distorted the same every time. When rotating, a different part of the FOV will be distorted which could cause an incorrect set of vectors to be created. This is probably the main cause so if the 12 mm setting is to be used then a distortion map will need to be made.

Since the dome was moved back above SimSat later than expected, time was not available to do a distortion map for the 12 mm lens setting, thus the 20 mm setting was used going forward.

Note that only a few positions were used in both test 1 and test 2 because MATLAB kept crashing on SimSat in the current configuration. SimSat runs Windows XP and MATLAB 7, but the software ran fine when doing singular tests. In order to make the process of measuring with the FaroArm after every picture go faster, MATLAB was programmed to wait until a key was input to take the next picture. This would usually last anywhere from 2 to 5 pictures before MATLAB would crash and all data would be lost. This caused a delay and serves to highlight the importance of budgeting time for unanticipated errors, but was eventually fixed and work was able to be resumed.

4.2.1.2 Utilizing FaroArm Based Catalog.

The FaroArm catalog construction described in Section 3.4.2 was not able to be fully tested in this thesis effort. Before the catalog was utilized, the mistake of not fixing the Y-Axis or X-Axis in a particular direction before cataloging the panels was recognized. This meant that, although their distances were correct relative to each other, a true catalog relative to a fixed frame could not be created . Since the dome vibration issue also showed that even if the correct axes had been chosen, the cataloged positions may change with any interaction with the dome frame. Stiffening the dome and correctly creating the FaroArm catalog will be one of the immediate items for future work. The FaroArm catalog as a possible viable option was still investigated by determining the step accuracy, which is the

measured angular values between two rotations. This approach is tested more thoroughly over the entire dome as described in Section 4.2.2.2.

4.2.2 Rotations Over Entire Dome.

In order to show that SimSat can correctly determine its attitude over the full range of motion, the rest of the stars need to be correctly cataloged. Since the FaroArm catalog was set up in an unknown reference frame, the catalog had to be created with the camera. This involved moving rotating SimSat to view different panels and recording the rotation with the FaroArm as described in Section 3.4.3.

The tests performed about the X and Y axis of SimSat were done by weighing down one side of SimSat with a five pound cylindrical weight and lowering the support cage. This would cause SimSat to tilt to one side thereby creating a fixed rotation about the X or Y axis which could be increased or decreased by lowering or raising, respectively, the support cage. A depiction of this approach is shown in Figure 4.10.

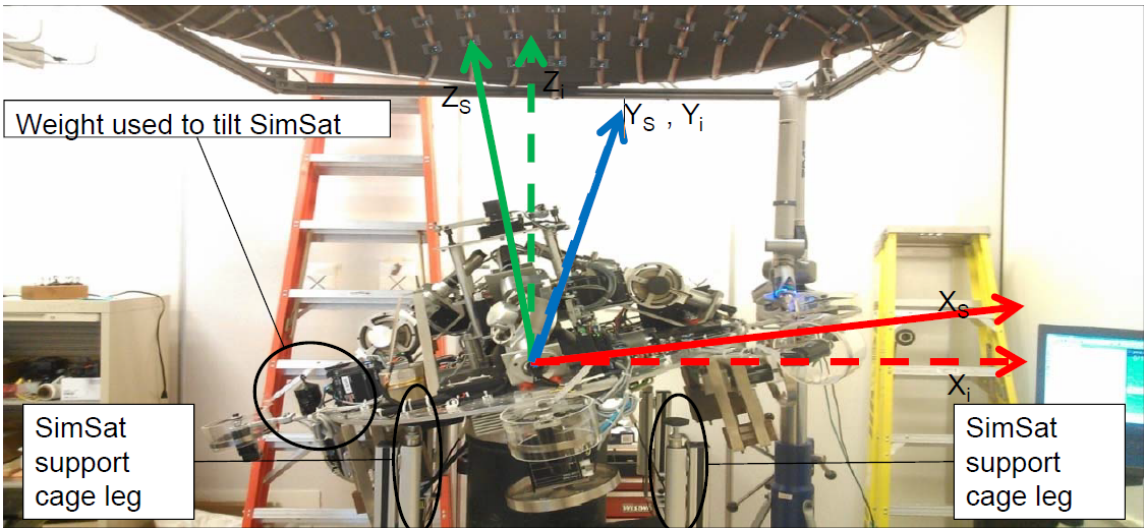

Figure 4.10: SimSat Coordinate Systems and Rotation Setup with a Rotation about Y-axis Shown

This method of cataloging with the camera was limited in range of motion to +/- 15 degrees about the X and Y axes, which is about half the full range of motion of SimSat. In order to catalog the full range of motion with the camera, an entire new support cage would have to be developed, so utilizing the FaroArm catalog would be ideal. Even though the FaroArm catalog was built incorrectly at the current time, the FaroArm catalog's feasibility can still be shown as discussed in Section 4.2.2.2. Before delving into that, the accuracy results from using the camera catalog will be discussed.

4.2.2.1 Average QUEST versus Full QUEST approach.

When rotation tests were done over the accessible range of motion, there were significant errors introduced using the full QUEST algorithm. Upon further testing, each individual panel was producing a more accurate solution through the QUEST algorithm than the combinations of panels being put into the QUEST algorithm. This was very puzzling since the QUEST algorithm produces an optimal estimate of the attitude based on the vectors given, so more information should yield a more accurate solution, given the same variance of each measurement.

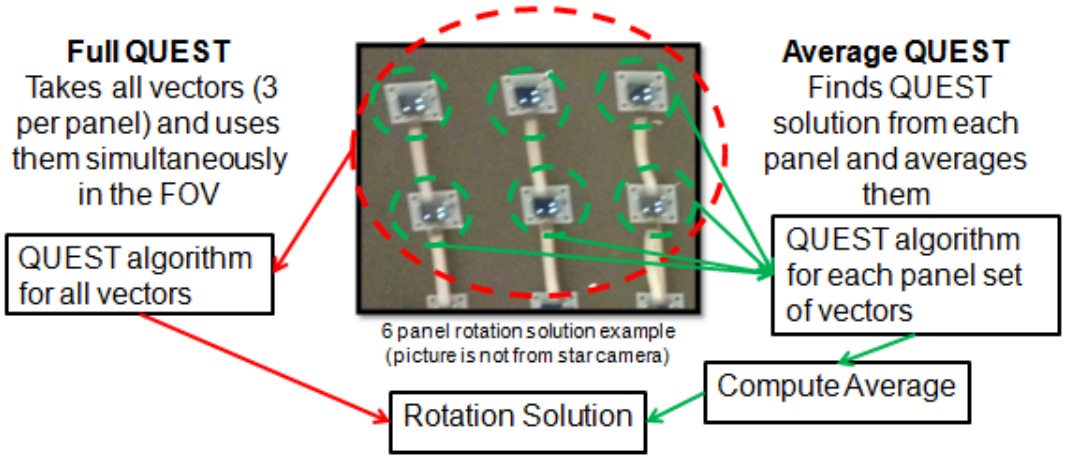

Figure 4.11: Depiction of Full QUEST and Average QUEST Approaches Used Once Errors were Noticed in Y-Axis Test

Since this issue could not be fully resolved in time to finish this thesis effort, an alternate approach was developed called the "Average QUEST" algorithm. Instead of using all the vectors derived from an image in QUEST at the same time, each panel's set of three vectors was used to find an attitude solution using the QUEST algorithm and then all of those solutions were averaged. The "Full QUEST" algorithm simply refers to the intended instance of the QUEST algorithm which takes all vectors at once and produces a single attitude estimation. The comparison between the two methods is laid out in Figure 4.11.

An example case is presented in table form in Figure 4.12 which highlights the accuracy loss when using the full QUEST algorithm. The Euler Angle Z solution for each panel appears to be centered around zero degrees, so there could be some distortion issues that causes panels in certain parts of the FOV to have increased error depending on where they are in relation to the boresight. However, since we are only using one panel these errors could also be caused by the "cosine effect", especially if the panels are near the boresight itself.

Full QUEST vs. Panel Averaged QUEST Example									
	Panel 1	Panel 2	Panel 3	Panel 4	Panel 5	Panel 6	Truth	Full QUEST Error	Avg QUEST Error
EA X (deg)	0.246	-0.217	0.061	0.147	-0.401	-0.386	-0.140	-0.254	-0.049
EA Y (deg)	10.542	10.695	10.561	10.571	10.689	10.706	10.649	0.017	0.022
EA Z (deg)	0.634	0.363	-0.588	-0.039	-0.381	-0.675	-0.155	-1.318	-0.041

Figure 4.12: Table with Highlighted Accuracy Differences Between Full QUEST and Average QUEST Methods

The increased error values were of similar magnitude across the entire Y-axis range of motion on the support cage, as shown in Figure 4.13. The worse case mean absolute error about the full range of motion for the average QUEST method was 0.0891 degree, while the worse case mean absolute error for the full QUEST method was 0.8195 degree, which is almost an order of magnitude increase.

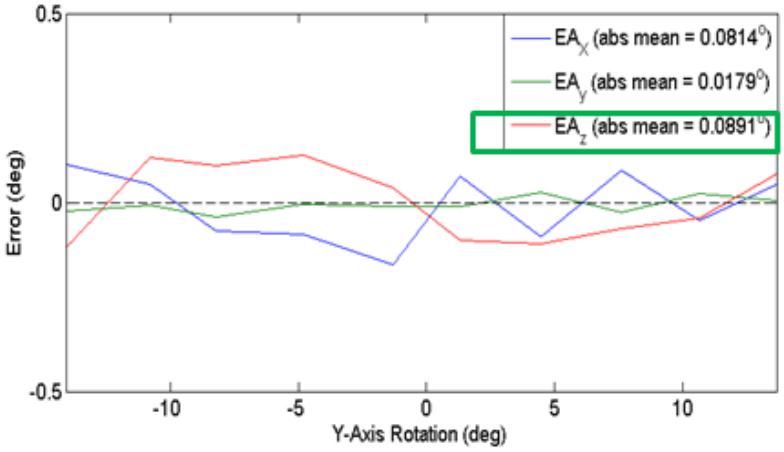

(a) Y-Axis Rotation Solution Error Using Average QUEST

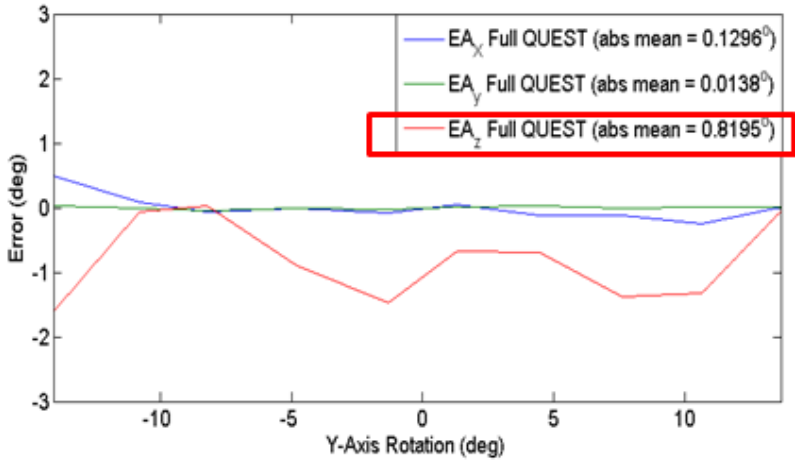

(b) Y-Axis Rotation Solution Error Using Full QUEST

Figure 4.13: QUEST Method Comparison for Y-axis

The test was repeated about the X-axis for the average QUEST case to ensure that similiar accuracy levels could be achieved and these results were not dependent on axis, which could be possible since the dome is ellipsoidal and not perfectly spherical. The results of this test were similar with a worse case mean absolute error of 0.0841 degree using the average QUEST algorithm, as shown in Figure 4.14.

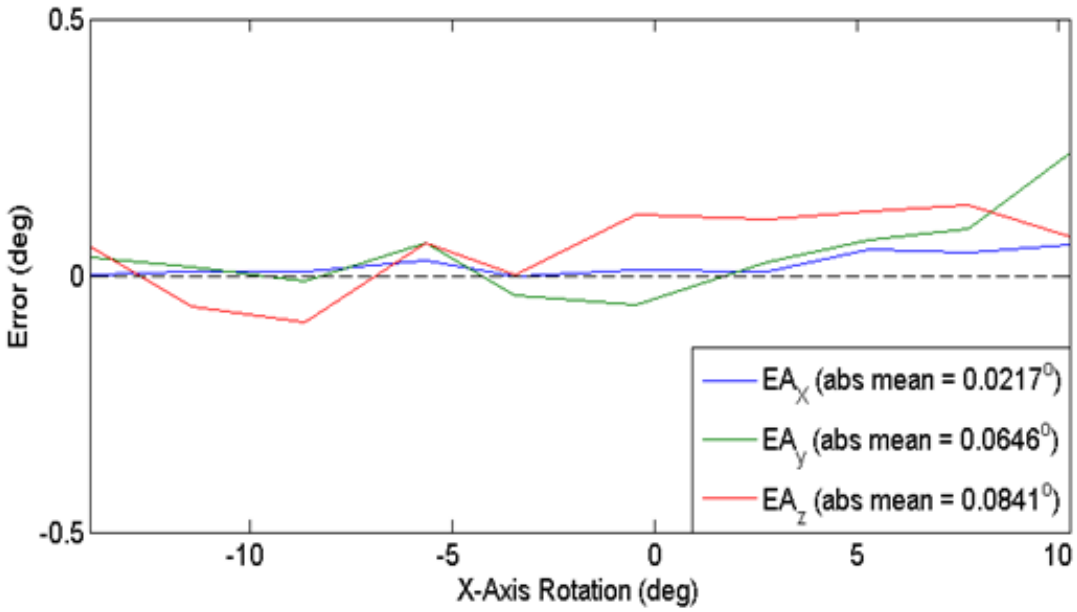

Figure 4.14: X-Axis Rotation Solution Error Using Average QUEST

Initially this discrepancy was thought to be caused by the camera catalog itself, arising from the inconsistency between catalog points as discussed in Section 4.1.3. Testing this theory required using the FaroArm catalog approach in some capacity. Since the FaroArm catalog still had relative position of each star correct, the step between two tested rotation locations could be calculated by subtracting one test point from another. For example, the Y-axis test was conducted by starting at -15 degrees and rotating SimSat by about +3 degrees about the Y axis until SimSat reached the end of the range of motion on the

other side of the support cage, near +15 degrees about Y. Taking the step between two points, which is around 3 degrees, calculating from the FaroArm catalog solution and comparing it to the truth solution can tell us a general idea of the FaroArm catalog's validity. These results are presented in Section 4.2.2.2 and since the FaroArm catalog does seem to be viable, the step error between from the camera catalog and FaroArm catalog can be compared for the full QUEST and average QUEST approaches, as shown in Figure 4.15.

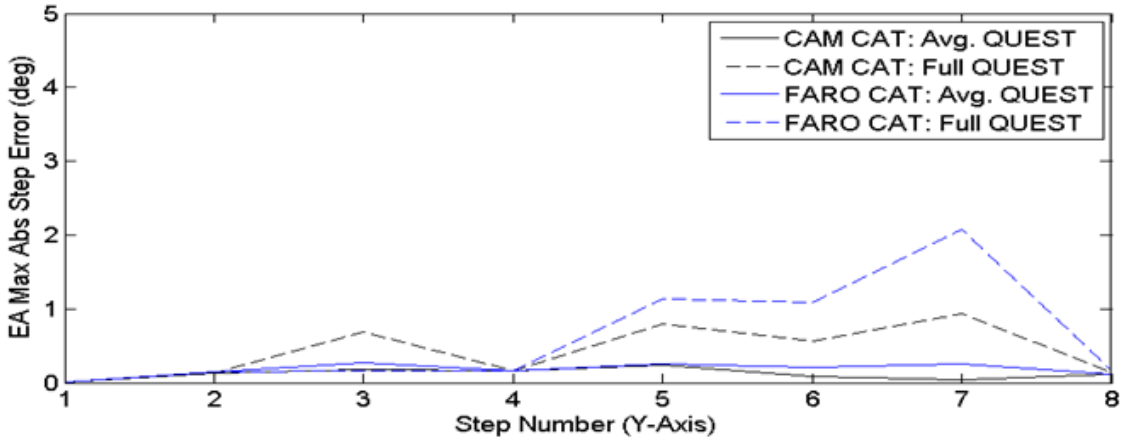

Figure 4.15: FaroArm Catalog and Camera Catalog both Show Larger Max Error Using Full QUEST

Figure 4.15 shows that the full QUEST error is likely from a combination of factors and not just from the camera catalog. The dotted lines utilize the full QUEST approach and have higher step error than the average QUEST method in almost every step point. In order to further characterize the catalog differences when using the different algorithms, the FaroArm catalog needs to be rebuilt with the axes correctly fixed so rotation solutions can be directly compared instead of step solutions.

The accuracy loss with the full QUEST algorithm was a surprise; however, the average QUEST algorithm shows that the system can still reach improved accuracy levels and that there is still enough information in each image to calculate a valid rotation solution.

4.2.2.2 Verifying Feasibility of FaroArm Based Catalog.

As discussed in the previous section, the FaroArm catalog was investigated briefly in this research by comparing the step between two rotation test points. This was done first for the Y-axis, shown in Figure 4.16, yielding a worst case mean absolute step error of 0.1407 degree. The X-axis test was also used to calculate step error, depicted in Figure 4.17, which resulted in a worst case mean absolute step error of 0.1354 degree.

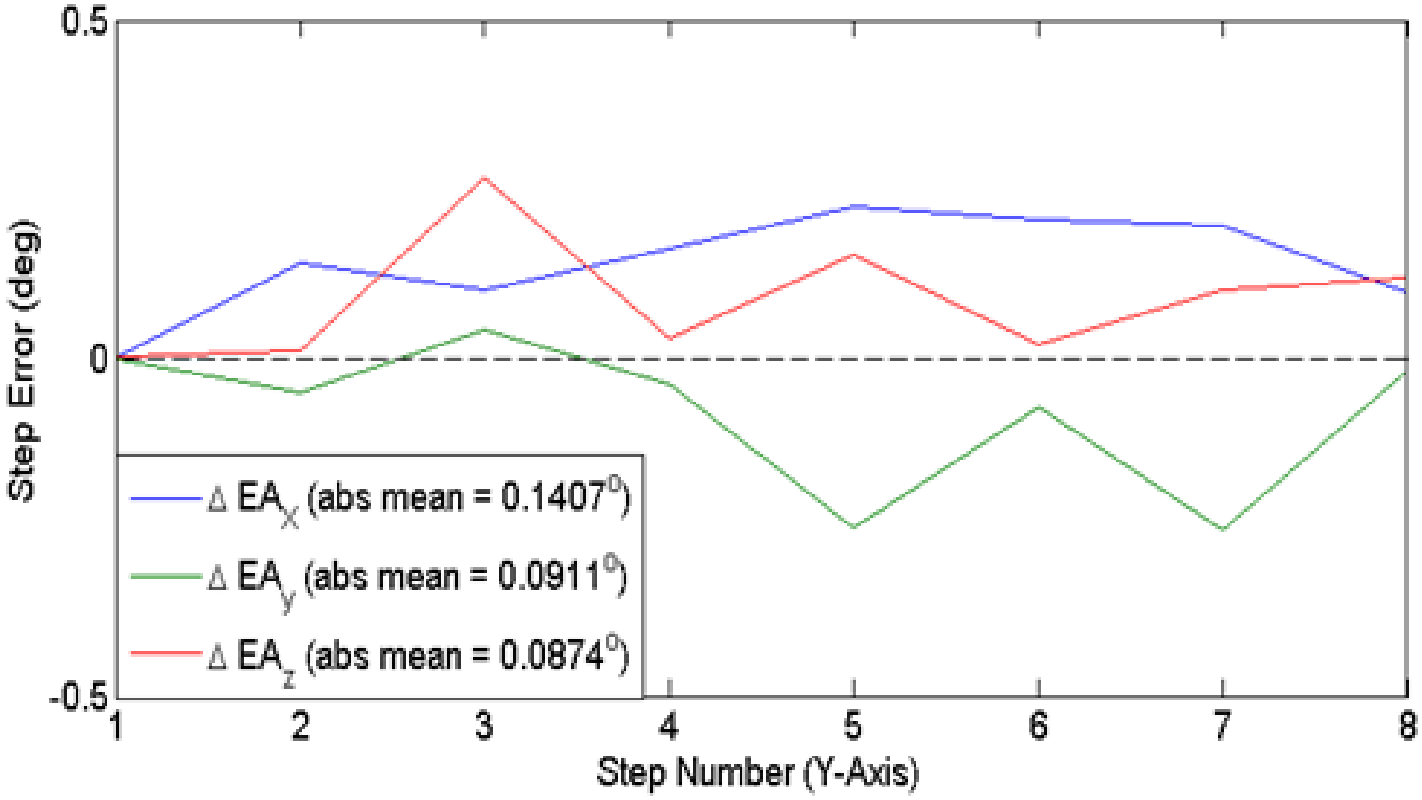

Figure 4.16: Y-Axis Step Error Using FaroArm Catalog

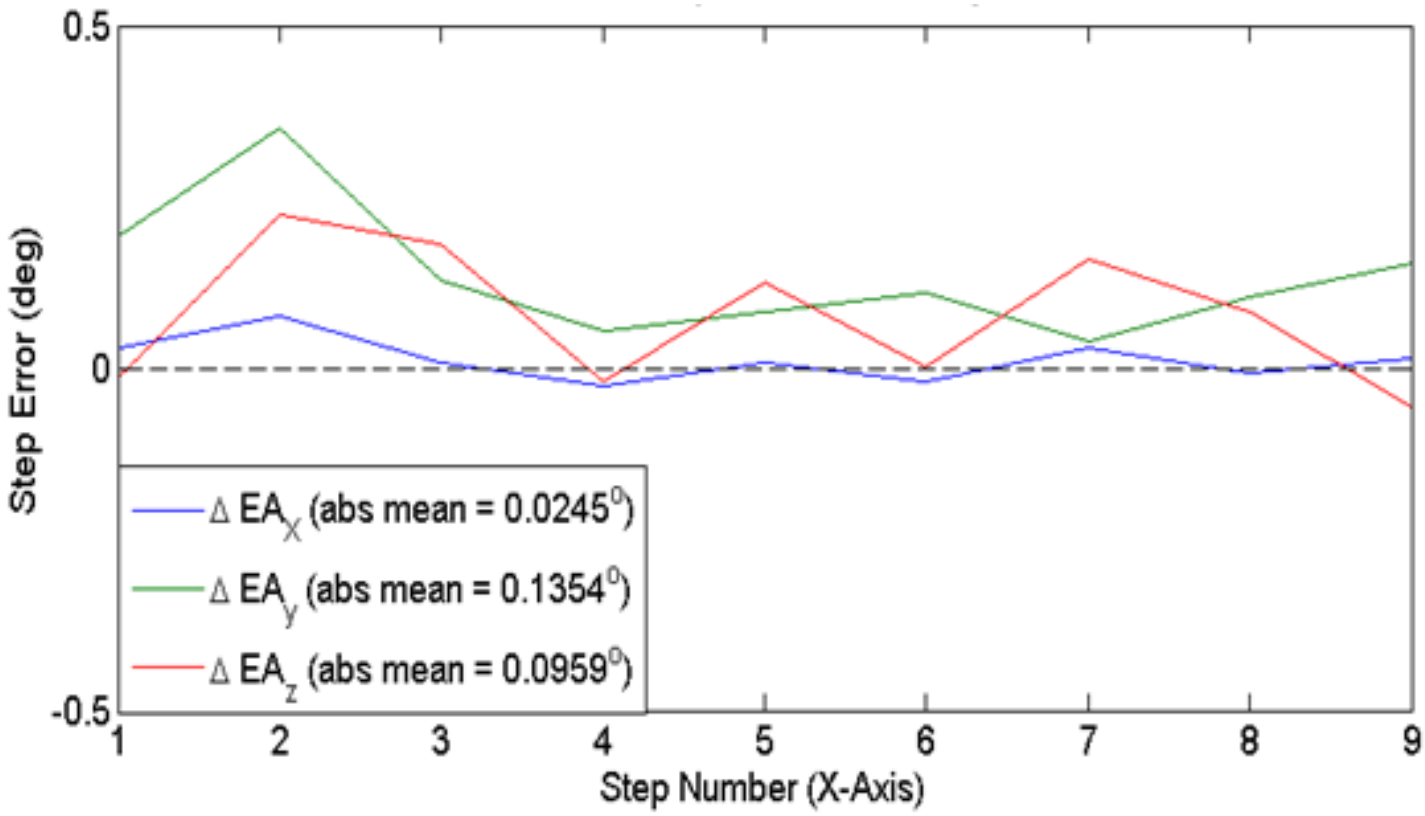

Figure 4.17: X-Axis Step Error Using FaroArm Catalog

These step error values are not truly indicative of rotation accuracies since errors could overlap between two rotations and produce a higher or lower value at a particular step. However, these tests show the FaroArm catalog is definitely feasible and worth the time to recreate the FaroArm catalog after the SimSat dome has been more securely attached to the walls for increased lateral stiffness. Once this catalog is recreated then investigation into the cause of the QUEST algorithm solution errors can be investigated by comparing the catalogs directly instead of through a step error.

V. Conclusions and Recommendations

5.1 Conclusion

The goal of this thesis effort was to create an star field that allowed SimSat to determine its attitude through its star camera system over the full range of motion. While that goal has not yet been obtained, the results from this thesis have brought SimSat closer to having a fully functional external reference system. There are still several integration challenges ahead, but a fully populated star field with robust star patterns is available.

The methodology used in this research started off with creating a test bed that would allow easier progress on full dome population. This test bed was built on an optics bench that also facilitated rotation stages to be fixed relative to the dome that increased testing capabilities. Setting up the optics bench allowed ambient light to be controlled and analyzed. The initial optics bench set up revealed stiffness issues, which would come back when the dome was moved back to above SimSat.

The improvement of the light sources used to populate the dome was another aspect of this research. 0.96 inch OLED panels were ultimately chosen since they do not require a back light which could give false star readings, have a large viewing angle, have many color and brightness options, and are straightforward to program. With these OLED panels, initial investigations into which parameters affect accuracy was performed.

The largest effect on accuracy was shown to be the spread of stars in an image. This effect might only occur in certain cases where the panel is near the boresight, but for small angles the system has difficulty distinguishing between rotations about two different axes if only one closely packed set of vectors is provided. Another large effect was shown to be color interpolation factor of a color camera. Since not every pixel is being fully utilized for centroid information because of interpolation with neighboring pixels, there is an increase in NEA vs. a monochrome camera that utilizes every pixel for pure intensity reading. Focal

length of the optics was shown to affect both NEA and absolute accuracy since it changes the FOV to include more stars when shorted, but can also cause increased distortion in a varifocal lens like the one selected. Aperture was set near closed to increase depth of field and have consistent focus across the FOV. The other aspects that are from the light source that were discussed in Section 3.2 such as star size, star color, and contrast ratio all relate to star brightness. Star brightness is useful for determining distinct stars, but the affect on accuracy can be controlled through software by changing the algorithm parameters, as shown in Section 3.2.4. Once these preliminary investigations were concluded, the population scheme for the dome was created.

Fully covering the dome in OLED panels was driven by the requirement that at least two panels always be in the FOV. Satisfying this requirement was initially calculated to require 125 panels, all of which would need wiring harnesses to be powered and reprogrammed. The ability to inertially catalog each panel through an external reference was also a desired trait. The problem of fixing the rectangular panels to the spherical dome also was issue. The 3D printed panel mount was designed to solve all of these problems by allowing wires to pass under all panels, permitting easy FaroArm measurement of the panel plane, and providing a spherical backing to mate with the dome. With this mount, the panels could be arranged in a way to minimize the maximum amount of wire that would have to pass under a single panel. With the panels fully covering the dome, the development of a robust catalog was next.

The star catalog leverages the placement sensitivity of the OLED panels to place predictable images on each screen that can be recognized by the camera. A triangle method was developed to add more stars on each panel and add more robustness to the panel identification scheme. This catalog was able to be built with the FaroArm (although it was built incorrectly on SimSat in its current state) or with the camera, as long as the current

position is known from another source. With this star catalog, the final system results could be investigated.

The camera comparison between the monochrome Lw235m and color Lu205c revealed the speed and accuracy advantages of using a black and white camera. Testing NEA with the 25mm lens and three panels in the FOV the Lw235m resulted in a NEA of 3.6 arcseconds, compared to a NEA of 6.84 when using the color camera. Since the black and white camera only has to download one third of the data, the systems update rate can also be sped up by nearly a factor of three since the cataloging approach used is not time consuming (compared to real star trackers). With these results, the monochrome camera was used throughout the rest of the research.

While still on the optics bench, the influence of ambient light was tested. The main conclusions to draw from this test was that ambient light is not a factor that has a strong effect on the system. The centroiding algorithm parameters may have to be adjusted to reject more false stars (especially with directive light on the dome which causes many reflects), but the system is capable of performing under all most light conditions. This means that a background shroud was not needed in the SimSat room, but the algorithm would have to be readjusted once the dome was set up above SimSat. But before the dome was moved, cataloging across the center swath of the dome was tested to ensure it could perform over a wide area.

Sweeping across the dome in 2 degree increments after cataloging every 18 degrees revealing an interesting trend. The error was low when the FOV included only stars that were part of the same catalog "group" (meaning they were cataloged at the same time). When stars from two different catalog groups, the errors grew in a predictable fashion. This could point to the center of rotation not being properly aligned or a mistake in calculating the inertial vectors from the cataloged position. Further investigation on the optics bench also revealed that the rotation stages utilized may not be properly calibrated

since they had greater than reported minimum bidirectional repeatability and suffered from gear lash, see Figure 4.6 and Figure 4.7. While the lack of confidence in the rotation stages was troublesome, the concepts proved effective so the dome was moved back to overhead SimSat.

Initial results back on SimSat were promising, but there are still challenges ahead. The camera based catalog approach performed well with the focal length of 20 mm when cataloging the center three panels. RMS error of the Euler Angles over three positions was 0.0243 degrees, which shows what the system is can be capable of accomplishing. More tests over the available range of motion with the SimSat support cage rotating about the X and Y axes revealed a worst case error of about 0.09 degree using the average QUEST algorithm. Fixing the error with the full QUEST algorithm will probably take several more steps, including lens distortion mapping, dome distortion characterization, and FaroArm catalog reconstruction, which are all described in Section 5.2.

The center of rotation and Z-axis was cataloged with the FaroArm, but the X and Y-axis were correctly aligned with an external reference, so their exact direction is unknown (we just know that they lie in the same plane as the real X and Y axis used for SimSat). The dome was also not stiff enough to have a reliable position to inertially catalog and assume the star positions fixed over time. Although testing thus far has shown the FaroArm catalog to be a reliable method by utilizing the step error calculations, stiffening the dome frame above SimSat will be one of the more immediate steps in future work and then the panels can be re-cataloged so the FaroArm catalog method can be investigated further(which would negate camera catalog issues).

In conclusion, the process of building a reliable star tracker based external reference system has been studied and has shown promise to achieve high accuracy. Future work must be done to increase the integration and robustness of the software along with securing

the positional integrity of the system. With these improvements, the star dome system will allow AFIT to explore more advanced areas of spacecraft attitude determination.

5.2 Research Future Work

In order to fully realize the potential of the system, the following focus areas are suggested.

5.2.1 Dome Structural Reinforcement.

Before attempting further cataloging endeavors, the dome structure should be stiffened as much as possible to prevent any lateral movement. Triangular braces could be added to the dome's hanging supports to make the system more rigid and prevent transient movement along with reducing long term creep effects. This would ensure the system would be robust for future endeavors and allow comparison of the FaroArm catalog method with the camera approach to see if they can be melded together.

5.2.2 Software Robustness.

This aspect covers some of the aspects that really hampered the last phase of this research. The issues with SimSat compatibility with certain MATLAB routines (randomly sending an error report and freezing) and the camera video feed software prevented camera cataloging to be completely quickly over the width of the dome. These issues may be caused by using an older version of MATLAB since the functions were programmed in more recent versions or cross referencing of the same functions.

Another aspect of error checking that should be addressed is the rejection of partial stars right on the edge of the FOV. This can lead to incorrect panel recognition in a small percentage of cases. A simple fix would be to not attempt to solve for star centroids that are near the edge of the FOV. This would prevent both incorrect panel matches and bad centroid placement, but correct panel recognition, which would lead to somewhat inaccurate vector creation.

One more aspect of this is the ability to track stars while slewing. Either a maximum slew rate needs be to established so that the star tracker will not attempt to take measurements when slewing to prevent motion blur, or the slew information can be extracted from the amount of blur in the image.

As mentioned in Section 4.2.2.1, resolving the high error when using the full QUEST algorithm should be a priority. The system has error levels near 0.08 degree using the average QUEST, but is capable of 0.02 degree error (as demonstrated by first Z-axis test on SimSat) using the full QUEST. However, the full QUEST algorithm has issues when being utilized over different sections of the dome. Resolving this issue involves first confirming the catalog differences by rebuilding the FaroArm catalog, then investigating distortion of the lens and of the dome itself, as described in the next section.

5.2.3 Lens and Dome Distortion Mapping.

Creating a distortion map of the lens at a given focal length will improve overall accuracy and may significantly reduce the error of using the full QUEST algorithm. This can be done by taking a checkerboard pattern grid and imaging it with the camera. By finding how much the known straight lines are bending, the distortion of the lens can be mapped. This map can then be inverted in every image to create a non-distorted image. Initial investigations using the 25 mm lens showed that this was not expected to be a large problem, but this factor was not fully investigated with the new 12-36 mm zoom lens.

Another possible error source could be the distortion of the dome itself. Although the distance to each panel is known by utilizing the FaroArm, the assumption that each panel is facing directly at the center of rotation may be incorrect. This could be tested on the dome in several different ways. One possible ways would be to set up a set of laser points around the camera lens to project a known shape, such as a square, onto the dome. This square could be imaged at different points on the dome's surface and the amount of variance in the shape across different sections of the dome would reveal how good the assumption is that

each point of the dome can be approximated as a plane normal to the camera lens directly near the boresight.

5.2.4 Motion Capture Technology Cataloging.

Another way to catalog the stars would be to use a motion capture machine to briefly catalog all of the stars. SimSat could be outfitted to record its position and then moved around the FOV. This is just one possibility if the FaroArm catalog does not work well. However, this idea still requires SimSat to remain still when taking pictures at a given attitude. This would require a better support system for any position, such as an adjustable stand where every land can be adjusted to a separate height. If that was procured then the FaroArm vector rotation method could be used to catalog the dome with the camera, but it would take much longer.

5.2.5 Integrated Panel Programming.

The ultimate goal is to allow reprogramming of each panel. Initially, the plan was to use an I2C bus to switch each panel on/off and program them one at a time with a PC fixed above SimSat, as shown in Figure 5.1. The reprogramming of all panels would facilitate more advanced star pattern recognition algorithms, but might not improve the overall accuracy much.

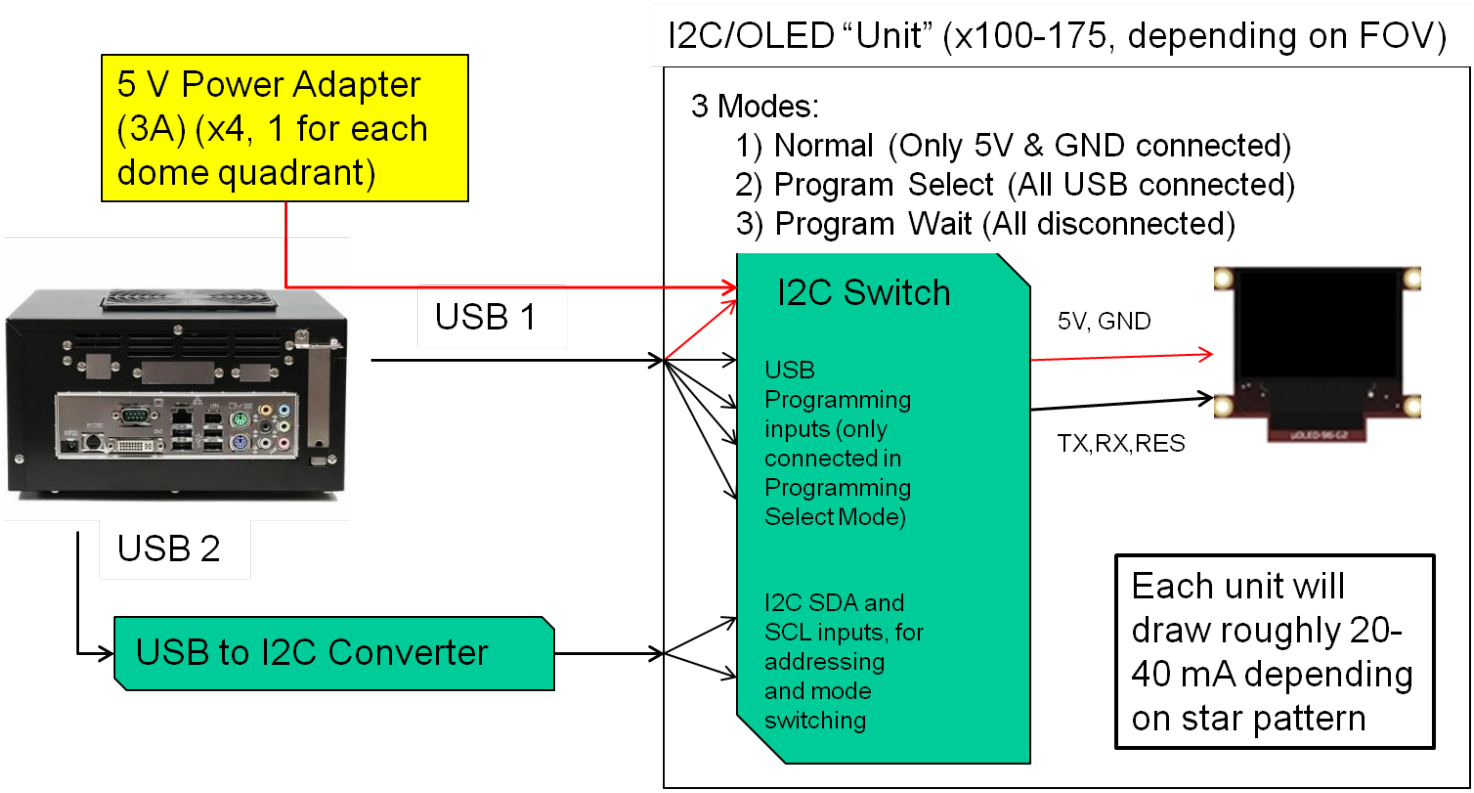

Figure 5.1: OLED Panel Network Plans

Bibliography

[1] "HIPPARCOS - Hipparcos Main Catalog", Aug 2012. URL http://heasarc.gsfc.nasa.gov/W3Browse/all/hipparcos.html.

[2] Berry, Richard and James Burnell. *The Handbook of Astonautical Image Processing*. Willmann-Bell, second edition, 2011.

[3] Boone, B.G., J.R. Bruzzi, W.F. Dellinger, B.E. Kluga, and K.M. Strohbehn. "Optical Simulator and Testbed for Spacecraft Star Tracker Development". *Optical Modeling and Performance Predictions II*, volume 5867. Proc. of SPIE, 2005.

[4] Diaz, Kenneth D. *Performance Analysis of a Fixed Point Star Tracker Algorithm for use Onboard a Picosatellite*. Master's thesis, California Polytechnic State University at San Luis Obispol, 2006.

[5] Eisenman, Allan R., Carl C. Liebe, and John L. Joergensen. "New Generation of Autonomous Star Trackers". *SPIE*, volume 3221, 524–535. 1997.

[6] Eisenman, Allan R. and C.C. Liebe. "The Advancing State-of-the-Art in Second Generation Star Trackers". *Aerospace Conference, 1998 IEEE*, volume 1, 111–118 vol.1. 1998.

[7] Geffroy, Bernard, Phillippe le Roy, and Christophe Prat. "Review Organic Light-Emitting Diode (OLED) Technology: Materials, Devices, and Display Technologies". *Polymer International*, 55:572–582, 2006.

[8] Hall, Chris. "Spacecraft Attitude Dynamics and Control", 2003. Virginia Tech Course Notes.

[9] Hechtl, Eugene. *Optics*. Addison Wesley, fourth edition, 2002.

[10] Inc., FARO Technologies. *FARO Edge Features, Benefits, and Technical Specifications*, September 2013.

[11] Liebe, C.C. "Star Trackers for Attitude Determination". *Aerospace and Electronic Systems Magazine, IEEE*, 10(6):10–16, 1995.

[12] Liebe, C.C. "Accuracy Performance of Star Trackers - A Tutorial". *Aerospace and Electronic Systems, IEEE Transactions on*, 38(2):587–599, 2002.

[13] Liebe, C.C., E.W. Dennison, B. Hancock, R.C. Stirbl, and B. Pain. "Active Pixel Sensor (APS) Based Star Tracker". *Aerospace Conference, 1998 IEEE*, volume 1, 119–127 vol.1. 1998.

[14] Liu, Hai-bo, Yi-zhou Tan, Ding-yi Sheng, Jian-kun Yang, Ji-chun Tan, Weng-liang Wang, and De-zhi Su. "Distortion Model for Star Tracker". *Proc. SPIE*, volume 7544, 75445T–75445T–6. 2010.

[15] Markley, F. Landis. "Attitude Determination Using Two Vector Measurements". *NASA Technical Report*, 1998.

[16] McChesney, Christopher G. *Design of Attitude Control Actuators for a Simulated Spacecraft*. Master's thesis, Air Force Institute of Technology, 2011.

[17] McFarland, C. Dougas. *Near Real-Time Closed-Loop Optimal Control Feedback for Spacecraft Attitude Maneuvers*. Master's thesis, Air Force Institute of Technology, 2009.

[18] Michaels, D. "Ball Aerospace Star Tracker Achieves High Tracking Accuracy for a Moving Star Field". *Aerospace Conference, 2005 IEEE*, 1–7. 2005.

[19] Needelman, David, Rongsheng Li, and Yeong-Wei Andy Wu. "Recent Advances in Stellar Attitude Acquisition (SAA) Algorithms and Procedures". *AIAA Guidance, Navigation, and Control Conference and Exhibit, 2005 AIAA*, 1–17. 2005.

[20] Padro, Jorge. *Development of a Star Tracker-Based Reference System for Accurate Attitude Determination of a Simulated Spacecraft*. Master's thesis, Air Force Institute of Technology, 2012.

[21] Potter, J.E. and W.E. Vander Velde. "Optimum Mixing and Gyroscope and Star Tracker Data". *J. Spacecraft*, 5(5), 1967.

[22] Roach, Neal, Wayne Rohe, and Nathan Welty. *A Systems Engineering Approach to the Design of a Spacecraft Dynamics and Control Testbed*. Master's thesis, Air Force Institute of Technology, 2008.

[23] Shuster, Malcom D. "Focal-Plane Representation of Rotations". *The Journal of Astronautical Sciences*, 48(2):381–390, 2000.

[24] Shuster, M.D. and S.D. Oh. "Three-Axis Attitude Determination from Vector Observations". *Journal of Guidance and Control*, 4(1), 1981.

[25] Snider, Ryan E. *Attitude Control of a Sattelite Simulator Using Reaction Wheels and a PID Controller*. Master's thesis, Air Force Institute of Technology, 2010.

[26] Swenson, Eric. "MECH 632: Intermediate Spacecraft Dynamics", 2013. Air Force Institute of Technology Course Notes.

[27] Tappe, Jack, J.J. Kim, Albert Jordan, and Brij Agrawal. "Star Tracker Attitude Estimation for an Indoor Ground-Based Spacecraft Simulator". *AIAA Modeling and Simulation Technologies Conference 8-11 August*. 2011.

[28] Tappe, Jack A. *Development of Star Tracker System for Accurate Estimation of Spacecraft Attitude*. Master's thesis, Naval Postgraduate School, 2009.

[29] Thorlabs. *CR1-Z7 Motorized Rotation Stage Operating Manual*, August 2012. Rev D.

[30] Thorlabs. *PRM1Z8 Motorized Rotation Stage User Guide*, Nov 2013. Rev E.

[31] Wessling, Francis and Mark Vander Does. "The Star Field Simulator for the Spacelab Instrument Pointing System Fixed Head Star Trackers". *SPIE*, 2221:116–127, 1994.

[32] Wiesel, Willam. *Spaceflight Dynamics*. Aphelion Press, third edition, 2010.

REPORT DOCUMENTATION PAGE

Form Approved
OMB No. 0704–0188

1. REPORT DATE *(DD–MM–YYYY)*	2. REPORT TYPE	3. DATES COVERED *(From — To)*
27–03–2014	Master's Thesis	Oct 2012–Mar 2014

4. TITLE AND SUBTITLE

Design of a Programmable Star Tracker-Based Reference System For a Simulated Spacecraft

5a. CONTRACT NUMBER

5b. GRANT NUMBER

5c. PROGRAM ELEMENT NUMBER

6. AUTHOR(S)

Grunwald, Warren C., Second Lieutenant, USAF

5d. PROJECT NUMBER

5e. TASK NUMBER

5f. WORK UNIT NUMBER

7. PERFORMING ORGANIZATION NAME(S) AND ADDRESS(ES)

Air Force Institute of Technology
Graduate School of Engineering and Management (AFIT/EN)
2950 Hobson Way
WPAFB, OH 45433-7765

8. PERFORMING ORGANIZATION REPORT NUMBER

AFIT-ENY-14-M-22

9. SPONSORING / MONITORING AGENCY NAME(S) AND ADDRESS(ES)

Capt Jorge Padro, Comm: (505) 853-4749, email: jorge.padro@us.af.mil
Air Force Research Lab, Space Vehicles Directorate (RV)
3550 Aberdeen Ave SE
Bldg 472 Rm 225
Kirtland AFB, NM 87117

10. SPONSOR/MONITOR'S ACRONYM(S)

AFRL/RVSV

11. SPONSOR/MONITOR'S REPORT NUMBER(S)

12. DISTRIBUTION / AVAILABILITY STATEMENT

DISTRIBUTION STATEMENT A:
APPROVED FOR PUBLIC RELEASE; DISTRIBUTION UNLIMITED

13. SUPPLEMENTARY NOTES

14. ABSTRACT

The main objective of this research effort is to achieve an accuracy level for the SimSat star tracker system comparable to what is reported in current literature by various star tracker manufacturers and researchers. Previous work has provided a spherical star dome that needs to be fully populated with light sources. Programmable organic light emitting diode (OLED) panels were chosen to populate the dome to allow high contrast ratios without backlighting and increase the number of star combinations able to be represented. Noise equivalent angles less than five arcseconds (1σ) are achieved about the boresight axis and less than half an arcsecond around the other axes. Absolute accuracy near the center of the star dome is tested to be less than 0.04 degree about each axis. Two different approaches to inertially cataloging the starfield are also investigated, externally referencing each panels coordinates using a coordinate measurement arm and utilizing the camera's known position to catalog the panel's location. The full population of the SimSat star dome and reprogrammable capability of the panels allows many future research endeavors related to star pattern recognition and attitude determination to be undertaken.

15. SUBJECT TERMS

SimSat, star tracker, attitude determination, satellite simulator

16. SECURITY CLASSIFICATION OF:			17. LIMITATION OF ABSTRACT	18. NUMBER OF PAGES	19a. NAME OF RESPONSIBLE PERSON
a. REPORT	b. ABSTRACT	c. THIS PAGE			Eric D. Swenson (ENY)
U	U	U	UU	152	19b. TELEPHONE NUMBER *(include area code)* (937) 255-3636 x7479 eric.swenson@afit.edu